The Thesis Committee for Ziye Liu
Certifies that this is the approved version of the following thesis:

An Analytical Model for Quantification of Geosynthetic Benefits in Roadway Base Stabilization

APPROVED BY
SUPERVISING COMMITTEE:

Jorge G. Zornberg, Supervisor

Gholam Hossein Roodi

An Analytical Model for Quantification of Geosynthetic Benefits in Roadway Base Stabilization

by

Ziye Liu

Thesis

Presented to the Faculty of the Graduate School of

The University of Texas at Austin

in Partial Fulfillment

of the Requirements

for the Degree of

Master of Science in Engineering

The University of Texas at Austin

August 2018

Dedication

To my grandmother

To my parents

Acknowledgements

This research was carried out under the inspiration and support of several individuals to whom I would like to express my sincere gratitude.

I am deeply grateful to my supervisor, Dr. Jorge G. Zornberg, for his guidance and support throughout my time as his student. He showed respect for my research interest and introduced me to a challenging and enjoyable research topic. I benefited a lot from his valuable suggestions and continuous encouragement all along my research.

I would also like to thank Dr. Gholam Hossein Roodi for helping me grow as a better researcher under his patient guidance. By working closely with him during the entire process of model development, I was able to overcome the difficulties and frustrations with his valuable inputs as an experienced colleague and kindest support as a friend. I was very fortunate to work with such a great man.

I am also grateful that I have those nice and talented classmates: Chris Nelsen, Jonas Bauer, James Munson, Lucas Melo, Ashim Gajurel, Shivangi Jain, Luming Yang, Liming Zheng. They helped and encouraged me during my studies at the University of Texas at Austin. It was so good to share our memory as graduate students in our Geotechnical Engineering Program. I learnt a lot from them, and I wish them the best in their bright future.

I also wish to thank Dr. Xin Peng for his help when I first joined the research group of Dr. Zornberg. Xin taught me how to conduct small pullout tests using transparent soil. He was very patient with me. I also appreciated the advice he gave me when I was confused about my research path and future plan. It was really nice experience that I could work with and learn from him.

I would also like to convey my special thanks to my friends: Kai Feng, Kenny Cheang and Zhoufeng Ying. I will never forget your support and encouragement during these two years of my life. Maybe the luckiest thing that happened to me in this city was to have you as my close friends.

Lastly, I want to express my deepest gratitude to my parents and all my family. My mother was always listening to me and encouraging me when I felt frustrated. My grandmother loves me unconditionally, and she does not need me to be successful but happy and healthy. I always feel supported by my lovely family. They mean a lot to me wherever I am.

Abstract

An Analytical Model for Quantification of Geosynthetic Benefits in Roadway Base Stabilization

Ziye Liu, M.S.E.

The University of Texas at Austin, 2018

Supervisor: Jorge G. Zornberg

Stabilization of base aggregate using geosynthetics may provide improved performance in flexible pavements. Through the aggregate-geosynthetic interaction, the induced shear stress in the base aggregates is transferred to the geosynthetic resulting in the development of tensile stresses. The tensioned geosynthetic applies in turn additional lateral confinement to the aggregates to restrain their movement under repeated traffic loading. The use of geosynthetics in base stabilization has been reported to result in reduced rutting depths in roadways. Design guidelines, either empirical or mechanistic-empirical, have been established for the design of non-stabilized roadways. These guidelines, however, do not take the geosynthetic effect into account. Accordingly, the geosynthetic benefits in base stabilization need to be quantified in a way that can easily be incorporated into the existing design procedures. This study proposed an analytical model to achieve this goal.

In this study, the additional lateral confinement provided by the geosynthetic was modeled as a uniform additional confining stress within the geosynthetic influence zone.

The pavement section was considered as an infinitely long elastic solid under plane strain conditions, which allowed the model framework to be established using the theory of elasticity. The aggregate-geosynthetic interaction, on the other hand, was modeled using the soil-geosynthetic composite (SGC) model. As a result, an additional confining stress could be defined from the stress-displacement relationships in the elastic model framework. An increased elastic modulus could then be predicted from the additional confining stress with a specific criterion for equivalency of the original base course with additional confinement and an alternative base course with enhanced elastic modulus but without additional confinement. The increased modulus can be used as an updated property for the geosynthetic-stabilized base aggregate in mechanistic-empirical pavement design procedures.

The predicted equivalent increased moduli were validated using the results from repeated loading triaxial tests of two published studies. Overall, reasonably good agreement was found between model predictions and the test results. Predictions from this model were also compared against those of another analytical model, and close results were observed. A sensitivity analysis conducted using the proposed model indicated that model predictions are particularly sensitive to the original base modulus, geosynthetic properties (including confined geosynthetic stiffness and the stiffness of the soil-geosynthetic composite) and the thickness of the geosynthetic influence zone.

Table of Contents

List of Tables xiii

List of Figures xiv

Chapter 1: Introduction 1

1.1 Motivation 1

1.2 Research Objectives 3

1.3 Thesis Structure 4

Chapter 2: Literature Review 5

2.1 Overview of Geosynthetic Base Stabilization 5

2.1.1 Base Course in Pavements 5

2.1.2 Geosynthetics in Roadway Systems 6

2.1.3 Test Methods for the Quantification of Soil-Geosynthetic Interaction 8

2.1.4 Mechanisms involved in Geosynthetic Stabilization 13

2.2 Design of Geosynthetic Stabilized Bases 16

2.2.1 Existing Design Methods for Flexible Pavements 16

2.2.2 Approaches to Incorporating the Geosynthetic Influence into Pavement Design 19

2.2.2.1 Improvement Ratio Approaches 19

2.2.2.2 Equivalent Property Approaches 22

2.2.2.3 Development of New Design Procedures 25

Chapter 3: Analytical Model for Geosynthetic Stabilized Bases 28

3.1 Introduction 28

3.2 Modeling Philosophy 29

3.2.1 Assumptions from the Theory of Elasticity 29
3.2.2 Plane Strain Condition 31
3.2.3 Governing Equations 32
3.2.4 Three Pavement Cases 35
3.3 DEVELOPMENT OF THE ANALYTICAL MODEL 38
3.3.1 Assumed Stress Conditions 38
3.3.2 Derivation of Strain and Displacement Expressions 40
3.3.3 Quantification of the Geosynthetic Influence 42
3.3.3.1 Formulation of the SGC Model 42
3.3.3.2 Adaptation of the SGC Model to the Traffic Loading Condition 49
3.3.3.3 Determination of the Additional Confining Stress 50
3.3.3.4 Determination of the Increased Elastic Modulus 53
3.3.4 Model Results 56
Chapter 4: Validation of the Analytical Model 61
4.1 OVERVIEW 61
4.2 VALIDATION USING NAZZAL'S (2007) STUDY 62
4.2.1 Overview of Resilient Modulus Tests by Nazzal (2007) 62
4.2.2 Considerations in the Analytical Model for Comparison with Nazzal's Study 64
4.2.2.1 Model Inputs Regarding Pavement Geometry 65
4.2.2.2 Model Inputs Regarding Geogrid Properties 65
4.2.2.3 Model Inputs Regarding Traffic Loading Conditions 66
4.2.2.4 Assumptions Regarding Soil and Interface Shear Strengths and Soil Elastic Properties 67

4.2.3 Comparison between Model Predictions and Test Results of Nazzal's Study 67

4.3 VALIDATION USING LUO ET AL. (2017) STUDY (NCHRP PROJECT 01-50) 70

4.3.1 Overview of Constitutive Models and Test Plans in Luo et al. (2017) Study....70

4.3.2 Considerations in this Model for Comparison with Luo et al. (2017) Study....73

4.3.2.1 Model Inputs of Pavement Geometry....74

4.3.2.2 Model Inputs of Material Properties 74

4.3.2.3 Model Inputs of Traffic Loading Conditions 76

4.3.3 Comparison between Model Predictions and Test Results of Luo et al. Study 77

4.4 COMPARISON WITH YANG & HAN (2012) MODEL....81

4.4.1 Overview of the Parametric Analysis Conducted by Yang and Han (2012) 82

4.4.2 Input Parameters Specified in the Analytical Model....84

4.4.3 Comparison of Predictions from Two Models 85

Chapter 5: Sensitivity Analysis....88

5.1 OVERVIEW....88

5.2 EFFECT OF MATERIAL PROPERTIES 89

5.2.1 Original Elastic Modulus 89

5.2.2 Confined Geosynthetic Tensile Stiffness....90

5.2.3 Stiffness of the Soil-Geosynthetic Composite K_{SGC} 92

5.2.4 Aggregate-Geosynthetic Interface Friction Angle....94

5.2.5 Poisson's Ratio of the Base Aggregate....95

5.3 EFFECT OF GEOMETRIC CHARACTERISTICS 96

5.3.1 Pavement Layer Thicknesses (h_1 and h_2) 96
5.3.2 Thickness of the Geosynthetic Influence Zone ($2t$) 98
5.3.3 Thickness of the Geosynthetic ($2t_{gs}$) 99
5.4 EFFECT OF TRAFFIC LOADING CONDITIONS 100
5.4.1 Tire Pressure (p) 100
5.4.2 Wheel Width (Ww) 101
5.5 SUMMARY 102
Chapter 6: Summary and Conclusions 103
6.1 Summary 103
6.2 Conclusions 105
6.3 Suggestions for Future Work 107
Appendix A: Determination of Constants b and d 109
Appendix B: Determination of Constant c 112
Appendix C: Correction Factor α 114
References 123
Vita 127

List of Tables

Table 4.1: Properties of Crushed Limestone I Used in Nazzal's (2007) Study 62

Table 4.2: Properties of Geogrids Used in Nazzal's (2007) Study 63

Table 4.3: Geometric Parameters Assumed in the Analytical Model to Compare with Nazzal's Study 65

Table 4.4: Confined Tensile Stiffness Assumed for Geogrids Used in Nazzal's Study 66

Table 4.5: Properties of Geogrids Used by Luo et al. (2017) 72

Table 4.6: Repeat Loading Triaxial Test Protocol Adopted by Luo et al. (2017) 72

Table 4.7: Geometric Parameters Assumed in the Analytical Model to Compare with Luo et al. Study 74

Table 4.8: Confined Tensile Stiffness Assumed for Geogrids Used in Luo et al. Study 76

Table 4.9: Baseline Input Parameters for the Parametric Analysis (Yang and Han, 2012) 82

Table 5.1: Baseline Input Parameters for Sensitivity Analysis 89

List of Figures

Figure 2.1: Test methods for the characterization of soil-geosynthetic interaction: (a) sketch of interface direct shear test; (b) sketch of pullout test (not to scale) 9

Figure 2.2: Sketches of triaxial compression tests: (a) unreinforced aggregate specimen; (b) geosynthetic-reinforced aggregate specimen 11

Figure 2.3: Typical test setup and layout of sensors in the cyclic plate load testing (Abu-Farsakh and Chen, 2011)....12

Figure 2.4: APT facilities: (a) Linear test track (LINTRACK, Delft, Netherlands); (b) Circular test track (LCPC, France)....13

Figure 2.5: Stabilization mechanisms induced by geosynthetics (Holtz et al., 1998): (a) Lateral restraint; (b) Increased bearing capacity; and (c) Tensioned-membrane support....15

Figure 2.6: Summarized flow chart of Luo et al. (2017) study 26

Figure 3.1: Coordinate system of the roadway section considered in this study....32

Figure 3.2: Stresses in an elastic element 33

Figure 3.3: Diagram of Three Pavement Cases: (a) Case 1; (b) Case 2; (c) Case 3 37

Figure 3.4: Constants *a*, *b*, *c* and *d*, traffic loading condition and layer thicknesses marked in the pavement profile 40

Figure 3.5: Constitutive relationships adopted in the SGC model: (a) geosynthetic unit tension-tensile strain relationship; (b) soil-geosynthetic interface shear 44

Figure 3.6: Force equilibrium in the SGC model (Zornberg et al., 2017)....44

Figure 3.7: Different loading mechanisms and the corresponding geosynthetic deformation modes: (a) under pullout loading; (b) under traffic loading.....46
Figure 3.8: Distribution of the important parameters in the SGC model and the proposed analytical model: (a) geosynthetic unit tension; (b) geosynthetic tensile strain; (c) geosynthetic displacement 48
Figure 3.9: Details of the pavement section in Case 2: (a) pavement geometry, traffic loading condition and stress distribution; (b) object of interest in the proposed model: geosynthetic influence zone 57
Figure 3.10: Diagrams of the results of the proposed model: (a) object of interest in the proposed model: geosynthetic influence zone; (b) distribution of geosynthetic unit tension; (c) distribution of geosynthetic tensile strain.....58
Figure 3.11: Diagrams of the results of the proposed model: (a) object of interest in the proposed model: geosynthetic influence zone; (b) distribution of horizontal displacements of the aggregate and geosynthetic 59
Figure 3.12: Diagrams of the results of the proposed model: (a) object of interest in the proposed model: geosynthetic influence zone; (b) distribution of aggregate vertical displacements 60
Figure 4.1: Comparison between $RMr - 1 \times 100\%$ at deviatoric stress of 80 kPa in Nazzal's resilient modulus tests and $RE - 1 \times 100\%$ predicted using the analytical model 68
Figure 4.2: Comparison between $RMr - 1 \times 100\%$ at deviatoric stress of 160 kPa in Nazzal's resilient modulus tests and $RE - 1 \times 100\%$ predicted using the analytical model 69

Figure 4.3: Comparison between $RMr - 1 \times 100\%$ at deviatoric stress of 250 kPa in Nazzal's resilient modulus tests and $RE - 1 \times 100\%$ predicted using the analytical model 69
Figure 4.4: Comparison between $RMr, x - 1 \times 100\%$ of the geogrid TX-1 in Luo et al. Study and $RE - 1 \times 100\%$ predicted using the analytical model.....78
Figure 4.5: Comparison between $RMr, x - 1 \times 100\%$ of the geogrid TX-2 in Luo et al. Study and $RE - 1 \times 100\%$ predicted using the analytical model.....78
Figure 4.6: Comparison between $RMr, x - 1 \times 100\%$ of the geogrid BX-3 in Luo et al. Study and $RE - 1 \times 100\%$ predicted using the analytical model.....79
Figure 4.7: Comparison between $RMr, y - 1 \times 100\%$ of the geogrid TX-1 in Luo et al. Study and $RE - 1 \times 100\%$ predicted using the analytical model.....79
Figure 4.8: Comparison between $RMr, y - 1 \times 100\%$ of the geogrid TX-2 in Luo et al. Study and $RE - 1 \times 100\%$ predicted using the analytical model.....80
Figure 4.9: Comparison between $RMr, y - 1 \times 100\%$ of the geogrid BX-3 in Luo et al. Study and $RE - 1 \times 100\%$ predicted using the analytical model.....80
Figure 4.10: Effect of material modulus on the quantified geogrid benefit (adapted from Yang and Han (2012))....83
Figure 4.11: Comparison of the model predictions of $\Delta \mathrm{M}r,\ \%$ for $\mathrm{Mr, unreinf} = 134{,}241\ kPa$....85
Figure 4.12: Comparison of the model predictions of $\Delta \mathrm{M}r,\ \%$ for $\mathrm{Mr, unreinf} = 201{,}361\ kPa$....86
Figure 4.13: Comparison of the model predictions of $\Delta \mathrm{M}r,\ \%$ for $\mathrm{Mr, unreinf} = 268{,}482\ kPa$....86
Figure 4.14: Comparison of the model predictions of $\Delta \mathrm{M}r,\ \%$ for $\mathrm{Mr, unreinf} = 335{,}602\ kPa$....87

Figure 5.1: Effect of the original elastic modulus Eu on the predicted elastic modulus improvement ratio R_E 90
Figure 5.2: Effect of the confined geosynthetic tensile stiffness Jc on the predicted elastic modulus improvement ratio R_E 91
Figure 5.3: Combined effect of the original elastic modulus Eu and the confined geosynthetic stiffness Jc on the predicted elastic modulus improvement ratio R_E 91
Figure 5.4: Effect of K_{SGC} on the correction factor α 92
Figure 5.5: Effect of K_{SGC} on the predicted elastic modulus improvement ratio R_E 93
Figure 5.6: Combined effect of the original elastic modulus Eu and K_{SGC} on the predicted elastic modulus improvement ratio R_E 94
Figure 5.7: Effect of the aggregate-geosynthetic interface friction angle ϕ on the correction factor α 95
Figure 5.8: Effect of the aggregate-geosynthetic interface friction angle ϕ on the predicted elastic modulus improvement ratio R_E 95
Figure 5.9: Effect of the Poisson's ratio of the base aggregate μ on the predicted elastic modulus improvement ratio R_E 96
Figure 5.10: Effect of the whole asphalt layer thickness $h1$ on the predicted elastic modulus improvement ratio R_E 97
Figure 5.11: Effect of the half base course thickness $h2$ on the predicted elastic modulus improvement ratio R_E 97
Figure 5.12: Effect of the half thickness of the geosynthetic influence zone *t* on the predicted elastic modulus improvement ratio R_E 99
Figure 5.13: Effect of the half geosynthetic thickness tgs on the correction factor α ..100

Figure 5.14: Effect of the half geosynthetic thickness tgs on the predicted elastic modulus improvement ratio R_E 100
Figure 5.15: Effect of the tire pressure p on the predicted elastic modulus improvement ratio R_E 101
Figure 5.16: Effect of the wheel width Ww on the predicted elastic modulus improvement ratio R_E 102
Figure A.1: Geometry of the problem involving a uniform strip load 110
Figure C.1: Deformation of transverse and longitudinal ribs under traffic loading.....116
Figure C.2: Unreasonable result of aggregate displacement using experimental τy 117

Chapter 1: Introduction

1.1 MOTIVATION

Stabilization of road bases is a major geosynthetic application in roadways, especially in flexible pavements. In a multilayer flexible pavement system, the base course is a layer of aggregate material below the surface asphalt layer and above the subgrade. A subbase course is sometimes constructed between the base course and the subgrade to replace part of the more expensive base aggregate. Although geosynthetics can also be placed within the subbase, only geosynthetic stabilization of the base course is discussed herein. Due to repeated traffic loading, the resilient modulus of base aggregate is progressively degraded because of the lateral displacement of aggregate particles. Lower resilient modulus results in higher contact pressures on top of the subgrade and eventually an increased rutting depth in the roadway structure. Geosynthetics have been used to solve this issue, since lateral restraint can be provided by geosynthetics through their interaction with the surrounding aggregate. The presence of a geosynthetic inclusion results in an extended pavement service life or in a decrease in the required base course thickness.

Empirical or mechanistic-empirical methods have been utilized to design pavements. Currently available guidelines, however, do not include adesign procedure for pavements with the geosynthetic-stabilized base course. Research efforts to incorporate the geosynthetic effect into the mechanistic-empirical design have been focusing on identifying a desirable equivalent property for the soil-geosynthetic composite. Among the possible alternatives, probably the most practical one involves using an equivalent increased resilient modulus, since it can conveniently serve as the surrogate property input for the base material within the geosynthetic influence zone. However, due to the

complexity of soil-geosynthetic interaction, the relationship between the increased resilient modulus and the geosynthetic characteristics has not been established so far.

The increased resilient modulus of the soil-geosynthetic composite has been evaluated using repeated loading triaxial tests, whose results are analyzed to fit a generalized constitutive model. However, considerable time and effort are required to perform a complete test series, and the test results are only applicable to a specific geosynthetic product and section layout. Consequently, an analytical model could be beneficial to provide an estimate of the resilient modulus of the soil-geosynthetic composite as a function of model inputs for different stress conditions and geosynthetics. This study aims at developing such a model under the framework of the elasticity theory. Specifically, the geosynthetic benefit was first quantified as an additional confining stress, which was then used to predict an increased resilient modulus using equivalency criteria.

Mechanistic-empirical pavement design defines the critical resilient strains using the multi-layered elasticity theory and then predicts the pavement distresses using empirical equations. Computer-aided design tools have been developed to automatically calculate the critical strains based on inputs such as pavement geometry, material properties, and traffic loading conditions. The analytical model proposed in this study can provide the property input of the geosynthetic-stabilized base material for the design software. By incorporating the effect of geosynthetics in this way, the current mechanistic-empirical design procedure can still be used, thereby providing designers with a viable method to evaluate the performance of geosynthetic-stabilized pavements.

1.2 RESEARCH OBJECTIVES

The overall objective of this research is to develop an analytical model to quantify the geosynthetic effect on the stabilization of road bases. Specifically, the proposed model aims at obtaining an equivalent increased resilient modulus of the geosynthetic-stabilized base material. This modulus can serve as the input in the design software to estimate the critical pavement response under traffic loading. This updated input enables designers to apply the currently available mechanistic-empirical design procedure to pavements with the geosynthetic-stabilized base course.

In order to achieve the overall objective, the following specific objectives are pursued in this study:

- Determine the force equilibrium, stress-strain relationship, displacement-strain relationship for the geosynthetic-stabilized base material using the theory of elasticity, to establish the basic framework of the analytical model.
- Express the additional confining stress $\Delta\sigma_3$ provided by the geosynthetic as a function of the geosynthetic tension.
- Obtain a closed-from solution for $\Delta\sigma_3$ based on the relations established in the above framework.
- Define a reasonable criterion to establish the equivalency between the additional confining stress and the increased resilient modulus of the geosynthetic-stabilized base material.
- Estimate the increased resilient modulus using the specified criterion.
- Validate the model results of the increased resilient modulus using the repeated loading triaxial tests results reported in the literature.
- Analyze the sensitivity of the model results to the input parameters.

1.3 THESIS STRUCTURE

This thesis includes six chapters. Chapter 1 introduced the motivation and objectives for this research. Chapter 2 provided the background information on the geosynthetic base stabilization and the related design methods. Research progress in the incorporation of the geosynthetic effect into the established design guidelines was also summarized in Chapter 2. Chapter 3 introduced the modeling philosophy and provided details on the derivation of the analytical model. Quantification of the geosynthetic influence in the form of the additional confining stress or the increased resilient modulus was also discussed in detail in this chapter. Chapter 4 included the model validation conducted by comparing the model predicted increased resilient moduli of the soil-geosynthetic composite with the measured triaxial test results of Nazzal (2007) and Luo et al. (2017). Also included in this chapter was a comparison between the predictions of this model and those of Yang & Han (2012) model. Chapter 5 included a parametric analysis to evaluate the sensitivity of the model predictions to the assigned values of input parameters. Chapter 6 summarized the findings in this research. Some final discussion and conclusion were made based on the obtained results.

Chapter 2: Literature Review

Geosynthetic base stabilization is a roadway application where geosynthetics are used to stiffen the base aggregate material by applying lateral restraint to the aggregate movement under traffic loading. The stiffening provided by geosynthetics can be attributed to the aggregate-geosynthetic interaction. In order to quantify the geosynthetic benefit in base stabilization, the properties of base aggregate, geosynthetics and aggregate-geosynthetic interface should be carefully characterized. In addition, the mechanisms governing the geosynthetic influence on pavement stability need to be clearly identified. According, the evaluation conducted in this chapter discusses characteristics of road bases and geosynthetics, summarizes the test methods used to quantify the soil-geosynthetic interaction, and explains the governing mechanisms involved in geosynthetic stabilization. Furthermore, existing design guidelines for non-stabilized pavements and the emerging methods for incorporating into design the benefits provided by geosynthetics in pavement performance are also discussed. Details can be found in the following sections.

2.1 Overview of Geosynthetic Base Stabilization

2.1.1 Base Course in Pavements

Flexible and rigid pavements are two major types of pavements. As an important component in both types of pavements, the base course is a layer of granular material placed immediately below the surface layer, which is either an asphalt or a concrete layer. The granular material used to construct the base course can be crushed stone, crushed slag, or other untreated or stabilized materials (Huang, 1993).

In flexible pavements, the base course is critical. It provides the required stiffness of the pavement structure, improves the load distribution, and contributes to the subsurface drainage. As a result, it mitigates the development of structural distresses including

cracking and rutting. For reasons of economy, a subbase course composed of locally available, comparatively inexpensive material can be used between the base course and subgrade in flexible pavements. In this way, the thickness of the base course is reduced to reduce costs. In addition, the subbase course with more fines can serve as a filter between the subgrade and the base course, if an open-graded material is used for the base course (Huang, 1993). To improve the pavement performance under both traffic and environmental loads, the unbound granular material in flexible pavements can be stabilized by placing the geosynthetics in the base course, subbase course, or at their interface (e.g., Al-Qadi et al. 2008; Giroud and Han 2004a, b; Roodi and Zornberg 2012; Zornberg et al. 2012).

For rigid pavements, a base course may not be necessary, considering that the critical stress in the concrete can be more economically reduced by slightly increasing the concrete thickness. Nevertheless, the base course has been commonly used in rigid pavements for the control of pumping, frost action, shrinkage and swell, together with the improvement of drainage and the expedition of construction (Huang, 1993). It is not common for the base course to be stabilized in rigid pavements, given that it is mainly used for other purposes other than stiffening of the system.

For the development of an analytical model to quantify the geosynthetic influence, this study focuses on the geosynthetic base stabilization in flexible pavements. Although the model is also applicable to the stabilization of a subbase course, for simplicity only the base course will be discussed herein.

2.1.2 Geosynthetics in Roadway Systems

Geotextiles (woven and nonwoven) and geogrids (biaxial and multiaxial) are the types of geosynthetics most commonly used in roadway systems. Other geosynthetics,

including erosion control products, geocells, geonets (or geocomposite drainage products), and geomembranes have also been utilized in some roadway projects (Zornberg, 2017). These different geosynthetic products can fulfil one or more functions in various roadway applications. For unpaved roads, geosynthetics have been used to improve the load distribution, reinforce the soft subgrade soil and thus prevent the development of shear failure surfaces. For paved roads, however, the use of geosynthetics is usually aimed at minimizing reflective cracking in asphalt overlays as well as at improving the performance of base aggregate layers (Zornberg, 2017).

The typical functions of geosynthetics used in roadway construction include separation, filtration, drainage, sealing, reinforcement and stiffening (Koerner, 2012; Zornberg, 2017). "Reinforcement" should be differentiated from "stiffening" by considering different ranges of deformation and different governing states of the system. Specifically, soil reinforcement refers to the condition where the stability of the soil-geosynthetic composite is maintained or improved by using geosynthetics (e.g., reinforced subgrades in unpaved roads). The governing state of the reinforced soil is the limit state where large deformations develop, which are consistent with global failure. Accordingly, the key geosynthetic property used in soil reinforcement design is its tensile strength. On the other hand, soil stiffening, refers to cases where geosynthetics are utilized to improve the performance of the soil-geosynthetic composite under service loads by controlling the deformation (e.g., stabilization of the base course or asphalt layer in flexible pavements) (Roodi, 2016). The governing state of the stabilized soil is the service state under small deformation, and hence, the relevant design properties are those that quantify the increased stiffness of the soil-geosynthetic composite. When placed in the base course of pavements, the geosynthetic fulfils the function of soil stiffening or stabilization. Accordingly, small

displacement is considered, and thus the theory of elasticity can be adopted to model the pavement response.

The stiffening function can be fulfilled by either geogrids or geotextiles, but geogrids have been more common. Hence, more information on geogrids is provided as follows.

Geogrids are plastics formed into a very open grid-like configuration, with large apertures existing between individual ribs in the machine and cross machine directions (Koerner, 2012). According to the methods of manufacture, geogrids can be divided into three categories: (1) unitized or homogeneous geogrids; (2) coated yarn-type geogrids; and (3) polyester and/or polypropylene rod or strap geogrids. Geogrids can also be classified into uniaxial, biaxial and triaxial types. Uniaxial geogrids are suitable for soil reinforcement applications in retaining walls and slopes, while biaxial and triaxial geogrids have been more commonly used for stabilization purpose in roadways. For the structures reinforced with uniaxial geogrids, design typically considers the geogrid properties related to the limit condition of the system, such as the tensile strength and the pullout resistance (Roodi, 2016). For multiaxial geogrids used for roadway stabilization, although designers have typically selected products based on the minimum requirement of properties of geogrid in isolation (e.g., ultimate tensile strength and tensile stiffness) (Archer and Wayne, 2012), the performance-based design is being evaluated by seeking an appropriate characterization of the soil-geogrid interaction under small displacements.

2.1.3 Test Methods for the Quantification of Soil-Geosynthetic Interaction

Researchers have adopted different test methods to quantify the soil-geosynthetic interaction, including the interface and the composite characteristics. As shown in Figure 2.1(a), a traditional test method has been the interface direct shear test, from which the

interface friction angle can be determined (Moraci et al., 2014; Vieira et al., 2013; Liu et al., 2009; Lee and Manjunath, 2000). Boundary conditions may influence test results, especially for small shear boxes (Palmeira, 2007).

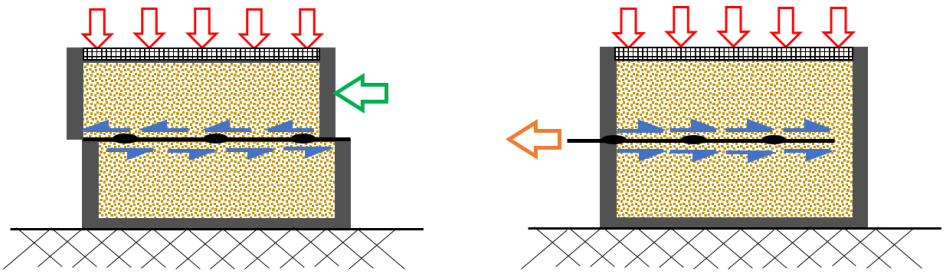

(a) Interface Direct Shear Test (b) Pullout Test

Figure 2.1: Test methods for the characterization of soil-geosynthetic interaction: (a) sketch of interface direct shear test; (b) sketch of pullout test (not to scale)

As shown in Figure 2.1(b), pullout test is another test method that has been used to evaluate the soil-geosynthetic interaction. (e.g., Roodi, 2016; Sukmak et al. 2015; Abdi and Zandieh 2014). This test type, however, has difficulty in determining the interface shear stress and relating it to the soil-geosynthetic relative displacement (Perkins and Cuelho, 1999). Consequently, it has been used primarily to study the anchorage strength of geosynthetics (Palmeira, 2007). Nevertheless, complemented by reasonable assumptions of interface conditions, pullout tests can be effectively utilized to characterize the soil-geosynthetic composite. For example, by assuming rigid-perfectly plastic response for the interface shear, Zornberg and Gupta (2010) identified both the geosynthetic tensile characteristics and the interface shear behavior through a single parameter called the stiffness of the soil-geosynthetic composite, or K_{SGC} (Zornberg et al., 2017). Relying on K_{SGC}, soil-geosynthetic interaction tests, conducted using an equipment based on pullout

tests, can be conducted to assess the suitability of a geosynthetic product for the design of roadway base stabilization.

As shown in Figure 2.2, another adopted test method has been the triaxial compression tests, where geosynthetics are placed within cylindrical samples. Two types of triaxial tests that have been usually used in roadway projects are the monotonic triaxial test and the repeated loading triaxial test. Monotonic triaxial tests can measure the elastic modulus of the geosynthetic-stabilized sample at different strain levels and obtain its ultimate shear strength. Repeated loading triaxial tests, on the other hand, evaluate the permanent deformations of the soil-geosynthetic composite or measure its resilient modulus. These triaxial tests are well suited for the analytical modeling since the constitutive relationships are well established for triaxial loading condition (e.g., Yang & Han, 2012). However, the small scale of triaxial test samples makes the test results of questionable variance with the material properties under the filed condition. Nonetheless, triaxial tests, with their simplicity, repeatability and flexibility in controlling the stress states in the specimen, have often been used to evaluate the resilient response of the soil-geosynthetic composites (Ling & Tatsuoka, 1994).

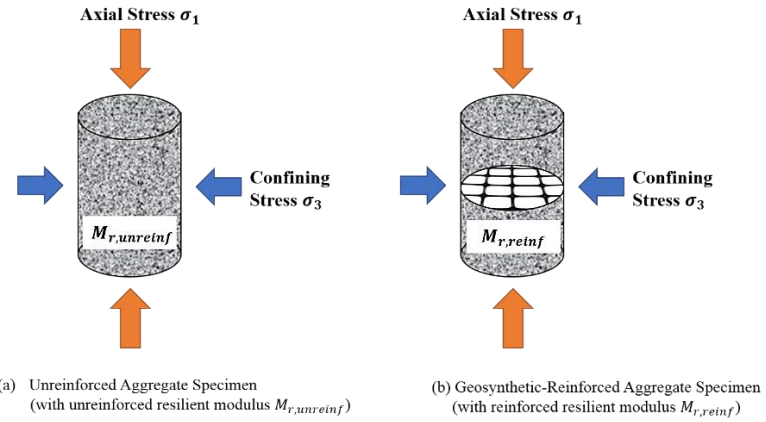

Figure 2.2: Sketches of triaxial compression tests: (a) unreinforced aggregate specimen; (b) geosynthetic-reinforced aggregate specimen

Last but not least, the performance of the geosynthetic-stabilized pavements has been evaluated using plate load tests, in which large-scale multilayer pavement sections are subjected to cyclic plate load. As shown in Figure 2.3, internal stresses, internal strains and surface deflection (rutting depth) can all be measured in plate load testing (e.g., Abu-Farsakh and Chen, 2011; Luo et al., 2017). Specialty sensors can be placed surrounding the soil-geosynthetic interface to directly measure the stress and strain distribution in both the base aggregate and geosynthetics. Therefore, plate loading testing, with a large-scale laboratory sample for sensor installation, is also a good test method for the characterization of soil-geosynthetic interaction.

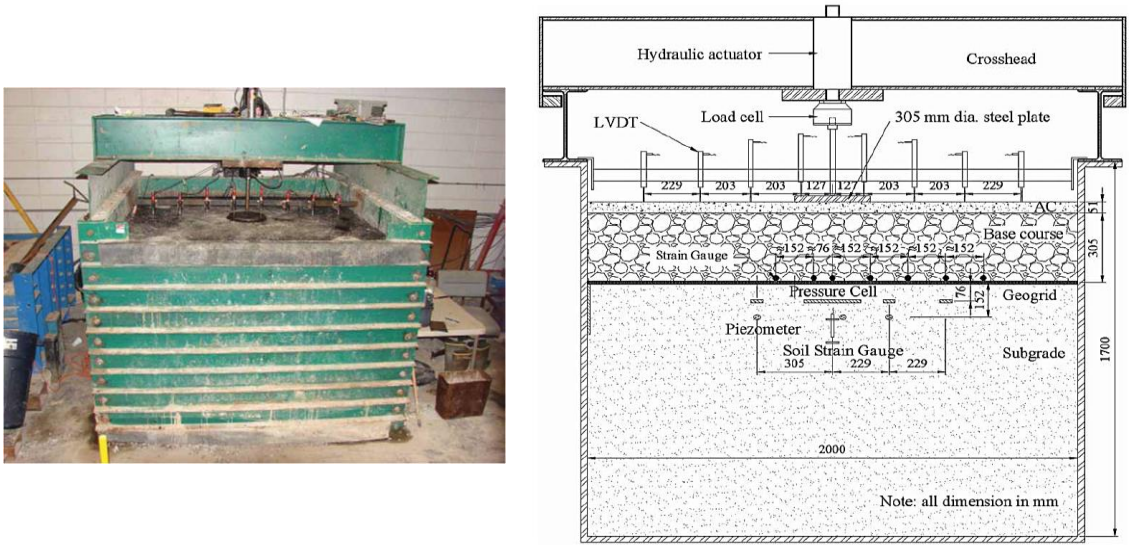

(a) Laboratory test box (b) Layout of sensors

Figure 2.3: Typical test setup and layout of sensors in the cyclic plate load testing (Abu-Farsakh and Chen, 2011)

The aforementioned test methods are all laboratory tests, the results of which are subjected to the influence of the boundary and sample dimensions. To better simulate the field conditions of the soil-geosynthetic interaction in real roadways, some full-scale tests have been developed. As shown in Figure 2.4, a representative full-scale test is the accelerated pavement testing (APT), which has been known as an effective method in evaluating pavement performances by applying controlled wheel loading under environmental conditions (Yang et al., 2012). Instead of obtaining index properties of geosynthetics, pavement layer materials or soil-geosynthetic composites, APT is a performance-based method. The pavement permanent deformation can be estimated through APT with comparatively high accuracy compared to small-scale laboratory tests. As a result, empirical models of the pavement permanent deformation are usually developed and calibrated using APT data (Hugo & Martin, 2004). However, full scale tests

such as APT are expensive and time-consuming so they have been mainly used for research or establishing industry standards (e.g., Al-Qadi et al., 2008, Al-Qadi et al, 2012).

(a)

(b)

Figure 2.4: APT facilities: (a) Linear test track (LINTRACK, Delft, Netherlands); (b) Circular test track (LCPC, France)

In summary, in the evaluation of soil-geosynthetic interaction in roadway systems, the principle of adopting a certain test method is to pursue the test results' reasonable correlation with the field performance while producing practical inputs for the prevailing pavement design methods. Efforts to fulfil this goal are currently under way.

2.1.4 Mechanisms involved in Geosynthetic Stabilization

The improvement in pavement performance due to the geosynthetic stabilization of base and subgrade has been attributed to three main mechanisms, including (1) lateral restraint; (2) increased bearing capacity; and (3) the tensioned membrane effect (Giroud and Noiray, 1981; Giroud et al., 1984; Perkins and Ismeik, 1997; Holtz et al., 1998). In a specific geosynthetic application in roadways, only certain mechanisms will be triggered.

As mentioned earlier, geosynthetics, if used for subgrade stabilization (usually in unpaved roads), will be placed at the base-subgrade or subbase-subgrade interface to

improve the stability of the soft subgrade soil. Although lateral restraint also plays a role, increased bearing capacity and tensioned membrane effect are the special mechanisms in such cases where comparatively large deformations are required to mobilize the geosynthetic strength (Giroud et al., 1985; Berg et al., 2000; Giroud and Han, 2004). As shown in Figure 2.5(b), the geosynthetic increases the bearing capacity of the subgrade by forcing the potential bearing surface failure plane to develop at an alternate higher shear strength surface (Gupta, 2009). Consequently, the bearing failure mode of the subgrade may change from punching failure to general failure due to geosynthetic reinforcement. On the other hand, in the tensioned-membrane mechanism (Figure 2.5(c)), the geosynthetic is stressed due to the depression basin created by the wheel load causing the geosynthetic to act as tensile support in the vertical direction, reducing the stresses applied to the subgrade soil and meanwhile increasing its bearing capacity (Cox et al., 2011). Nevertheless, large enough deformations together with high-stiffness geosynthetics are required for this tensioned-membrane mechanism to work.

When it comes to geosynthetic base stabilization, the governing mechanism is lateral restraint as illustrated in Figure 2.5(a). Lateral restraint describes the ability of the geosynthetic to confine aggregate particles within the plane of the material (Archer, 2008). The vertical traffic load induces lateral forces, which spread the aggregate particles and lead to local deformations of the fill (Cox et al., 2011). Owing to the frictional interaction and interlocking between the fill material and the geosynthetic, the

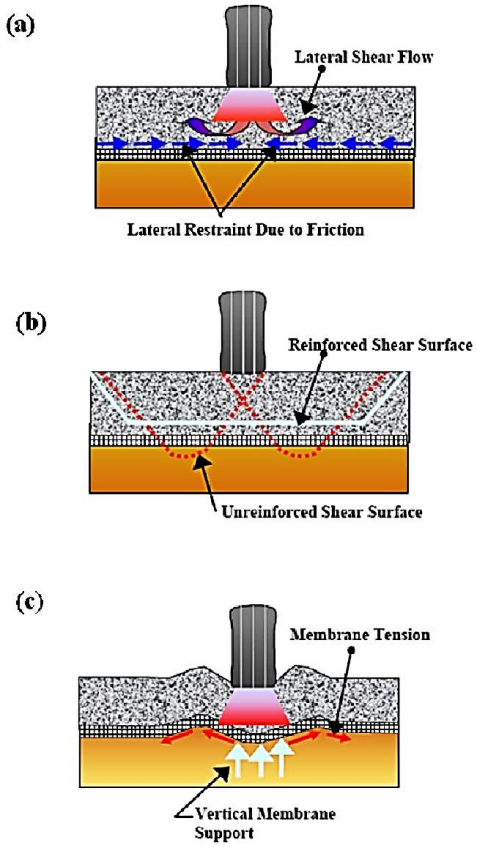

Figure 2.5: Stabilization mechanisms induced by geosynthetics (Holtz et al., 1998): (a) Lateral restraint; (b) Increased bearing capacity; and (c) Tensioned-membrane support

aggregate particles are restrained at the soil-geosynthetic interface (Hufenus et al., 2006). The soil-geosynthetic interaction transmits tensile forces from aggregates to the geosynthetic and, in turn, the tensioned geosynthetic applies additional lateral confinement to the aggregates. This mechanism yields a stiffening effect on the granular material surrounding the geosynthetic, which results in an increase in modulus of the reinforced layer (Archer, 2008). Other benefits brought by this mechanism to the stabilized base course include the decrease in vertical and horizontal strains and the improvement in load distribution. It is worth mentioning that the vertical stress and strain, as well as shear stress,

in the subgrade are also reduced through lateral restraint (Maubeuge and Klompmaker, 2011). This mechanism, also referred to as shear resisting interface, does not imply the need for significant rut depths to form and therefore is of unique interest for permanent paved roads (Maubeuge and Klompmaker, 2011; Hufenus et al., 2006).

2.2 DESIGN OF GEOSYNTHETIC STABILIZED BASES

2.2.1 Existing Design Methods for Flexible Pavements

For flexible pavements constructed without the addition of geosynthetics, the design method started with empirical ones, but they have been gradually evolving towards the mechanistic-empirical ones. Systematic research on the design methodology of pavements was first motivated by the American Association of State Highway Officials (AASHO) Road Test (1958-1960), which was the largest road experiment of its time and was initiated to evaluate the performance of highway pavements under moving loads with known magnitude and frequency (HRB, 1961). An important outcome from the AASHO Road Test was the development of equivalent single axle loads (ESALs) (Pedersen, 2007). From the 1960s to the 1990s, several versions of AASHTO guides for the design of pavements were released following the completion of the AASHTO Road Test (AASHTO, 2015). Among them, although still empirical, the 1993 AASHTO guide is one of the most widely used methods for flexible pavement design in the United States. Following the 1993 ASHTO guide, the next milestone in the development of pavement design methodology is the NCHRP Project 1-37A (1998-2004), named *Guide for the Design of New and Rehabilitated Pavement Structures*. The outcome of this project was a research document and rudimentary software for designing pavements using mechanistic-empirical procedures (ARA, 2004). Based on the results of the NCHRP Project 1-37A, in 2008, AASHTO released an interim edition of the *Mechanistic-Empirical Pavement Design*

Guide, A Manual of Practice (*MEPDG)*. In 2011, AASHTO released the first version of *DARWin-ME*, rebranded to *AASHTOWare Pavement ME Design*™, which is a commercial pavement design software that expands and improves the features of the prototype computational software developed as part of the NCHRP Project 1-37A (AASHTO, 2015). The latest version of MEPDG was released in 2015, and its supporting design tool, the up-to-date version of *AASHTOWare Pavement ME Design*™*,* is available on the AASHTO website.

The AASHTO Guide for Design of Pavement Structures (1993) considers the pavement to be multi-layer elastic system with an overall structural number (SN), as defined for flexible pavements using the following equation:

$$SN = a_1 D_1 + a_2 D_2 m_2 + a_3 D_3 m_3 \quad (2.1)$$

where $a_i =$ the i^{th} layer coefficient, $D_i =$ the i^{th} layer thickness (inches), and $m_i =$ the i^{th} layer drainage coefficient. The first layer is the asphalt layer, the second layer is the base course, and the third layer, if applicable, is the subbase course. The structural number is an abstract number indicative of the structural strength of a pavement required by a given combination of soil support (e.g., subgrade resilient modulus), total traffic expressed in ESALs, terminal serviceability, and environment (AASHTO, 1993). Accordingly, the required SN is calculated based on the above factors using the following empirical equation:

$$\log(W_{18}) = Z_R \times S_o + 9.36\log(SN+1) - 0.20 + \frac{\log\left(\frac{\Delta PSI}{4.2-1.5}\right)}{0.40+\frac{1094}{(SN+1)^{5.19}}} + 2.32\log(M_R) - 8.07 \quad (2.2)$$

Where $W_{18} =$ predicted number of 18-kip equivalent single axle load applications, $Z_R =$ standard normal deviate, $S_o =$ combined standard error of the traffic prediction and performance prediction, $\Delta PSI =$ difference between the initial design serviceability index, p_o, and the design terminal serviceability index, p_t, and $M_R =$ subgrade resilient

modulus (psi). After determined from Equation (2.2), the structural number must be converted to actual thicknesses of asphalt, base and subbase layers through Equation (2.1), by assigning appropriate layer coefficients representing the relative stiffness of the layer materials (AASHTO, 1993).

The 1993 AASHTO guide is simple and practical, but its design reliability is limited since the empirical observations and correlations adopted in this guide may or may not be applicable for a specific pavement project. Considering the empirical methods' limitations and the advances in computer and pavement technology, the movement to a mechanistic-empirical based pavement design procedure is fitting and desirable (AASHTO, 2015). The release of MEPDG by AASHTO is a critical step in this attempt. The "mechanistic" portion of MEPDG calculates the critical pavement responses (e.g., stresses and strains) using elastic layered theory with the traffic loading conditions and the pavement material properties used as inputs. Subsequently, the "empirical" portion relates those critical pavement responses to the development of observed distresses (e.g., rutting, cracking, international roughness index (IRI)) (AASHTO, 2015). According to the latest edition of MEPDG (AASHTO, 2015), the basic steps of the MEPDG design process are listed as follows:

1. Select a trial design cross section of the pavement;
2. Select the appropriate performance indicator criteria (threshold value) and design reliability level for the project;
3. Select the hierarchical level when obtaining the inputs, including general project information, design criteria, traffic, climate, structure layering, and material properties;
4. Run *AASHTOWare Pavement ME Design*™ software and examine the inputs and outputs for engineering reasonableness;

5. Revise the trial design, as needed.

Under such a sophisticated framework, MEPDG makes it possible to select cost-effective layer materials and thicknesses while ensuring that specific distress types can be limited to values less than the failure criteria within the design life of the pavement structure (AASHTO, 2015). However, the practicality of the mechanistic-empirical method is limited by the significant time and effort required to determine all the inputs, especially when traffic, climate and environmental conditions impose a comprehensive influence.

2.2.2 Approaches to Incorporating the Geosynthetic Influence into Pavement Design

The geosynthetic influence on the stabilization of base course would ideally be quantified in such a way that it can easily be incorporated into the existing design methodologies of flexible pavements. Since the AASHTO guide (1993) and MEPDG are the two prevailing methods in the United States, the quantification of geosynthetic influence usually needs to be compatible with either of these methods. Improvement ratio approaches have been usually applied to the empirical pavement design (AASHTO guide 1993), while equivalent property approaches have been typically used for the mechanistic-empirical pavement design (MEPDG). Some researchers have also attempted to include some new design procedures as a complement to the existing MEPDG. An overview of some typical studies about this topic is provided in this section.

2.2.2.1 Improvement Ratio Approaches

The purpose of geosynthetic base stabilization in flexible pavements has been to extend its service life (Al-Qadi et al., 1997, Cancelli and Montanelli, 1999; Wasage et al., 2004) or to lower the cost of base materials by reducing the base course thickness (Montanelli et al., 1997, Cancelli and Montanelli, 1999). Because the AASHTO guide

(1993) has been widely used since its release, early research efforts on benefit quantification of geosynthetics focused on modifying Equations (2.1) and (2.2) to reflect the geosynthetic influence. Specifically, different forms of improvement ratios have been defined. The typical ones include Traffic Benefit Ratio (TBR), Base Course Reduction (BCR) and Layer Coefficient Ratio (LCR). Definition of each of them will be discussed next.

Traffic Benefit Ratio (TBR), as per Berg et al. (2000), is defined as a ratio of the number of load cycles on a reinforced section to reach a certain failure criterion to the number of load cycles on an unreinforced section, with the same geometry and material constituents, to reach the same failure criterion. TBR is sometimes referred to as Traffic Improvement Factor (TIF). A concise expression of TBR is provided below:

$$\text{TBR} = \frac{N_{f,r}}{N_{f,u}} \tag{2.3}$$

When applied to Equation (2.2), TBR extends the service life of geosynthetic stabilized pavement in terms of an increased W_{18} as follows:

$$W_{18(with\ geosynthetic)} = \text{TBR} * W_{18(without\ geosynthetic)} \tag{2.4}$$

Base Course Reduction (BCR), as per Berg et al. (2000), is defined as the percent reduction in the reinforced base, or subbase, thickness from the unreinforced thickness, with the same material constituents, to reach the same failure criterion, as follows:

$$\text{BCR} = \frac{T_u - T_r}{T_u} \times 100\% \tag{2.5}$$

where $T_u =$ the thickness of the base course without geosynthetic stabilization, $T_r =$ the thickness of geosynthetic stabilized base course. Obviously, if BCR was known, using Equation (2.5) would be the easiest way to calculate the reduced base course thickness.

Layer Coefficient Ratio (LCR) is a modifier applied to the layer coefficient of the base or subbase layer. Unlike TBR and BCR, which are directly obtained from tests, LCR is an empirical parameter specially derived for the use in the AASHTO empirical method (e.g., Guide 1993). If the geosynthetic is placed within the base course, the role of LCR in structural numbers is shown by the following equations:

$$SN_u = a_1 \cdot D_1 + a_2 \cdot D_2 \cdot m_2 + a_3 D_3 m_3 \tag{2.6}$$

$$SN_r = a_1 \cdot D_1 + (\text{LCR} \cdot a_2) \cdot D_2 \cdot m_2 + a_3 D_3 m_3 \tag{2.7}$$

$$SN_u = a_1 \cdot D_1 + (\text{LCR} \cdot a_2) \cdot D_2' \cdot m_2 + a_3 D_3 m_3 \tag{2.8}$$

Where $SN_u =$ the structural number of the flexible pavement without geosynthetics, $SN_r =$ the structural number of flexible pavements with geosynthetic stabilized base course, and $D_2' =$ the reduced base course thickness due to geosynthetics. Other parameters maintain the same meanings as in Equation (2.1). Equation (2.8) indicates that with the geosynthetic and the corresponding LCR, the flexible pavement with the reduced base course thickness can still handle the same structural number (i.e., the same ESALs) as the unreinforced pavement.

Based on equation (2.6) and (2.7), if SN_r is obtained from Equation (2.2) using the $W_{18(with\ geosynthetic)}$ in Equation (2.4), LCR can be expressed as follows:

$$\text{LCR} = \frac{SN_r - a_1 \cdot D_1 - a_3 D_3 m_3}{SN_u - a_1 \cdot D_1 - a_3 D_3 m_3} \tag{2.9}$$

After LCR has been obtained using Equation (2.9), D_2' can be calculated from Equation (2.8) as follows (Han, 2015[44]):

$$D_2' = \frac{SN_u - a_1 \cdot D_1 - a_3 D_3 m_3}{LCR \cdot a_2 \cdot m_2} \tag{2.10}$$

It should be noticed that the basis of LCR is TBR. Since TBR only indicates the increase in the number of loading cycles to the failure state, LCR works as a convenient

tool to incorporate the TBR results into the AASHTO empirical method (e.g., Guide 1993) to get the equivalent reduction of base course thickness. Consequently, in the design software developed based on AASHTO Guide 1993 by geosynthetic manufacturers, LCR calculated from a database of TBR is ultimately used to predict the reduced base course thickness for the users.

As indicated in the preceding discussion, the use of the improvement ratio approach requires experimental data to define TBR or BCR. Accelerated pavement testing (APT) is commonly adopted to measure these ratios. The improvement ratio approach is also known as an "approved product list approach" since TBR and BCR are considered geosynthetic product, and test conditions, specific (Berg et al., 2000). Consequently, significant effort is needed to establish a comprehensive database for these ratios, and the practicality of this approach is limited accordingly. Currently, design of geosynthetic stabilized flexible pavements using TBR or BCR is mostly assisted by the design software provided by the geosynthetic manufacturers, e.g., SpectraPave4-PRO^{TM} from the Tensar Corporation. However, the reliability of the design result will depend highly on the accuracy of the TBR or BCR database, so careful verification is usually required.

2.2.2.2 Equivalent Property Approaches

In the design of geosynthetic stabilized bases, another approach to incorporating the geosynthetic influence is to replace a certain mechanical property of the natural aggregate material with an equivalent improved value. This approach can be conveniently applied to the mechanistic-empirical design by modifying the material property inputs. The primary parameters used in MEPDG to characterize the base course are the resilient modulus and Poisson's ratio. Few studies have focused on changes in Poisson's ratio due to the addition of geosynthetics, since the resulting thickness designs are largely insensitive

to Poisson's ratio (within typical ranges) (AASHTO, 2015). Consequently, the ideal equivalent property is the improved resilient modulus of the geosynthetic-stabilized base course. However, the resilient modulus is stress-dependent, and MEPDG requires it to be determined using the generalized constitutive model developed from the NCHRP Project 1-28A (Witczak, 2003), as follows:

$$M_r = k_1 P_a \left(\frac{\theta}{P_a}\right)^{k_2} \left(\frac{\tau_{oct}}{P_a} + 1\right)^{k_3} \tag{2.11}$$

where $M_r =$ resilient modulus (psi);

$\theta =$ bulk stress = $\sigma_1 + \sigma_2 + \sigma_3$;

$\sigma_1 =$ major principal stress;

$\sigma_2 =$ intermediate principal stress (= σ_3 for M_r test on cylindrical specimen);

$\sigma_3 =$ minor principal stress (confining pressure);

$\tau_{oct} =$ octahedral shear stress

$$= \frac{1}{3}\sqrt{(\sigma_1 - \sigma_2)^2 + (\sigma_1 - \sigma_3)^2 + (\sigma_2 - \sigma_3)^2}$$

$P_a =$ atmospheric pressure;

$k_1, k_2, k_3 =$ regression constants.

In each stress sequence of the resilient modulus test, M_r is calculated using the following Equation (2.12), and k_1, k_2, k_3 are obtained by fitting the resilient modulus test data to Equation (2.11).

$$M_r = \frac{\sigma_d}{\varepsilon_r} \tag{2.12}$$

where $\sigma_d =$ the cyclic deviatoric stress and $\varepsilon_r =$ the resilient strain.

Such a way of defining and determining the resilient modulus makes it hard to analytically derive the improved resilient modulus in a direct manner. Responding to this issue, Yang and Han (2012) proposed an analytical solution for the improved resilient

modulus through the quantification of the additional confining stress caused by the geosynthetic. More specifically, Yang and Han's (2012) model solves for the additional confining stress $\Delta\sigma_3$, since Equation (2.11) is still adopted to calculate the resilient modulus while the confining stress is updated by including $\Delta\sigma_3$. This model relates $\Delta\sigma_3$ to the geosynthetic tension and displacement, analyzes the geosynthetic as a planar element, and runs iteration to ultimately solve $\Delta\sigma_3$. In summary, this model is supported by a rigorous theoretical derivation, but considerable amount of calculation is required to obtain $\Delta\sigma_3$.

Some researchers have also been exploring other appropriate properties to characterize the soil-geosynthetic composite. A representative property that has been proposed by Zornberg et al. (2017) includes the stiffness of the soil-geosynthetic composite (K_{SGC}), which is obtained using an analytical model referred to as the soil-geosynthetic composite (SGC) model. The SGC model evaluates the confined load-strain characteristics of the soil-geosynthetic composite under small displacements using results from a soil-geosynthetic interaction device, which adopted the configuration of a pullout test (Zornberg and Gupta, 2010). It considers the confined geosynthetic stiffness (J_c) and the interface yield shear stress (τ_y) as two important parameters governing the soil-geosynthetic interface behavior. The two parameters have been combined to define a unique coefficient (K_{SGC}) to characterize the soil-geosynthetic interaction under small displacements, as shown by the following expression:

$$K_{SGC} = 4 \cdot \tau_y \cdot J_c \tag{2.13}$$

With this parameter, as per Zornberg et al. (2017), the relationship between the geosynthetic unit tension and the geosynthetic displacement can be described as follows:

$$T_{(x)}^2 = K_{SGC} \cdot u_{(x)} \tag{2.14}$$

The SGC model has clear formulations, and the parameter K_{SGC} can be readily measured through the soil-geosynthetic interaction tests, especially small-scale ones. In addition, K_{SGC} is related to small displacements. All these characteristics make it particularly suitable for specifications and the design of structures such as stabilized roadways (Zornberg et al., 2017). However, K_{SGC} cannot be incorporated directly into the current MEPDG. As mentioned earlier, the governing property input of the base course in MEPDG is the resilient modulus. Therefore, a reasonable relationship with the resilient modulus is required for K_{SGC} to be practically used in the design of geosynthetic-stabilized bases.

2.2.2.3 Development of New Design Procedures

The current MEPDG is a complete system if used for the design of pavements with natural layer materials. However, with the addition of geosynthetics, effort is needed to modify the mechanistic-empirical design procedures in MEPDG. Without doubt, updating the MEPDG, especially its empirical pavement performance model and design software, is a long-term systematic work, so the current attempt is still limited to proposing the appropriate procedures to obtain the equivalent improved property, with other MEPDG components remaining the same as before. One representative study is the NCHRP Project 01-50 completed by Luo et al. (2017) at the Texas A&M Transportation Institute.

In the study reported by Luo et al. (2017), as shown by Figure 2.6, triaxial tests were conducted to develop a new permanent deformation model and determine the cross-anisotropic properties of base material, both of which were prepared to serve the quantification of the additional confining stress $\Delta\sigma_3$ (developed using Yang & Han model (2012) as a basis). Subsequently, the determined $\Delta\sigma_3$ worked as an input into the finite element modeling, whose results were generalized to develop Artificial Neural Network

(ANN) models of critical strains and stresses in pavements (Luo et al., 2017). Finite element computations were also modified to match the results of their full-scale laboratory testing of typical asphalt and concrete pavement sections in an instrumented large-scale tank (LST) (Luo et al., 2017). Based on their ANN models, a computer program called "Composite Geosynthetic-Base Course Model" was developed to determine the improved base course property inputs for the design software (*AASHTOWare Pavement ME Design*™) in MEPDG. The researchers also claimed that this computer program could be incorporated into MEPDG Pavement ME Design software with good compatibility.

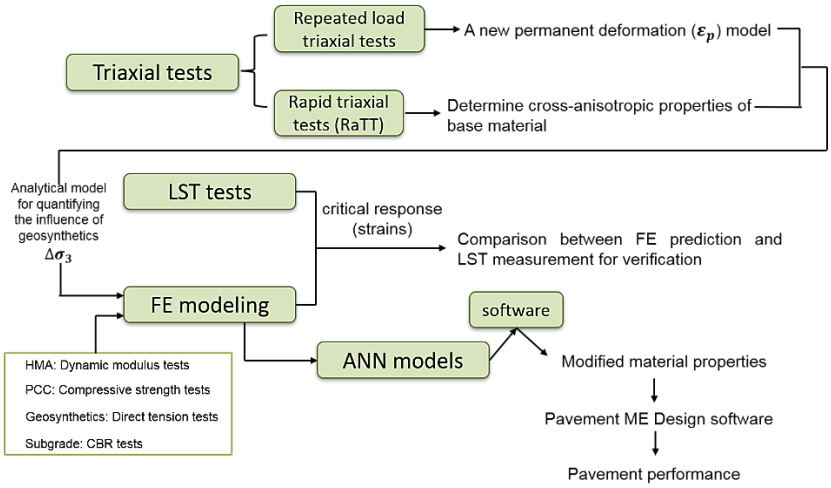

Figure 2.6: Summarized flow chart of Luo et al. (2017) study

It can be noticed that Luo et al. (2017) proposed procedures to quantify the additional confining stress and the equivalent improved base course property, while the prediction of pavement performance is still completed by the existing software (*AASHTOWare Pavement ME Design*™) in MEPDG. Accordingly, it is still within the range of the equivalent property approach.

Concerning the future development of new design procedures, the geosynthetic benefit may be considered in the form of the improvement in pavement performance instead of the change in mechanical properties of materials. Pavement performance includes the development of rutting and cracking, which are predicted in the current mechanistic-empirical design guideline using empirical equations. Since the geosynthetic inclusion may retard the development of rutting and cracking (Moghaddas-Nejad and Small, 1996; Kinney et al., 1998), this time effect should be evaluated to update the existing models of pavement performance. Performance data collected from in-service geosynthetic-stabilized roadways or from full-scale laboratory tests of geosynthetic-stabilized base materials may contribute to the modification of performance models. Consequently, the design procedures will be updated together with the modified performance models. Such a research direction constitutes another way of incorporating geosynthetic effect into mechanistic-empirical pavement design. Apparently, this direction is complex and requires additional studies.

Chapter 3: Analytical Model for Geosynthetic Stabilized Bases

3.1 INTRODUCTION

The framework of this analytical model is established based on the elasticity theory and the soil-geosynthetic composite (SGC) model. The base course material is assumed to be homogeneous, isotropic and linearly elastic, and the deformations are assumed to be small. Therefore, the base course response under the wheel load was analyzed using the elasticity theory. Specifically, the roadway was simplified as an infinitely long elastic solid subjected to a continuous strip load along the wheel path. Hence, a plane strain problem was considered with zero longitudinal displacement. However, when a geosynthetic layer is included as an additional component in the pavement system, the complex soil-geosynthetic interaction cannot be easily addressed using the elasticity theory. Therefore, a soil-geosynthetic interaction model (SGC model) was used to incorporate the geosynthetic contribution into the framework of elasticity theory.

The soil-geosynthetic composite (SGC) model expresses the geosynthetic unit tension as a function of the geosynthetic displacement using the stiffness of the soil-geosynthetic composite or K_{SGC}. The additional lateral restraint provided by the geosynthetic in the base course can be attributed to the tension developed in the geosynthetic. In this study, the additional lateral restraint provided by the geosynthetic was modeled as a uniform additional confining stress within the geosynthetic influence zone. The geosynthetic unit tension divided by the thickness of its influence zone defines the additional confining stress. As a direct indicator of the geosynthetic influence, this additional confining stress was then used in the stress-displacement relationship in the elasticity theory. Subsequently, an equivalent increased elastic modulus of the base course was estimated based on the additional confining stress. The increased modulus can be used

as an updated property for the geosynthetic-stabilized layer in the mechanistic-empirical pavement design procedures.

The analytical model proposed in this study was developed considering three different cases of a base course. Case 1 is a control section, which considers a base course without geosynthetic with an elastic modulus of E_u; Case 2 is a geosynthetic-stabilized section with the original base elastic modulus E_u in which the geosynthetic influence is represented by an additional confining stress; and Case 3 is considered equivalent to Case 2, except that the geosynthetic influence is represented by an increased base elastic modulus (E_r instead of E_u) while no additional confining stress is considered. The quantification and evaluation of the geosynthetic influence are conducted under the framework of these three simplified pavement sections. Together with the elasticity theory and the SGC model, these three cases serve as the basis for all the following derivations and comparisons.

3.2 MODELING PHILOSOPHY

3.2.1 Assumptions from the Theory of Elasticity

The theory of elasticity governs the behavior of bodies that recover their initial state when the loads which produce deformations are removed (Maceri, 2010). An ideal research object in the theory of elasticity should be homogeneous, isotropic and linearly elastic with small deformation under loading. A realistic base course material, however, is not an ideal elastic material. Consequently, the following assumptions were made regarding the base course material so that it can be analyzed using the elasticity theory:

(1) The base course material is a continuous mass, rather than a medium of discrete particles, so that the physical quantities such as stresses, strains and displacements can be expressed using continuous functions.

(2) The base course material is perfectly elastic, which follows Hook's law of elasticity, namely the linear relationship between stress and strain components.

(3) The base course material is homogeneous. In other words, the elastic properties are the same throughout the body and the elastic constants are independent of the location in the material.

(4) The base course material is isotropic so that the elastic properties are the same in all directions. The elastic constants in this isotropic body are independent of the orientation of the coordinate axes.

(5) The displacements and strains in the base course material are small. Under loading conditions, the displacement components in all points of the base course are very small compared to the dimensions of the base.

For compatibility, in the case of a geosynthetic-stabilized base course, the aforementioned assumptions also apply to the geosynthetic.

The above assumptions may not be fully consistent with the actual characteristics of the unbound granular material in the base course. However, the purpose of this study was to generate a closed-form analytical solution to quantify the geosynthetic influence, so idealization and simplification of the base course materials are necessary. Considering that the base course in pavements is usually well compacted, the stiffness of granular materials is comparatively large, and the wheel load is of comparatively small magnitude when reaching the base course, the above assumptions are still acceptable when evaluating the base course response under traffic loading. In addition, the evaluation focuses more on the relative improvement in the base elastic modulus, and the relative change in modulus is less affected by whether the base material rigorously complies with the assumptions of elasticity. In other words, since the control section and the geosynthetic-stabilized section

are evaluated based on the same elasticity assumptions, the increase in base elastic modulus can serve as a reasonably good estimate for the stabilization effect of the geosynthetic.

3.2.2 Plane Strain Condition

The analytical model presented in this study considers an infinitely long roadway along the travelling direction of the traffic. To be consistent with this geometric condition, the wheel load was simplified as a uniform strip load along the wheel path. Considering these assumptions, a base course that is subjected to small deformations induced by the traffic load was solved as a two-dimensional elastic problem under a plane strain condition.

In a plane strain problem, one dimension is significantly larger than the others. As shown in Figure 3.1, an arbitrary cross section of the roadway can be selected as the *xy* coordinate plane, while the longitudinal line at the center of the wheel path was selected as the *z* axis. Under plane strain conditions, the principal strain along the longitudinal dimension is constrained and thus can be assumed zero. Although the principal stress along the longitudinal dimension is non-zero, this stress can be disregarded in calculations. Specifically, under plane strain conditions, all stress, strain and displacement components do not change along the z axis, which allows a two-dimensional analysis to be carried out for the cross section. In other words, stresses, strains and displacements in the cross section are functions of only the *x* and *y* coordinates.

An alternative approach involves treating the base course section as a three-dimensional system represented by a cylinder under triaxial loading. Such assumption increases the complexity of the problem while the sample dimension and stress conditions are only comparable to small-scale laboratory tests rather than the realistic roadway situations. The plane strain condition adopted in the proposed model in this study, however,

has advantages of being simple, realistic and comparatively convenient for the model framework to be established and for the geosynthetic influence to be involved.

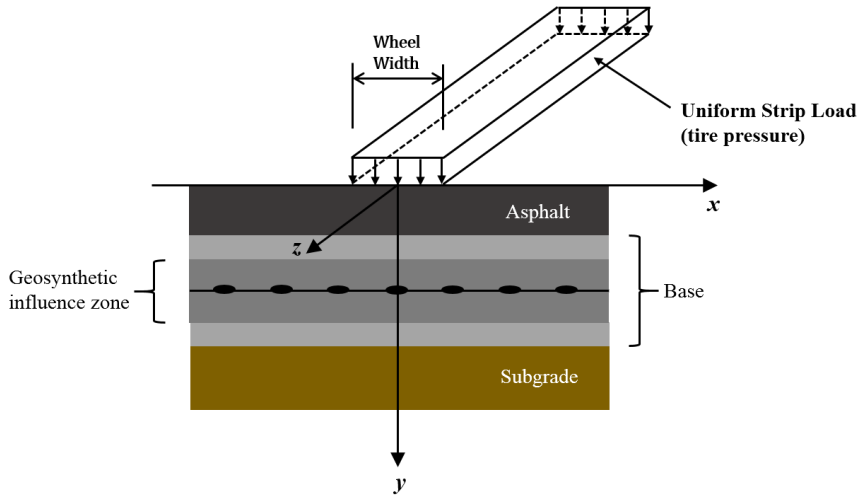

Figure 3.1: Coordinate system of the roadway section considered in this study

3.2.3 Governing Equations

In a two-dimensional elastic problem, the governing equations include three categories. The first category is related to the force equilibrium in an arbitrary elastic element as shown in Figure 3.2. It determines the relationship between the normal stress and shear stress components, as shown in the following Equations (3.1) and (3.2):

$$\frac{\partial \sigma_x}{\partial x} + \frac{\partial \tau_{yx}}{\partial y} + f_x = 0 \tag{3.1}$$

$$\frac{\partial \sigma_y}{\partial y} + \frac{\partial \tau_{xy}}{\partial x} + f_y = 0 \tag{3.2}$$

where $\sigma_x =$ the normal stress parallel to the x axis, $\sigma_y =$ the normal stress parallel to the y axis, $\tau_{yx} =$ the shear stress perpendicular to the y axis while parallel to the x axis, and $\tau_{xy} =$ the shear stress perpendicular to the x axis while parallel to the y axis. It can be proved that $\tau_{xy} = \tau_{yx}$. For simplification, both shear stress components (τ_{xy} and τ_{yx})

will be represented by τ_{xy} in the following discussions. f_x and f_y are the internal forces per unit volume in the *x* and *y* directions, respectively. f_x is typically induced by a horizontal inertia force, while f_y is the force of gravity. However, the horizontal inertia force is not applicable to this problem, and the force of gravity was ignored due to its small magnitude compared to the wheel load. Ignoring gravity also allows a symmetrical stress condition on both sides of the mid-depth of the base course.

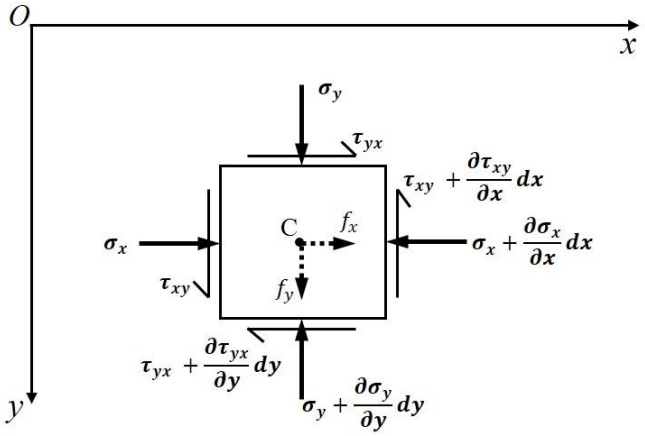

Figure 3.2: Stresses in an elastic element

The second category of governing equations concerns the relationship between strains and displacements. Based on the geometric analysis, the normal and shear strains can be related to the displacements in the *x* and *y* directions as follows:

$$\varepsilon_x = \frac{\partial u}{\partial x} \tag{3.3}$$

$$\varepsilon_y = \frac{\partial v}{\partial y} \tag{3.4}$$

$$\gamma_{xy} = \frac{\partial v}{\partial x} + \frac{\partial u}{\partial y} \tag{3.5}$$

where $u =$ the horizontal displacement (along the *x* axis), $v =$ the vertical displacement (along the *y* axis), $\varepsilon_x =$ the normal strain in the *x* direction, $\varepsilon_y =$ the normal strain in the *y* direction, and $\gamma_{xy} =$ the shear strain (change in a right angle composed by two lines

parallel to the *x* and *y* axes, respectively). As indicated by Equations (3.3) to (3.5), the strain components are derivatives of displacements, so the expressions of strains can be determined once the displacement functions are known. However, when strain components have been explicitly formulated, the displacement functions remain uncertain and have to be decided based on boundary conditions.

The third category of governing equations deals with the stress-strain relationship, namely the constitutive relationship. Unlike the preceding two categories of equations, which were valid for both plane stress and plane strain conditions, the stress-strain relationship shown by the following Equations (3.6) to (3.8) is valid only for a plane strain problem:

$$\varepsilon_x = \frac{1-\mu^2}{E}\left(\sigma_x - \frac{\mu}{1-\mu}\sigma_y\right) \tag{3.6}$$

$$\varepsilon_y = \frac{1-\mu^2}{E}\left(\sigma_y - \frac{\mu}{1-\mu}\sigma_x\right) \tag{3.7}$$

$$\gamma_{xy} = \frac{2(1+\mu)}{E}\tau_{xy} \tag{3.8}$$

where $E =$ the elastic modulus and $\mu =$ the Poisson's ratio. The eight unknowns appeared in the eight governing equations, including three stress components (σ_x, σ_y and $\tau_{xy} = \tau_{yx}$), three strain components (ε_x, ε_y and γ_{xy}), and two displacement components (*u* and *v*), can be solved by adopting boundary conditions.

A plane elasticity problem may be solved rigorously following two paths:

1) The displacement method, in which displacement components are considered as the essential unknowns and all other unknowns are expressed in terms of displacements. Once the functions of *u* and *v* are found using the equilibrium differential equations and the boundary conditions, strains and stresses can be back calculated.

2) The stress method, in which the stress components are considered as the essential unknowns with other unknowns expressed as the functions of stresses. In this case, the problem is solved by using the equations of compatibility, and it usually deals with the problems with only the stress boundary conditions.

This stress method was found not to be suitable for this study because apparent displacement boundary conditions needed to be considered. The displacement method, on the other hand, resulted in complicated mathematical expressions without closed-form analytical solutions. Consequently, a semi-inverse method was adopted in which specific functions for normal stress components (i.e., σ_x and σ_y) were assumed and strains and displacements were determined accordingly using the aforementioned governing equations.

3.2.4 Three Pavement Cases

As illustrated in Figure 3.3, three pavement cases were considered for evaluation of the influence of geosynthetic stabilization. Each case is a relatively simple pavement profile composed of hot mix asphalt, base and subgrade layers. Case 1 is a control section, where the base course has its original elastic modulus (E_u). Cases 2 and 3 are geosynthetic-stabilized sections with the geosynthetic placed at the mid-depth of the base course. The geosynthetic influence, however, is represented using different approaches in Cases 2 and 3. Specifically, within the geosynthetic influence zone of Case 2, the base material still has its original elastic modulus (E_u), but an additional confining stress ($\Delta\sigma_3$) is applied. In contrast, no additional confining stress is applied in Case 3, but the elastic modulus of the base material within the geosynthetic influence zone is increased to E_r. Indeed, the additional confinement from geosynthetic (considered in Case 2 by using $\Delta\sigma_3$) was assumed to be equivalent to an increased elastic modulus in the base layer (E_r in Case 3).

$\Delta\sigma_3$ can be calculated based on the tension developed in the geosynthetic. E_r, on the other hand, was solved as a value resulting in an equivalence between Case 2 and Case 3, for example by minimizing the displacement difference between the two cases.

Although the entire pavement profile is shown in the diagrams presented in Figure 3.3, only the geosynthetic influence zones are the objects of interest in the analysis using the theory of elasticity. It should also be noted that only one side of the pavement section that is located underneath the wheel load is presented in Figure 3.3. The *y* axis represents the central axis of a wheel load, which was assumed as an infinitely long strip load. The stress and strain induced by the wheel load was assumed to be symmetric with respect to this axis. The *x* axis, on the other hand, lies at the mid-depth of the base course.

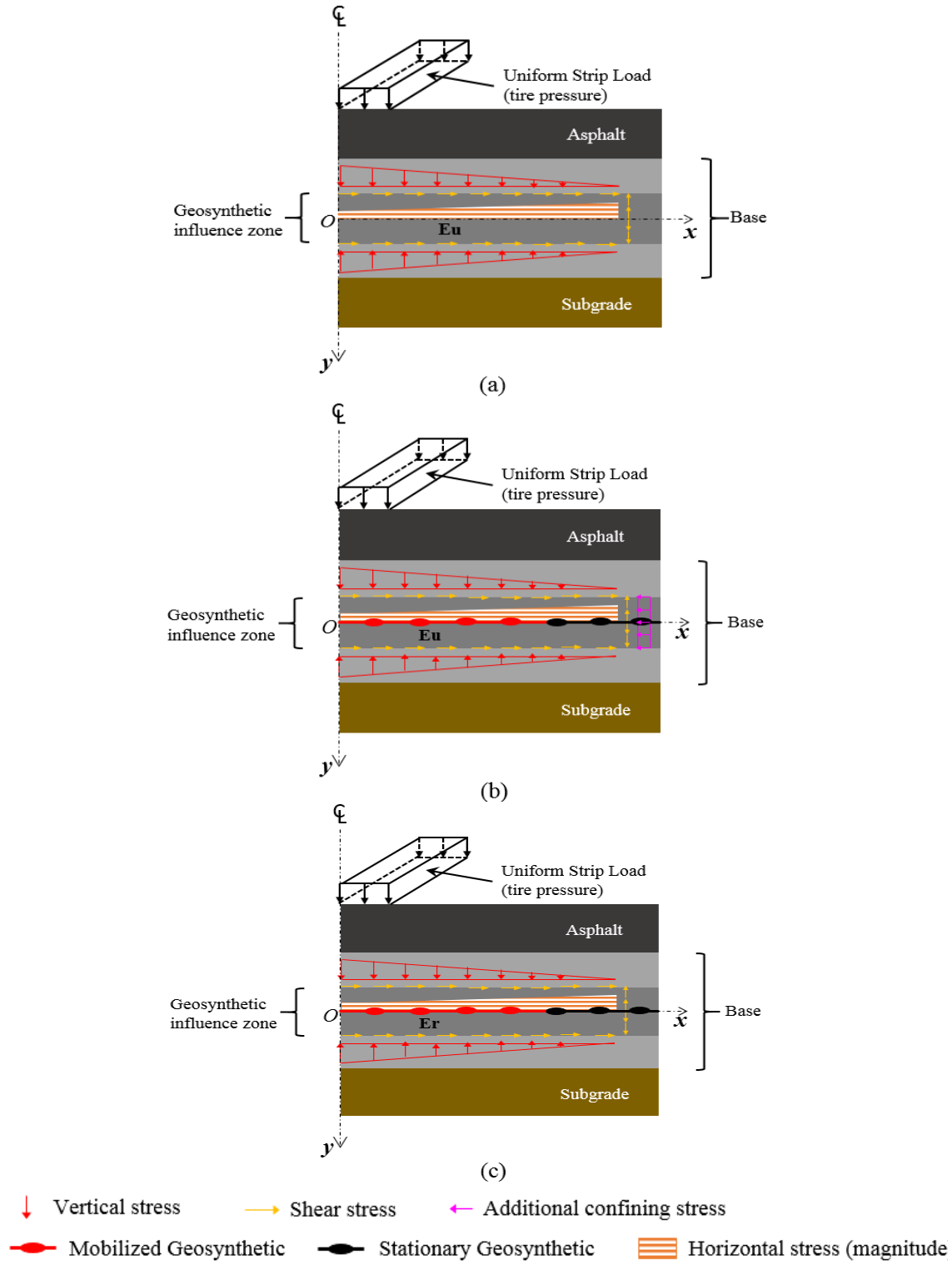

Figure 3.3: Diagram of Three Pavement Cases: (a) Case 1; (b) Case 2; (c) Case 3

3.3 DEVELOPMENT OF THE ANALYTICAL MODEL

3.3.1 Assumed Stress Conditions

As previously mentioned, the pavement cases were solved considering a semi-inverse method in which specific functions were assumed for the normal stress components and the strain and displacement components were then calculated. In the proposed model, linear functions were assumed for the normal stresses, and the resultant displacement expressions were similar to that adopted in the soil-geosynthetic composite (SGC) model, thereby facilitating incorporation of the SGC model into the framework developed using the theory of elasticity.

The linear normal stress expressions were assumed only for points located in the geosynthetic influence zone. Both the vertical and horizontal normal stress components are assumed to be linear functions, as follows:

$$\sigma_y = ax + b \tag{3.9}$$

$$\sigma_x = cx + d \tag{3.10}$$

where $\sigma_y =$ the vertical stress (parallel to *y* axis), $\sigma_x =$ the horizontal stress (parallel to *x* axis), and *a*, *b*, *c*, and *d* are stress constants. Consistent with the typical sign convention in the theory of elasticity, compressive vertical and horizontal stresses were assumed to be negative.

Constant *b* is the maximum vertical stress (at *x=0*) within the geosynthetic influence zone. It can be calculated based on the tire pressure (*p*) with the existing solution for the subsurface stress distribution under a strip load. Detailed procedures used to determine the *b* value are discussed in Appendix A.

To determine constant *a*, let *P* denote the known wheel load in kN/m. The wheel load is assumed to be represented by a strip load to be consistent with the plane strain

condition. If the tire pressure p is known, for example 35 psi for a sedan, and the wheel width is measured as W_w, then the wheel load P (kN/m) can be calculated using Equation (3.11), as follow:

$$P = p \cdot W_w \tag{3.11}$$

In the following discussion, as shown in Figure 3.1, only half of the symmetrical pavement section is analyzed. Along the x axis, let $x = L$ be the point where σ_y decreases to 0. In addition, the integral of the vertical stresses over the interval of [0, L] is equal to the half of the total wheel load. These two conditions, which can be used to determine L and a, are shown as follows:

$$aL + b = 0 \tag{3.12}$$

$$\int_0^L (ax + b)dx = a\frac{L^2}{2} + bL = -\frac{P}{2} \tag{3.13}$$

P is the absolute value of the wheel load, while the compressive stresses are negative. Consequently, a negative sign appears in Equation (3.13). By solving Equations (3.11) and (3.12) together, L and a can be expressed as follows:

$$L = \frac{-P}{b} \tag{3.14}$$

$$a = \frac{-b}{L} = \frac{b^2}{P} \tag{3.15}$$

Procedures to determine constants c and d in the assumed equation for σ_x are presented in Appendixes B and A, respectively. Specifically, c is determined using Equation (3.1) considering the equilibrium in the system, while d can be estimated using the elastic solutions for the subsurface stress distribution under a strip load.

Constants a, b, c and d, together with the traffic loading condition and pavement geometry, are marked in Figure 3.4. It should be noticed that the stress conditions are

assumed symmetrical on both sides of the x axis within the geosynthetic influence zone. This symmetry results from neglecting the gravity force in the base material.

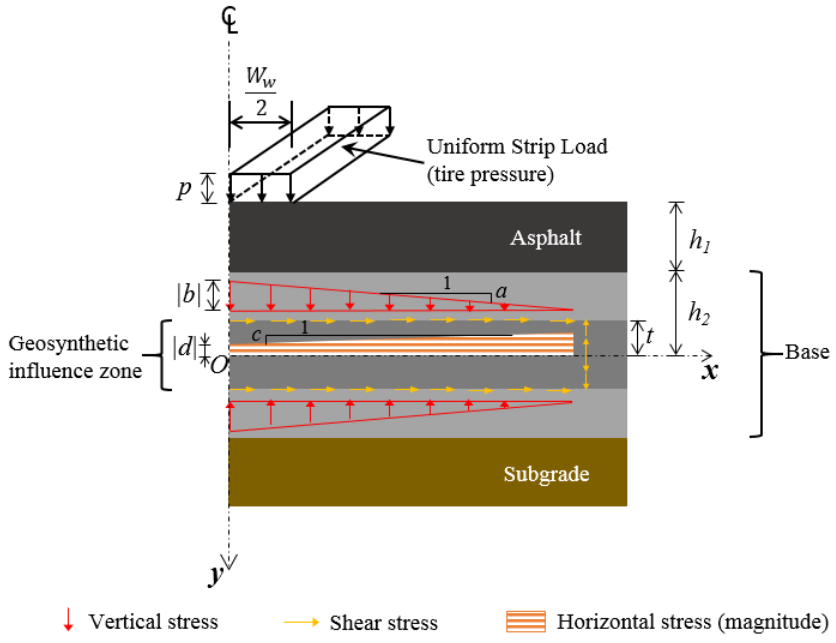

Figure 3.4: Constants a, b, c and d, traffic loading condition and layer thicknesses marked in the pavement profile

3.3.2 Derivation of Strain and Displacement Expressions

Based on the strain-stress and strain-displacement relationships in the plane strain problem, the expressions of strain and displacement components can be derived from those of the stress components. Specifically, substitution of Equations (3.9) and (3.10) into Equations (3.6) and (3.7) results in the explicit equations for ε_x and ε_y:

$$\varepsilon_x = \frac{1-\mu^2}{E}\left[\left(c - \frac{\mu}{1-\mu}a\right)x + d - \frac{\mu}{1-\mu}b\right] \tag{3.16}$$

$$\varepsilon_y = \frac{1-\mu^2}{E}\left[\left(a - \frac{\mu}{1-\mu}c\right)x + b - \frac{\mu}{1-\mu}d\right] \tag{3.17}$$

Then, according to Equations (3.3) and (3.4), the derivatives of horizontal and vertical displacement components are expressed as follows:

$$\frac{\partial u}{\partial x} = \frac{1-\mu^2}{E}\left[\left(c - \frac{\mu}{1-\mu}a\right)x + d - \frac{\mu}{1-\mu}b\right] \tag{3.18}$$

$$\frac{\partial v}{\partial y} = \frac{1-\mu^2}{E}\left[\left(a - \frac{\mu}{1-\mu}c\right)x + b - \frac{\mu}{1-\mu}d\right] \tag{3.19}$$

To determine the explicit formulae for *u* and *v*, the following boundary conditions are considered:

$$u|_{x=0} = 0 \tag{3.20}$$

$$v|_{y=0} = 0 \tag{3.21}$$

As a result, the aggregate horizontal and vertical displacement components can be expressed as follows:

$$u = \frac{1-\mu^2}{E}\left(c - \frac{\mu}{1-\mu}a\right)\frac{x^2}{2} + \frac{1-\mu^2}{E}\left(d - \frac{\mu}{1-\mu}b\right)x \tag{3.22}$$

$$v = \frac{1-\mu^2}{E}\left(a - \frac{\mu}{1-\mu}c\right)xy + \frac{1-\mu^2}{E}\left(b - \frac{\mu}{1-\mu}d\right)y \tag{3.23}$$

The horizontal displacement *u* is a second-order function of the *x* coordinate, while the vertical displacement *v*, is a function of both *x* and *y* coordinates, changes linearly with *x* at a certain depth *y*. With *u* and *v* known, the shear strain can be obtained using Equation (3.5), as follows:

$$\gamma_{xy} = \frac{1-\mu^2}{E}\left(a - \frac{\mu}{1-\mu}c\right)y \tag{3.24}$$

Eventually, the shear stress can be calculated using Equation (3.8), yielding the following equation:

$$\tau_{xy} = \frac{1-\mu}{2}\left(a - \frac{\mu}{1-\mu}c\right)y \tag{3.25}$$

The shear stress obtained above (τ_{xy}), is used later in this section to estimate the soil-geosynthetic interface friction. However, as discussed in detail later, the shear stress on the geosynthetic surface predicted from Equation (3.25) is expected to be particularly small due to the elastic solution. A more realistic soil-geosynthetic interface shear was eventually adopted considering the contribution of the interlocking between the aggregate and geogrid together with the skin friction at the interface.

3.3.3 Quantification of the Geosynthetic Influence

3.3.3.1 Formulation of the SGC Model

The influence of the geosynthetic in the stabilized base course was quantified by incorporating the soil-geosynthetic composite (SGC) model (Roodi 2016; Zornberg et al. 2017) into the preceding analytical framework. The soil-geosynthetic composite (SGC) model was developed by researchers at The University of Texas at Austin to characterize the soil-geosynthetic interaction under small displacements (serviceability conditions). This model solves well-established force equilibrium differential equations by adopting specific constitutive relationships and boundary conditions that resulted a closed-from solution. Specifically, the model introduced a single parameter, referred to as the stiffness of the soil-geosynthetic composite, or K_{SGC}, which captures both the tensile stiffness of the geosynthetic and the shear behavior of the soil-geosynthetic interface (Roodi 2016; Zornberg et al. 2017).

The soil-geosynthetic composite (SGC) model involves two constitutive relationships, which apply to the geosynthetic itself and the soil-geosynthetic interface, respectively. Concerning confined geosynthetic stiffness, the following equation was adopted to relate geosynthetic unit tension to its tensile strain:

$$T = J_c \cdot \varepsilon_g \tag{3.26}$$

where $T =$ the geosynthetic unit tension (kN/m), which is the applied force per unit width of the geosynthetic, $J_c =$ the confined geosynthetic stiffness (kN/m), and $\varepsilon_g =$ the geosynthetic tensile strain. Such a linear relationship between *T* and ε_g is illustrated in Figure 3.5(a). It should be noted that J_c is not the same as the geosynthetic elastic modulus. Instead, they are related based on the following equation:

$$J_c = E_g \cdot (2t_{gs}) \tag{3.27}$$

where $E_g =$ the geosynthetic elastic modulus (kPa) and $t_{gs} =$ the half thickness of the geosynthetic (m). In this study, J_c instead of E_g was adopted to evaluate the tensile characteristics of the geosynthetic.

On the other hand, the constitutive relationship for the soil-geosynthetic interface relates the interface shear stress to the relative displacement between the base aggregates and the geosynthetic. Specifically, the interface shear stress was assumed not to change with displacement, meaning a rigid-perfectly plastic response, which is illustrated in Figure 3.5(b). A yield interface shear stress, denoted by τ_y, develops for nonzero displacements as follows:

$$\tau(u) = 0 \qquad \text{for } u = 0 \tag{3.28a}$$

$$\tau(u) = \tau_y \qquad \text{for } u > 0 \tag{3.28b}$$

These two constitutive relationships simplified the solving process and ultimately resulted in a closed-form analytical solution. Detailed explanation will be provided in the following section.

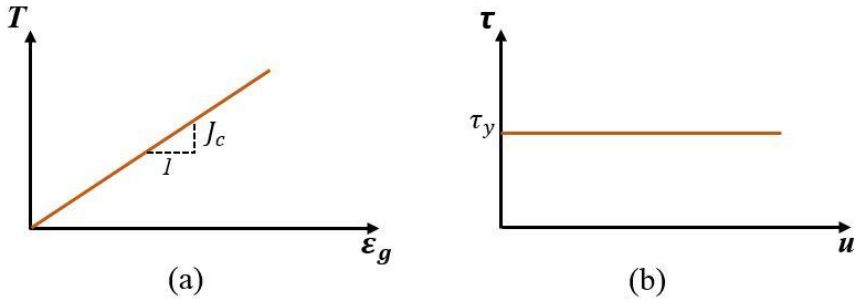

Figure 3.5: Constitutive relationships adopted in the SGC model: (a) geosynthetic unit tension-tensile strain relationship; (b) soil-geosynthetic interface shear

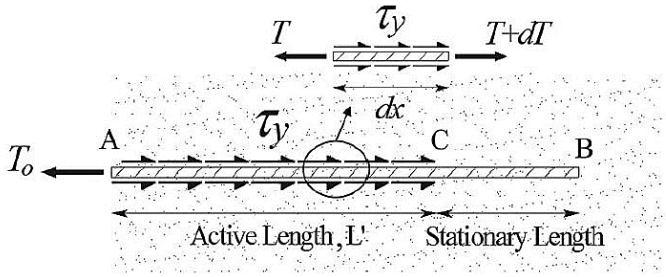

Figure 3.6: Force equilibrium in the SGC model (Zornberg et al., 2017)

Based on the force equilibrium of a differential segment of the confined geosynthetic as shown in Figure 3.6, the governing differential equation for the soil-geosynthetic interaction can be expressed as follows:

$$\frac{dT}{dx} = -2\tau_y \tag{3.29}$$

where $dx =$ the length of a differential segment of the geosynthetic, $T =$ the geosynthetic unit tension, and $\tau_y =$ the yield shear stress at the soil-geosynthetic interface. It should be noted that the left end (point A) of the geosynthetic in Figure 3.6 is the front of the pullout loading. Accordingly, in Equation (3.29), dT is negative since the unit tension decreases towards the stationary end, while dx and τ_y are positive values

representing the magnitude of segment length and shear stress respectively. Equation (3.29) indicates that T is a linear function of x with a slope of $-2\tau_y$, as shown by the following equation:

$$T(x) = -2\tau_y x + C \tag{3.30}$$

where $C =$ a constant needed to be determined based on the boundary condition. It is recognized in the SGC model that the interface shear is mobilized only along a portion of the geosynthetic length under a given confining pressure and for a given applied tension (Zornberg et al., 2017). The mobilized length is called the active length of the geosynthetic, which is denoted by L'. At $x = L'$, as shown by point C in Figure 3.6, the geosynthetic unit tension is considered to be zero. Consequently, the constant C in Equation (3.30) can be decided using Equation (3.31), and T can be subsequently expressed using Equation (3.32).

$$C = T_0 = 2\tau_y L' \tag{3.31}$$

$$T(x) = 2\tau_y (L' - x) \tag{3.32}$$

where T_0 is the geosynthetic unit tension at $x = 0$. Substitution of Equation (3.32) into Equation (3.26) results in the following expression of the geosynthetic tensile strain:

$$\varepsilon_g(x) = 2\frac{\tau_y}{J_c}(L' - x) \tag{3.33}$$

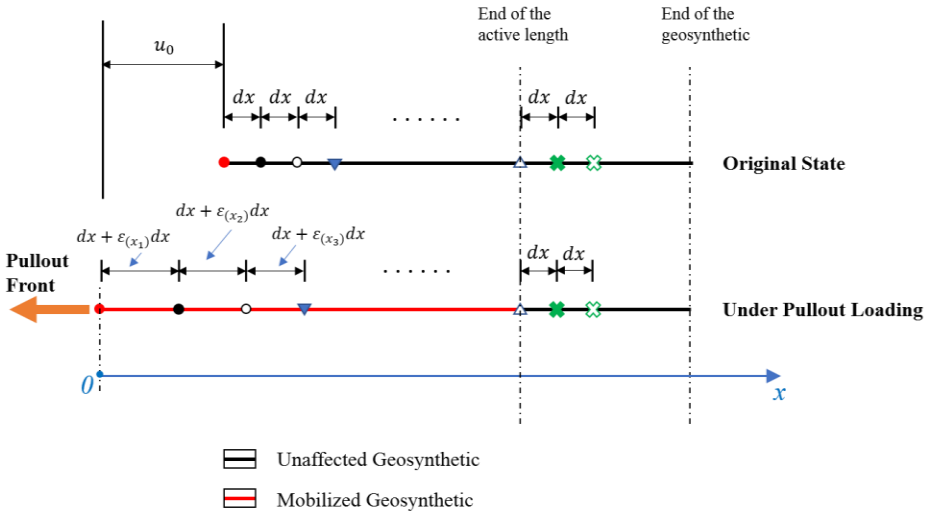

(a)

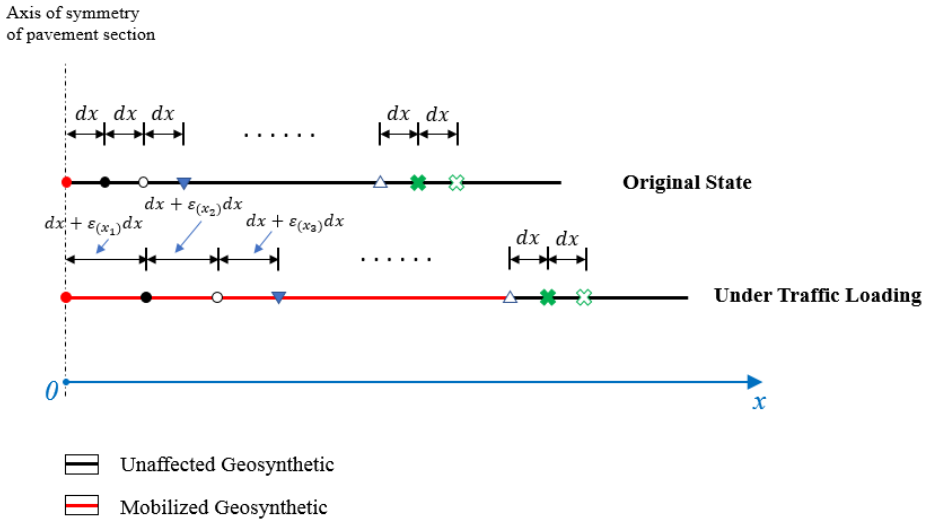

(b)

Figure 3.7: Different loading mechanisms and the corresponding geosynthetic deformation modes: (a) under pullout loading; (b) under traffic loading

The SGC model was developed based on the pullout loading mechanism. As shown in Figure 3.7(a), in such a coordinate system where the pullout front is the origin of the x axis, the geosynthetic unit tension and tensile strain can be represented by Equations (3.32)

and (3.33) according to the preceding analysis. Using the point marked by the blue triangle as an example, its displacement can be calculated using the following equation:

$$u_g(x_3) = u_{g0} + 3dx - \left[3dx + \sum_{i=1}^{3} \varepsilon_{(x_i)} dx\right] = u_{g0} - \sum_{i=1}^{3} \varepsilon_{(x_i)} dx \tag{3.34}$$

where $u_{g0} =$ the geosynthetic displacement at the pullout front. In a generalized form, the geosynthetic displacement at a certain point *x* can be obtained from the integral as follows:

$$u_g(x) = u_{g0} - \int_0^x \varepsilon_{(x)} dx \tag{3.35}$$

Subsequently, substitution of Equation (3.33) into Equation (3.35) yields the explicit expression of the geosynthetic displacement under pullout loading as follows:

$$u_g(x) = u_{g0} - \frac{2\tau_y}{J_c}\left(L'x - \frac{x^2}{2}\right) \tag{3.36}$$

To determine the unknown u_{g0} in Equation (3.36), the following boundary condition is adopted:

$$u_g(x = L') = 0 \tag{3.37}$$

As a result, u_{g0} is decided to be the value shown in Equation (3.38), and Equation (3.39) is the final expression of the geosynthetic displacement:

$$u_{g0} = \frac{\tau_y}{J_c} L'^2 \tag{3.38}$$

$$u_g(x) = \frac{\tau_y}{J_c}(x - L')^2 \tag{3.39}$$

The geosynthetic unit tension, tensile strain and displacement predicted using the SGC model are illustrated in Figure 3.8. It is noticed that the geosynthetic unit tension and tensile strain decrease linearly towards the end of the active length, while the geosynthetic displacement distribution is a convex curve. As discussed next, due to the difference in the loading mechanism and the boundary conditions, distribution of geosynthetic

displacements in the pavement cases subjected to traffic loading is different from that under the pullout loading.

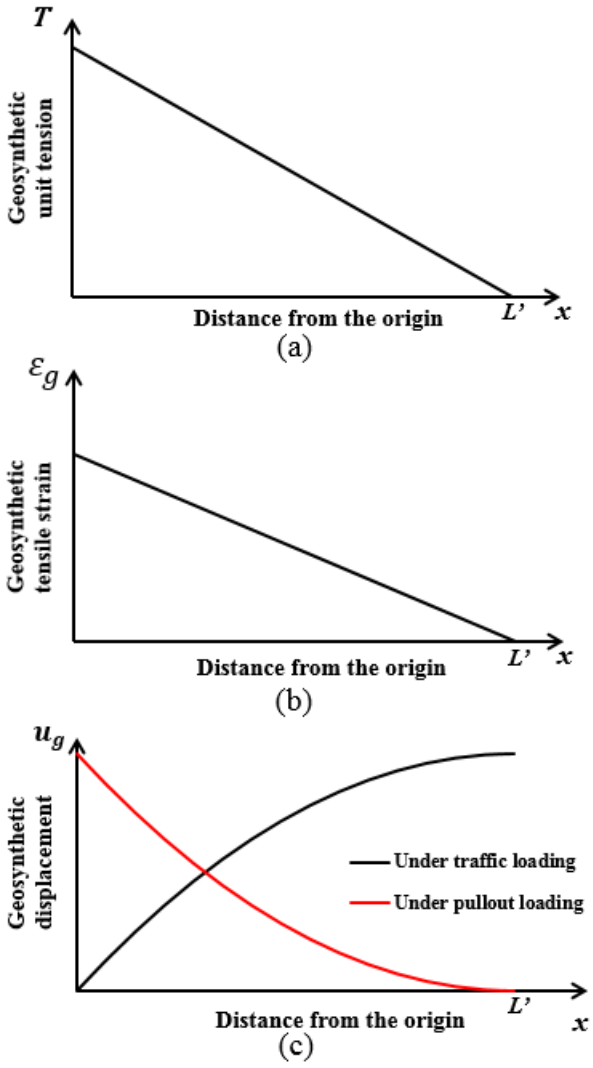

Figure 3.8: Distribution of the important parameters in the SGC model and the proposed analytical model: (a) geosynthetic unit tension; (b) geosynthetic tensile strain; (c) geosynthetic displacement

3.3.3.2 Adaptation of the SGC Model to the Traffic Loading Condition

Figure 3.7(b) illustrates the deformation pattern of the geosynthetic under the traffic loading condition. In this diagram, only the geosynthetic section that is located on one side of the vertical loading axis is shown, starting from the loading axis at x=0. This point is considered to be the middle point of the geosynthetic because the geosynthetic is expected to extend symmetrically on the other side of the loading axis. Although the geosynthetic unit tension and tensile strain still have their largest values in the middle of the geosynthetic (i.e., at x=0) and decrease linearly towards the positive *x* direction, the geosynthetic displacement is expected to be zero at this point and increase cumulatively towards the end of its active length. Selected again as an example, the displacement of the point marked by the blue triangle can be calculated for the vehicle loading condition as follows:

$$u_{g(x_3)} = 3dx + \sum_{i=1}^{3} \varepsilon_{(x_i)} dx - 3dx = \sum_{i=1}^{3} \varepsilon_{(x_i)} dx \tag{3.40}$$

In a generalized form, the geosynthetic displacement at a certain point *x* can be obtained from the integral as follows:

$$u_{g(x)} = \int_0^x \varepsilon_{(x)} dx \tag{3.41}$$

Subsequently, substitution of Equation (3.33) into Equation (3.41) results in the explicit expression of the geosynthetic displacement under the realistic vehicle loading as follows:

$$u_{g(x)} = \frac{-\tau_y}{J_c} [(x - L')^2 - L'^2] \tag{3.42}$$

Such a geosynthetic displacement distribution is illustrated by the black concave curve in Figure 3.8(c). It increases along the *x* axis due to the accumulation of displacements as indicated by the integral in Equation (3.41). The geosynthetic length

which is mobilized, however, is still limited since the tensile strain drops to zero at a certain point.

3.3.3.3 Determination of the Additional Confining Stress

As previously discussed, an additional confining stress was adopted in Case 2 to represent the effect of the geosynthetic stabilization on the base course. Under the traffic loading, the aggregate in the base course tends to move laterally, and the soil-geosynthetic interaction causes the geosynthetic to be stretched with the aggregate movement. Due to comparatively high geosynthetic tensile stiffness, the amount of extension is very limited, but considerable tension is expected to be developed in the geosynthetic. Inversely, this tension applies additional confinement to the aggregates, which can be considered as an equivalent compressive stress of the same magnitude as the tension applied at the location of the geosynthetic inclusion. Assuming a uniform compressive stress within the geosynthetic influence zone, the additional confining stress ($\Delta\sigma_3$) can be defined as:

$$\Delta\sigma_3 = \alpha \cdot \frac{T_{avg}}{2t} = \alpha \cdot \frac{T_0}{4t} \tag{3.43}$$

where $t =$ the half of the thickness (m) of the geosynthetic influence zone, $T_{avg} =$ the average geosynthetic unit tension (kN/m), $T_0 =$ the geosynthetic unit tension (kN/m) at $x = 0$. In this analytical model, $\Delta\sigma_3$ is assumed to be a constant value within the active length of the geosynthetic. The geosynthetic unit tension (T), however, decreases linearly with the increasing x within this range. Accordingly, the average unit tension was used to estimate $\Delta\sigma_3$. The coefficient α is a correction factor that increase the confinement pressure to take the contribution from the bearing resistance into account. As previously explained, additional confinement provided by the bearing resistance from geogrid transverse ribs cannot be effectively quantified in the elastic theory. Determination of α is explained in detail in Appendix C.

The value of $T_{(x=0)}$ can be estimated using Equation (3.31). However, the geosynthetic active length *L'* is unknown in this expression. In pullout tests, the location of the telltale which is first triggered under a certain frontal pullout force corresponds to the geosynthetic active length at that moment. Thus, *L'* can only be easily determined through experiments. Nevertheless, it is required in this analytical model to obtain *L'* mathematically, as a critical step in the incorporation of the SGC model into the framework of the theory of elasticity. The approach used to fulfil this goal is discussed in detail next.

Substitution of $x = L'$ into Equation (3.22) yields the following expression for the aggregate displacement at $x = L'$:

$$u_{sL'} = \frac{1-\mu^2}{E}\left(c - \frac{\mu}{1-\mu}a\right)\frac{L'^2}{2} + \frac{1-\mu^2}{E}\left(d - \frac{\mu}{1-\mu}b\right)L' \tag{3.44}$$

where constant *a* is determined using Equation (3.15), while constants *b* and *c* are obtained according to Appendixes A and B, respectively. For Case 1 and Case 3, constant *d* can be obtained as explained in Appendix A. Constant *d* in Case 2, however, is different since an additional confining stress is considered. To distinguish constant *d* in Case 2 from those in the other two cases, a new parameter *d'* was adopted, which is defined as follows:

$$d' = d - \Delta\sigma_3 \tag{3.45}$$

where *d* remains the same as that calculated in Appendix A, and $\Delta\sigma_3$ is a positive value representing the magnitude of the additional confining stress resulted from the geosynthetic.

Since a rigid-perfectly plastic response was assumed for the constitutive relationship at the soil-geosynthetic interface, the interface shear develops where relative displacement exists between the aggregates and geosynthetic. Accordingly, the aggregates and geosynthetic are expected to have the same displacement at $x = L'$, because the

geosynthetic has not been mobilized beyond that point, indicating no interface shear and thus no relative displacement. In short, the following equation is considered:

$$u_{sL'} = u_{gL'} \tag{3.46}$$

where $u_{sL'} =$ the aggregate displacement at $x = L'$ in Case 2, while $u_{gL'} =$ the geosynthetic displacement at $x = L'$ in Case 2. In addition, according to Equation (3.42), $u_{gL'}$ can be expressed as follows:

$$u_{gL'} = \frac{\tau_y}{J_c} L'^2 \tag{3.47}$$

Considering Equations (3.44), (3.46) and (3.47) and replacing *d* in Equation (3.44) by *d'* obtained from Equation (3.45) yield the following equation for Case 2:

$$\frac{\tau_y}{J_c} L'^2 = \frac{1-\mu^2}{E_u}\left(c - \frac{\mu}{1-\mu} a\right)\frac{L'^2}{2} + \frac{1-\mu^2}{E_u}\left(d - \Delta\sigma_3 - \frac{\mu}{1-\mu} b\right) L' \tag{3.48}$$

Furthermore, $\Delta\sigma_3$ is also a function of *L'*. Using Equation (3.31), T_0 can be replaced in Equation (3.43) as follows:

$$\Delta\sigma_3 = \alpha \cdot \frac{\tau_y L'}{2t} \tag{3.49}$$

Subsequently, replacing $\Delta\sigma_3$ in Equation (3.48) with Equation (3.49) results in the following equation:

$$\frac{\tau_y}{J_c} L'^2 = \frac{1-\mu^2}{E_u}\left(c - \frac{\mu}{1-\mu} a\right)\frac{L'^2}{2} + \frac{1-\mu^2}{E_u}\left(d - \alpha\frac{\tau_y L'}{2t} - \frac{\mu}{1-\mu} b\right) L' \tag{3.50}$$

Solving Equation (3.50) for L', the active length of the geosynthetic can be expressed as follows:

$$L' = \frac{\frac{1-\mu^2}{E_u}(d - \frac{\mu}{1-\mu} b)\frac{J_c}{\tau_y}}{1 - \frac{1-\mu^2}{E_u}\frac{J_c}{2}\left[\left(c - \frac{\mu}{1-\mu} a\right)\frac{1}{\tau_y} - \frac{\alpha}{t}\right]} \tag{3.51}$$

where $E_u =$ the original elastic modulus of the base material, $\mu =$ the Poisson's ratio of the base material, $J_c =$ the confined geosynthetic stiffness, $\tau_y =$ the yield shear stress at

the soil-geosynthetic interface, *a*, *b*, *c* and *d* are the constants in the assumptions of vertical and horizontal stresses, $\alpha =$ the correction factor, and *t* is the half of the thickness of the geosynthetic influence zone. With *L'* obtained in Equation (3.51), the additional confining stress caused by the geosynthetic can be determined by plugging *L'* into Equation (3.49), as follows:

$$\Delta\sigma_3 = \frac{\frac{1-\mu^2}{E_u}\left(d-\frac{\mu}{1-\mu}b\right)\frac{\alpha J_c}{2t}}{1-\frac{1-\mu^2 J_c}{E_u \ 2}\left[\left(c-\frac{\mu}{1-\mu}a\right)\frac{1}{\tau_y}-\frac{\alpha}{t}\right]} \tag{3.52}$$

3.3.3.4 Determination of the Increased Elastic Modulus

The geosynthetic stabilization effect on the base course was quantified by $\Delta\sigma_3$ as expressed in Equation (3.52). Nevertheless, to facilitate incorporation of geosynthetic effect into a mechanistic-empirical pavement design, probably a more desirable approach is to obtain an improved property for the base material such as an increased elastic modulus. Specific benefit of an improved material property for the base course is that the improved property can directly be used as an input into an existing pavement critical response model (e.g., WinJULEA) to calculate the resilient strain and further evaluate the rutting and cracking with empirical equations.

In this study, the increased elastic modulus (E_r) was estimated based on the equivalence between Case 2 and Case3. Specifically, the selected E_r is the elastic modulus that ensures the same aggregate horizontal displacement at $x = L'$ in Case 2 and Case 3, as indicated by the following equation:

$$u_{2s}(x = L') = u_{3s}(x = L') \tag{3.53}$$

where $u_{2s}(x = L') =$ the aggregate horizontal displacement at $x = L'$ in Case 2, while $u_{3s}(x = L')$ is its counterpart in Case 3.

As introduced earlier, the geosynthetic influence is represented by the additional confining stress and the increased elastic modulus respectively in Case 2 and Case 3. E_u and *d'* were the parameters adopted in Case 2, while E_r and *d* were the parameters adopted in Case 3. Substitution of these parameters into Equation (3.44) yields the following expressions for the horizontal aggregate displacements at $x = L'$ in Case 2 and Case 3:

$$u_{2s}(x = L') = \frac{1-\mu^2}{E_u}\left(c - \frac{\mu}{1-\mu}a\right)\frac{L'^2}{2} + \frac{1-\mu^2}{E_u}\left(d' - \frac{\mu}{1-\mu}b\right)L' \tag{3.54}$$

$$u_{3s}(x = L') = \frac{1-\mu^2}{E_r}\left(c - \frac{\mu}{1-\mu}a\right)\frac{L'^2}{2} + \frac{1-\mu^2}{E_r}\left(d - \frac{\mu}{1-\mu}b\right)L' \tag{3.55}$$

where $E_u =$ the original elastic modulus of the base material without geosynthetics; $E_r =$ the increased elastic modulus of the geosynthetic-stabilized base material; $\mu =$ the Poisson's ratio of the base material; *a*, *b*, *c* and *d* are the constants in the stress assumptions; and $d' =$ the surrogate for *d* in Case 2, as defined in Equation (3.45).

Substitution of Equations (3.54) and (3.55) into Equation (3.53) yields the following expression of E_r:

$$E_r = \frac{\left(c-\frac{\mu}{1-\mu}a\right)\frac{L'}{2}+\left(d-\frac{\mu}{1-\mu}b\right)}{\left(c-\frac{\mu}{1-\mu}a\right)\frac{L'}{2}+\left(d'-\frac{\mu}{1-\mu}b\right)} \cdot E_u \tag{3.56}$$

where L' can be expressed using Equation (3.51), and d' can be expressed according to Equations (3.45) and (3.52). By replacing L' and d' in Equation (3.56) with their explicit expressions and simplifying the resultant equation, the increased elastic modulus E_r can be ultimately expressed as follows:

$$E_r = E_u + \frac{\alpha(1-\mu^2)J_c}{2t} \tag{3.57}$$

where E_u, E_r and μ have the same meaning as in Equations (3.54) and (3.55). α is the correction factor as defined in Appendix C, J_c is the confined geosynthetic tensile stiffness (kN/m), and *t* is the half of the thickness of the geosynthetic influence zone.

It is worth mentioning that an alternative way to represent the equivalence between Case 2 and Case 3 is the minimum integral of the squared difference between the horizontal aggregate displacements in these two cases. This integral is calculated within the active length of the geosynthetic. Although this minimum integral is a more rigorous way to compare the horizontal displacements between the two cases, a simpler criterion as indicated in Equation (3.53) is finally adopted. As shown in Equation (3.46), the zero aggregate-geosynthetic relative displacement at $\mathrm{x} = L'$ in Case 2 was a critical assumption used to derive L' and $\Delta\sigma_3$. Since Case 3 is also a geosynthetic-stabilized case, the horizontal aggregate displacement at $\mathrm{x} = L'$ in Case 3 should also equal the geosynthetic displacement at $\mathrm{x} = L'$. Accordingly, $u_{3s(x=L')}$ should equal $u_{2s(x=L')}$ so that the horizontal displacement curves of the aggregates in Case 2 and Case 3 and the geosynthetic all intersect at one common point when $\mathrm{x} = L'$. Therefore, Equation (3.53) is followed to meet this requirement. In this way, the integrated squared difference between the horizontal aggregate displacements in the two cases was increased to some degree. However, this increase was slight and thus still acceptable.

The difference in horizontal displacements, instead of vertical displacements, was adopted because the horizontal displacements are more relevant to the lateral restraint mechanism, which is expected to be predominant mechanism is geosynthetic-stabilization of base course. In addition, the linear functions were adopted in the assumptions for the normal stress conditions to ensure that the resultant aggregate horizontal displacement has a function form similar to that of the geosynthetic displacement formulated in the SGC model. As shown in Equations (3.22), (3.23), and (3.42), the horizontal displacements of the aggregate and the geosynthetic are both second-order functions of *x*, while the aggregate vertical displacement is a linear function of *x* at a certain *y*. The similar form of the two horizontal displacement functions offered significant benefits in evaluating the

relative displacement between the aggregate and the geosynthetic, determining the geosynthetic active length, and quantifying the additional confining stress. Nonetheless, the adopted stress assumptions, customized for the horizontal displacement, may have compromised the vertical displacement predictions. Consequently, although the vertical displacement may directly be related to the rutting predictions, the horizontal displacement was used to evaluate the equivalence between Case 2 and Case 3.

3.3.4 Model Results

A summary of the main predictions by the proposed analytical model is presented in Figures 3.9 to 3.12 using schematic diagrams. Specifically, in Figure 3.9, the geosynthetic influence zone was extracted from the pavement profile in Case 2. This zone is included in Figures 3.10 to 3.12 to help illustrate the distribution of those parameters. Figure 3.10 presents the distribution of geosynthetic unit tension and tensile strain, Figure 3.11 presents the distribution of the aggregate and geosynthetic horizontal displacements, and Figure 3.12 presents the distribution of the aggregate vertical displacements. By analyzing these results, the following concluding remarks can be made:

- The geosynthetic was only mobilized within part of the vertical stress distribution zone.
- Linear geosynthetic unit tension and tensile strain are developed in the mobilized length of the geosynthetic, while the geosynthetic displacement is a second-order function.
- The three concave curves in Figure 3.11 correspond to the aggregate horizontal displacements in the three pavement cases. Aggregate horizontal displacements in Cases 2 and 3 are expected to be very close within the geosynthetic active length, and their curves intersect at the end of the active length (i.e., $x = L'$).

- The aggregate horizontal displacements in Case 2 and Case 3 are smaller than that of Case 1. This is how the geosynthetic influence is reflected in the comparison of horizontal displacements.
- The geosynthetic displacement was predicted to be smaller than the aggregate displacements. The relative displacement between the aggregate and geosynthetic along the active length of the geosynthetic indicated that the geosynthetic was not fully bonded to the moving aggregate particles.
- In the proposed model, the vertical aggregate displacement has a linear distribution along the *x* axis at any given depth *y*.
- As previously discussed, the adopted stress assumptions, customized for the horizontal displacement, compromised the vertical displacement predictions to some degree. Consequently, the aggregate vertical displacements in Cases 2 and 3 did not show significant reduction compared to that in Case 1.

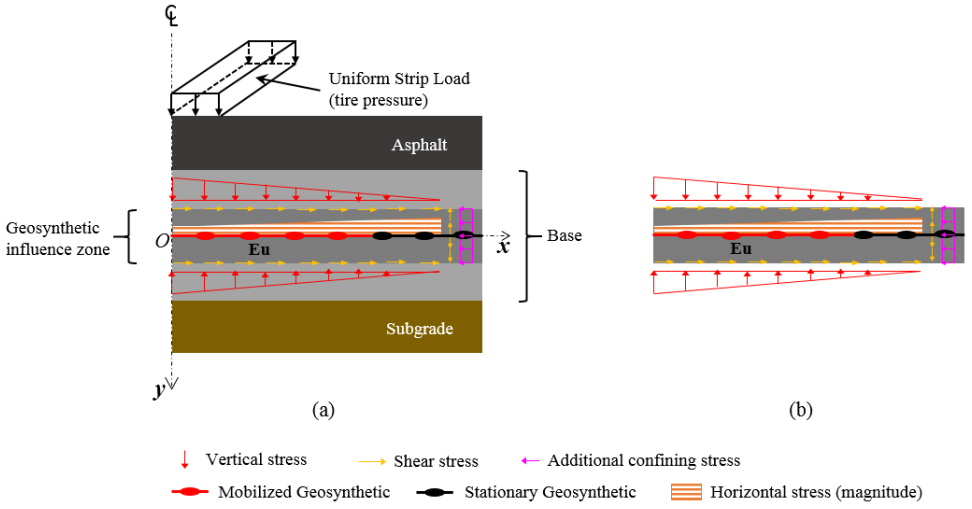

Figure 3.9: Details of the pavement section in Case 2: (a) pavement geometry, traffic loading condition and stress distribution; (b) object of interest in the proposed model: geosynthetic influence zone

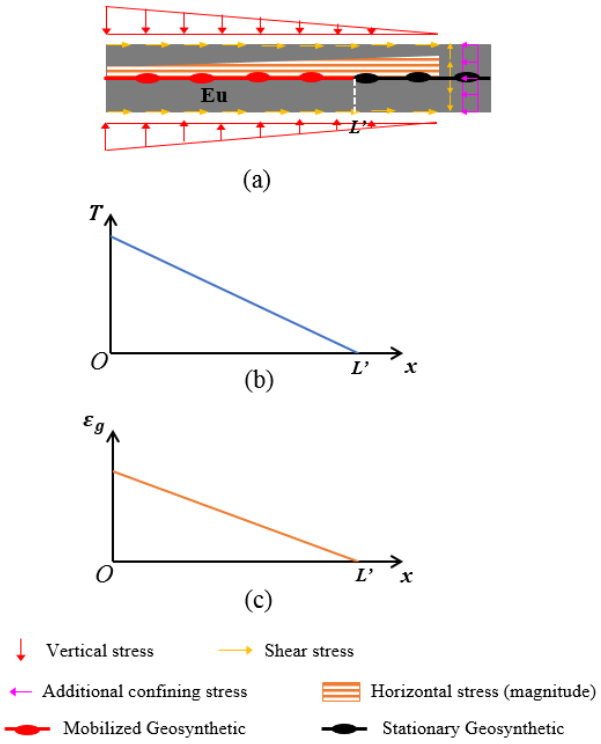

Figure 3.10: Diagrams of the results of the proposed model: (a) object of interest in the proposed model: geosynthetic influence zone; (b) distribution of geosynthetic unit tension; (c) distribution of geosynthetic tensile strain

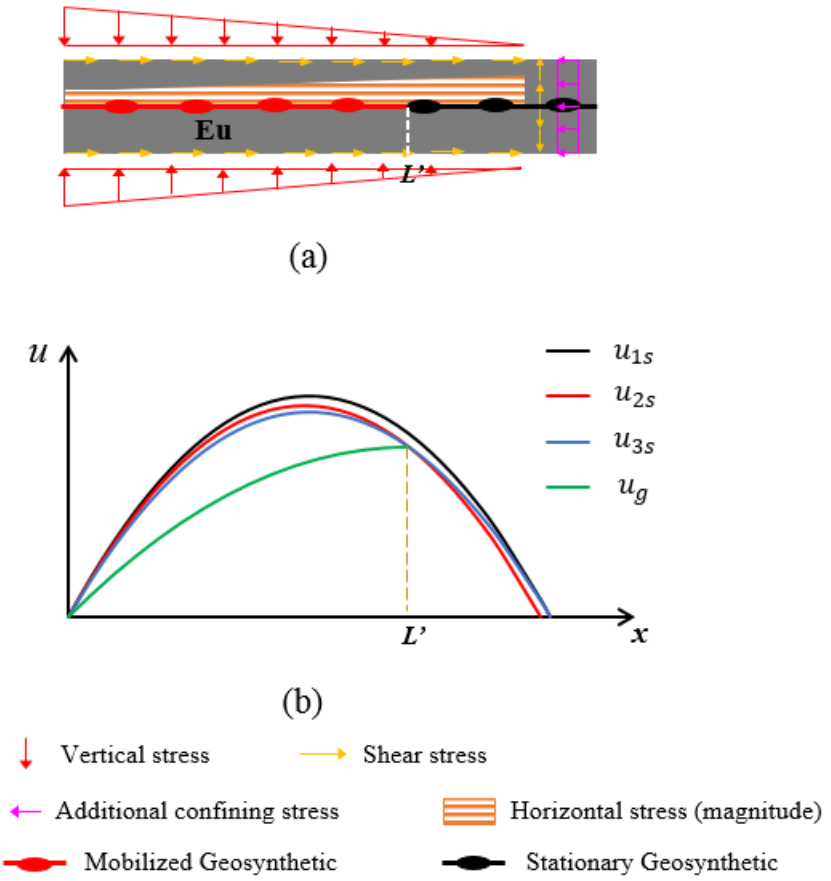

Figure 3.11: Diagrams of the results of the proposed model: (a) object of interest in the proposed model: geosynthetic influence zone; (b) distribution of horizontal displacements of the aggregate and geosynthetic

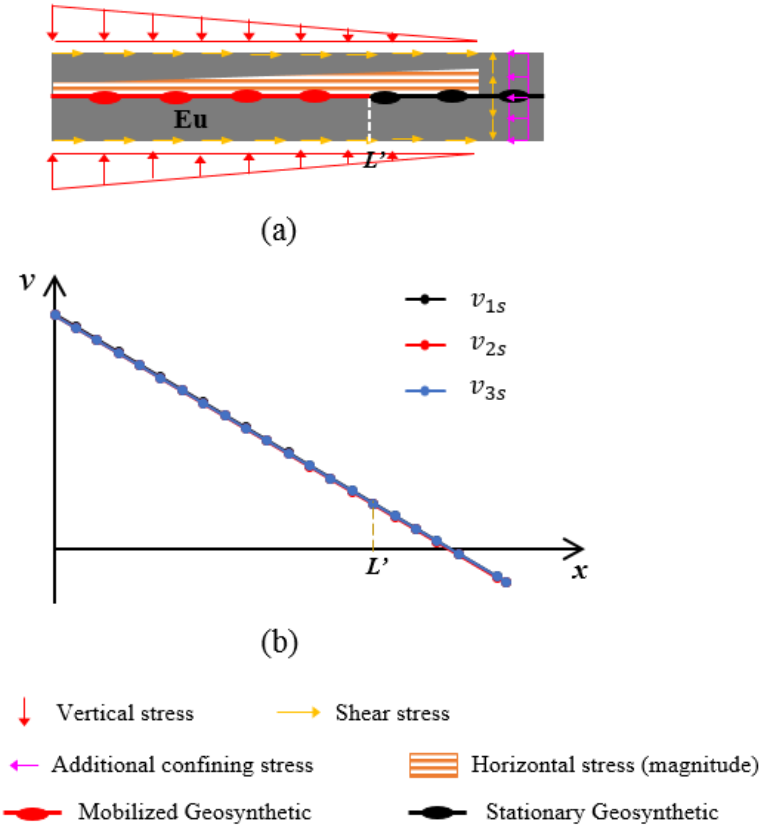

Figure 3.12: Diagrams of the results of the proposed model: (a) object of interest in the proposed model: geosynthetic influence zone; (b) distribution of aggregate vertical displacements

The increased elastic modulus (E_r) obtained using the developed analytical model can be used as the mechanical property for the geosynthetic-stabilized sublayers of the base course in pavement response software (e.g., WinJULEA) to predict the resilient strains and further evaluate the development of pavement distress using empirical equations. The total thickness of the geosynthetic-stabilized sublayers can be estimated using suggested values for geosynthetic influence zone. Using specific model inputs, validation and sensitivity analysis are performed for this model in the following chapters.

Chapter 4: Validation of the Analytical Model

4.1 OVERVIEW

The primary results of the analytical model proposed in this study are the additional confining stress $\Delta\sigma_3$ and the improved elastic modulus of the geosynthetic-stabilized base course. Elastic modulus is produced from this analytical model since its derivation is based on the theory of elasticity. However, resilient modulus instead of elastic modulus has typically been adopted by pavement designers, since elastic modulus, defined as the slope of the stress-strain curve in the elastic region (Askeland and Phulé, 2003), may not be fully consistent with the conditions of the unbound pavement materials which develop considerable plastic deformation under repeated traffic loads. Despite this difference, the resilient modulus can be an indicator of the material's elastic property, and thus, has been usually considered as an estimate of its elastic modulus (Olague et al., 2016). Therefore, considering that the majority of the experimental studies on geosynthetic-stabilized soil have reported resilient modulus rather than elastic modulus, it can be acceptable to compare the predicted elastic moduli from the proposed model with test results of resilient moduli for primary evaluation of the model.

In this section, triaxial test data from two published studies were used to validate the proposed analytical model. These two studies were selected because sufficient details were available in the original publications about the material properties, testing conditions and test results. One of these studies was conducted by Nazzal (2007), while the other was part of the NCHRP Project 01-50 completed by Luo et al. (2017). Since the test results of Nazzal (2007) were also utilized by Yang and Han (2012) to validate their analytical model for the resilient modulus of geosynthetic-stabilized unbound granular material, comparison

of predictions from the model proposed in this study with Yang & Han model was also made to serve as an additional evaluation.

4.2 VALIDATION USING NAZZAL'S (2007) STUDY

4.2.1 Overview of Resilient Modulus Tests by Nazzal (2007)

Nazzal (2007) conducted resilient modulus tests on unreinforced and geogrid-reinforced crushed limestone samples. As one type of the repeated loading triaxial (RLT) tests, resilient modulus tests were performed by Nazzal (2007) in accordance with AASHTO-T307 standard method to determine the resilient modulus of a base course material. The aggregate material used in the resilient modulus tests was referred to as Crushed Limestone I, whose properties are listed in Table 4.1. Five types of geogrids were utilized in reinforced samples, as summarized in Table 4.2. In addition, three different arrangements of geogrids were made in Nazzal's resilient modulus tests, by placing the geogrid at the middle, upper one third, or both the upper and lower one third (double) of the samples. Since the analytical model in this study was developed based on a symmetrical base course where the geosynthetic was placed at the mid-depth, the test results about the samples with the geogrid placed at the mid-height were mainly considered for comparison with the model predictions.

Table 4.1: Properties of Crushed Limestone I Used in Nazzal's (2007) Study

Material	Bulk Specific of gravity	apparent specific of gravity	OMC	γ_{max} (kN/m^3)	CBR	Mr (kPa) estimated from CBR	absorption (%)	AASHTO Classification	USCS Classification	
									Before compaction	After compaction
Crushed Limestone I	2.54	2.7	7	21.9	101	337,813	2.14	A-1-a	GW	GW-GM

Note: OMC: optimum moisture content obtained in Standard Proctor Test
γ_{max}: maximum unit weight obtained in Standard Proctor Test
CBR: California Bearing Ratio; M_r: resilient modulus

Table 4.2: Properties of Geogrids Used in Nazzal's (2007) Study

Product ID[a]	Type	Tensile stiffness (@ strain 2%)[b]		Aperture dimension		Flexural stiffness[c]	Rib thickness[d]	
		MD (kN/m)	CMD (kN/m)	MD (mm)	CMD (mm)	(g-cm)	MD (mm)	CMD (mm)
BX-1	I	250	380	33	33	250	0.76	0.76
BX-2	II	280	450	25	33	750	0.76	0.76
BX-3	III	380	510	33	33	250	1.27	1.27
BX-4	IV	410	650	25	33	750	1.27	1.27
BX-5	V	580	690	25	30.5	2000	1.78	1.78

a: BX-1 to BX-5 are products from Tensar Corporation. Specifically, as per the current nomenclature of Tensar, Bx-1 is BX-4100, BX-2 is BX-1100, BX-3 is BX 4200, BX-4 is BX 1200, and BX-5 is BX 1500.
b: Measured in accordance with ASTM standard method for determining tensile properties of geogrids ASTM D6637 (Tensar Earth Technologies Inc., 2003)
c: Measured in accordance with ASTM Standard Test Method for determining stiffness of non-woven fabrics using the cantilever test ASTM D-5732-95 (Tensar Earth Technologies Inc., 2003)
d: Obtained from the specifications of current Tensar geogrid products (Not provided in Nazzal's study)
MD: Machine direction CMD: Cross-machine direction

All test samples were 150 mm in diameter and 300 mm in height. The samples were first conditioned by applying 1,000 load cycles under a confining stress of 103.4 kPa and a deviatoric stress of 93.0 kPa. This step was followed by a sequence of loading with varying confining and deviatoric stresses. Each stress combination corresponded to 100 loading cycles. The haversine-shaped load pulse used in Nazzal's study had a 0.1 sec load duration and 0.9 sec rest period. With the resilient strain measured, the resilient modulus was calculated using Equation (2.12) for a specified confining and deviator stress combination, and a regression analysis was then performed to fit each test data to the generalized constitutive model in Equation (2.11).

In Nazzal's study, after the regression constants k_1, k_2, k_3 had been obtained for the unreinforced samples and the reinforced samples with specific geogrid types and locations, the generalized constitutive model presented in Equation (2.11) was used to calculate the resilient moduli of those samples at a confining stress of 21 kPa, and three deviatoric stresses of 80, 160 and 250 kPa. Resilient moduli at these three specified stress

states were compared between the unreinforced and reinforced samples to evaluate the influence of geogrids. The improvement ratios of resilient moduli, R_{Mr}, could then be calculated using the following equation:

$$R_{Mr} = \frac{M_r \text{ of the reinforced sample}}{M_r \text{ of the unreinforced sample}} \quad (4.1)$$

However, the calculated resilient moduli of unreinforced and reinforced samples at the above three stress states were provided in the original publication only in the form of line charts, without specific values for R_{Mr} reported. Consequently, in this study, the R_{Mr} values were generated by digitizing the line charts provided by Nazzal (2007).

4.2.2 Considerations in the Analytical Model for Comparison with Nazzal's Study

The geogrid influence was characterized in the analytical model by the improvement ratio of elastic modulus, R_E, as defined in the following equation:

$$R_E = \frac{E_r}{E_u} \quad (4.2)$$

where $E_r =$ the improved elastic modulus of the geosynthetic-stabilized base material, and $E_u =$ the original elastic modulus of the base material without geosynthetics. E_u was one of the inputs of the proposed analytical model, and it was estimated from California Bearing Ratio (CBR) of the crushed limestone I, using the following correlation (ARA, 2004):

$$M_r = 2555(CBR)^{0.64} \quad (4.3)$$

where $M_r =$ resilient modulus (psi), and it was considered as an estimate of elastic modulus (*Eu*). The *Eu* value was then expressed in kPa.

To predict *Er* and R_E using the proposed analytical model, additional model inputs concerning the pavement geometry, geogrid properties and traffic loading conditions were

specified using the resilient modulus tests information provided by Nazzal (2007). These aspects are discussed in detail in the following sections.

4.2.2.1 Model Inputs Regarding Pavement Geometry

The analytical model considered a base course under a plane strain condition. Due to the differences in the geometry of the analytical model and Nazzal's triaxial tests, geometric characteristics required for the analytical model were specified using the values listed in Table 4.3. The sample height in Nazzal's resilient modulus tests was 0.3 m, and the analysis in Nazzal's study assumed that the geosynthetic influence zone was the whole sample. Therefore, in the analytical model it was assumed that the geogrid influenced the entire base course. In other words, the thickness of the geogrid influence zone in the model was set equal to Nazzal's sample height. Hence, a good consistency in the geometry was ensured between the test sample and the pavement profile analyzed in the analytical model.

Table 4.3: Geometric Parameters Assumed in the Analytical Model to Compare with Nazzal's Study

Input parameter	Value
HMA thickness (m)	0.1524
Base course thickness (m)	0.3
Thickness of geosynthetic influence zone (m)	0.3

4.2.2.2 Model Inputs Regarding Geogrid Properties

The geometric characteristics of the geogrids, including the aperture sizes and rib thicknesses, were specified in the model according to Table 4.2. The values reported in Table 4.2, however, were not directly used to input geogrid tensile stiffness into the model. The stiffness values in Table 4.2 are in-isolation geogrid stiffnesses at 2% strain whereas the geogrid confined within the base course is usually subjected to smaller deformations, which correspond to a higher stiffness. Roodi (2016) estimated the confined stiffness of

the same geogrid product BX-2 under small displacements through pullout tests, and the average result was 650 kN/m. A correction factor was adopted to estimate the confined stiffness based on the in-isolation stiffness at 2% strain using the above information for BX-2:

Stiffness correction factor (for BX-2) =650/450 = 1.44

Since no additional stiffness data was available for other geogrid types, 1.44 was used to correct the stiffness values for all five types of geogrids. The resultant model inputs of the confined geogrid tensile stiffness are listed in Table 4.4.

Table 4.4: Confined Tensile Stiffness Assumed for Geogrids Used in Nazzal's Study

Geogrid Type	J_c (kN/m)
I	549
II	650
III	737
IV	939
V	997

4.2.2.3 Model Inputs Regarding Traffic Loading Conditions

The analytical model requires the inputs of traffic loading conditions so that the stress distribution can be determined based on the specified pavement geometry and the existing assumptions of stress forms. Since the traffic load was assumed to be a uniform strip load, the related model inputs included the width of strip load, i.e., the width of the wheel, and the strip load magnitude, i.e., the tire pressure. The wheel width was assumed to be 0.21 m, but the tire pressure was not directly specified. Instead, since the improvement in elastic modulus was evaluated for the aforementioned three stress states (i.e., confining stress $\sigma_3 = 21$ kPa, and total axial stresses $\sigma_1 = 101,\ 181,$ and 271 kPa), constants b and d in the stress assumptions were set as $-\sigma_1$ and $-\sigma_3$, respectively, and the tire

pressure was back-calculated from the magnitude of constant b (i.e., σ_1) using Equation (a.2) in Appendix A.

4.2.2.4 Assumptions Regarding Soil and Interface Shear Strengths and Soil Elastic Properties

The internal friction angle and Poisson's ratio of Crushed Limestone I were assumed to be 40° and 0.3, respectively, because information regarding these parameters was not provided by Nazzal (2007). The aggregate-geogrid interface friction angle was also assumed to be 40°.

4.2.3 Comparison between Model Predictions and Test Results of Nazzal's Study

The input data described above were used in the proposed analytical model to estimate E_r and the elastic modulus improvement ratio R_E. The predicted improvement ratios R_E were then compared with the resilient modulus improvement ratios (R_{Mr}) calculated using Nazzal's data. To more clearly communicate the comparison results, the improvement in modulus was further expressed as the percent increase of modulus (i.e., $(R_E - 1) \times 100\%$ and $\left(R_{M_r} - 1\right) \times 100\%$). The comparison was conducted separately for four geogrid types and three deviatoric stress levels, as shown in Figures (4.1) to (4.3). Geogrid type V was not included since the related results were missing in the original publication.

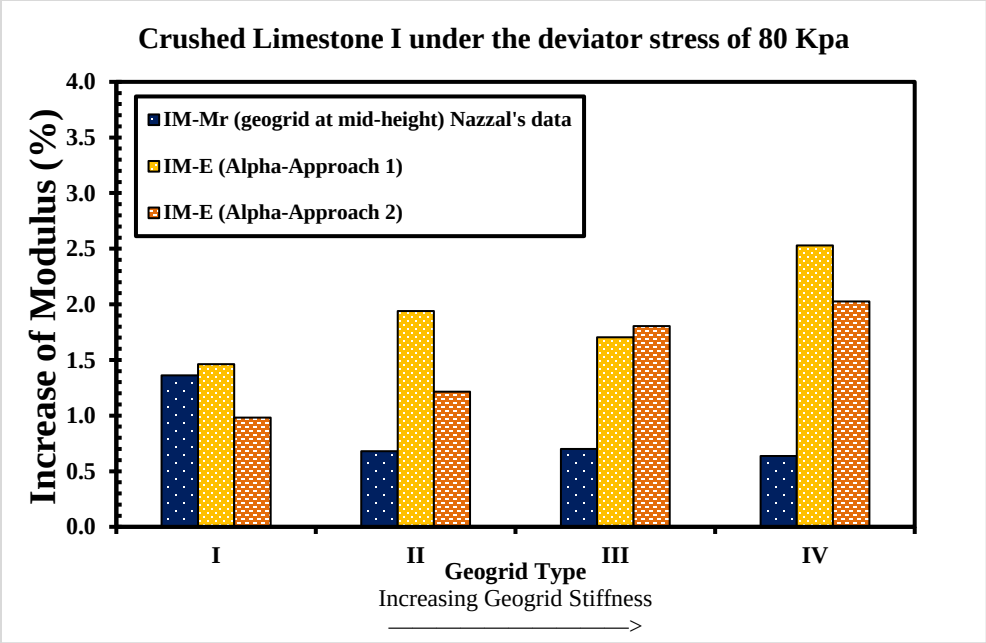

Figure 4.1: Comparison between $(R_{M_r} - 1) \times 100\%$ at deviatoric stress of 80 kPa in Nazzal's resilient modulus tests and $(R_E - 1) \times 100\%$ predicted using the analytical model

As indicated by the comparison results, the predicted percent increases of elastic modulus are close when determining the correction factor α using either of the two approaches proposed in Appendix C. This small difference indicates that the two approaches proposed to determine α are both effective, and they may be used as validation of one another.

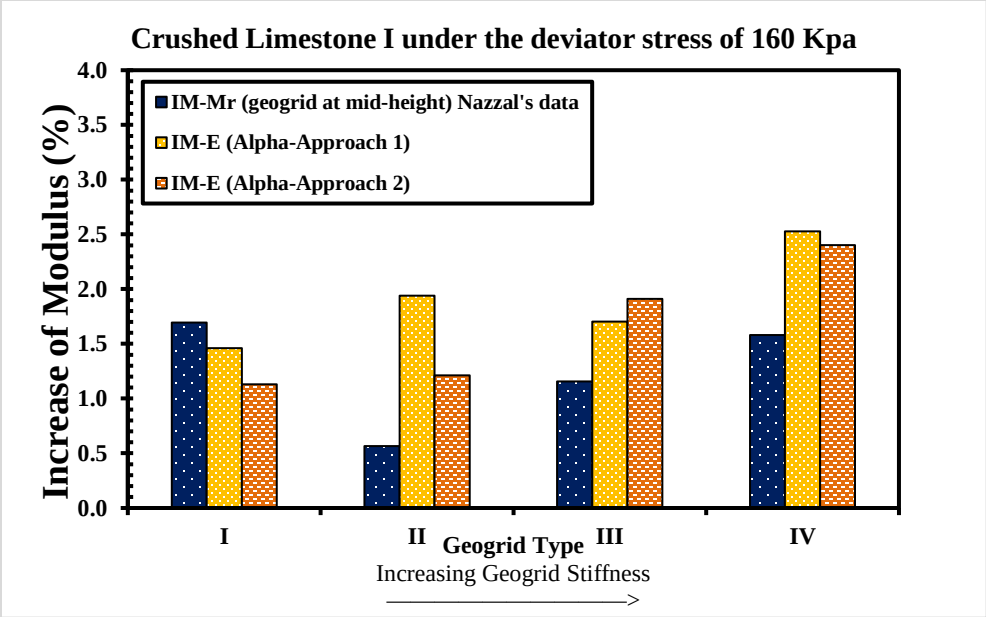

Figure 4.2: Comparison between $(R_{M_r} - 1) \times 100\%$ at deviatoric stress of 160 kPa in Nazzal's resilient modulus tests and $(R_E - 1) \times 100\%$ predicted using the analytical model

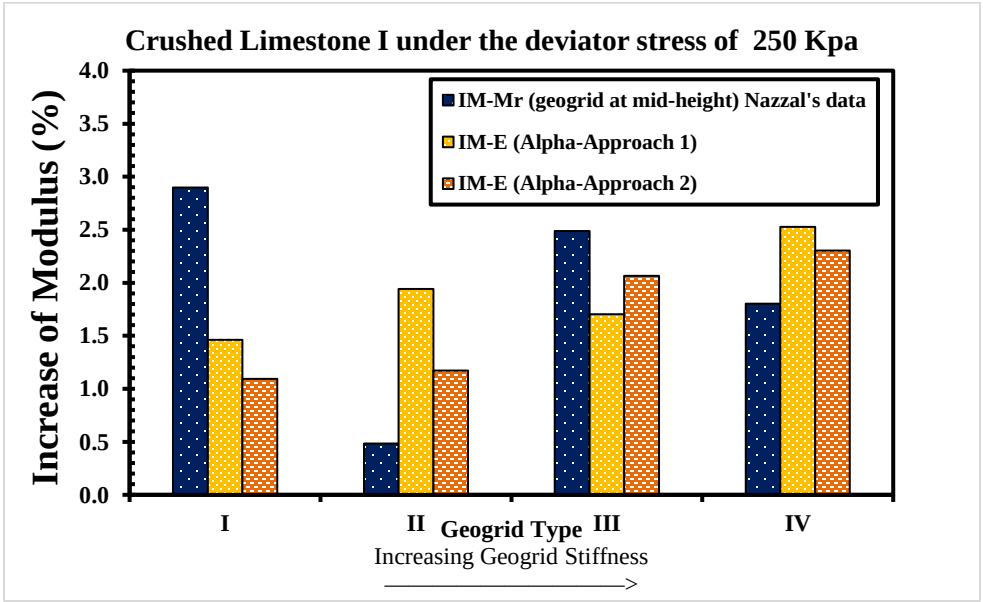

Figure 4.3: Comparison between $(R_{M_r} - 1) \times 100\%$ at deviatoric stress of 250 kPa in Nazzal's resilient modulus tests and $(R_E - 1) \times 100\%$ predicted using the analytical model

As shown in Figures 4.1 to 4.3, the percent increase of modulus ($(R_E - 1) \times 100\%$) predicted by this model are close to Nazzal's test results ($\left(R_{M_r} - 1\right) \times 100\%$). A reasonably good agreement can be observed in most groups of comparison, indicating the successful validation of the analytical model.

4.3 VALIDATION USING LUO ET AL. (2017) STUDY (NCHRP PROJECT 01-50)

4.3.1 Overview of Constitutive Models and Test Plans in Luo et al. (2017) Study

As part of the work done for NCHRP Project 01-50, Luo et al. (2017) conducted repeated loading triaxial tests to evaluate the cross-anisotropic properties of geogrid-reinforced unbound granular materials. By taking into account the cross-anisotropy, Luo et al. distinguished the resilient modulus in the vertical direction from that in the horizontal direction. In addition, two different Poisson's ratios were considered for the vertical and horizontal planes. The constitutive model in Equation (4.4) was adopted by Luo et al. to characterize the cross-anisotropic behavior.

$$\begin{bmatrix} \frac{1}{E_x} & -\frac{\upsilon_{xy}}{E_x} & -\frac{\upsilon_{xx}}{E_x} \\ -\frac{\upsilon_{xy}}{E_x} & \frac{1}{E_y} & -\frac{\upsilon_{xy}}{E_x} \end{bmatrix} \begin{Bmatrix} \sigma_x \\ \sigma_y \\ \sigma_x \end{Bmatrix} = \begin{Bmatrix} \varepsilon_x \\ \varepsilon_y \end{Bmatrix} \tag{4.4}$$

where $E_x =$ the resilient modulus in the horizontal direction; $E_y =$ the resilient modulus in the vertical direction; $\sigma_x =$ the horizontal (confining) stress; $\sigma_y =$ the vertical (axial) stress; $\varepsilon_x =$ the horizontal strain; $\varepsilon_y =$ the vertical strain; $\upsilon_{xx} =$ the Poisson's ratio in the horizontal plane; and $\upsilon_{xy} =$ the Poisson's ratio in the vertical plane. This constitutive model can be rewritten in the incremental form as shown in Equation (4.5):

$$\begin{bmatrix} \frac{1}{E_x} & -\frac{\upsilon_{xy}}{E_x} & -\frac{\upsilon_{xx}}{E_x} \\ -\frac{\upsilon_{xy}}{E_x} & \frac{1}{E_y} & -\frac{\upsilon_{xy}}{E_x} \end{bmatrix} \begin{Bmatrix} \Delta\sigma_x \\ \Delta\sigma_y \\ \Delta\sigma_x \end{Bmatrix} = \begin{Bmatrix} \Delta\varepsilon_x \\ \Delta\varepsilon_y \end{Bmatrix} \tag{4.5}$$

It should be noted that the basis for this constitutive model is the theory of elasticity. That means the rigorous term of the moduli used in Equations (4.4) and (4.5) should be elastic modulus. However, the repeated triaxial test results were analyzed by Luo et al. using either Equation (4.4) or (4.5), which indicates that they assumed the resilient modulus was equal to the elastic modulus.

The generalized constitutive model for resilient modulus in Equation (2.11) was also adopted by Luo et al. to formulate E_y. However, they assumed that E_x is n times E_y, in which n was obtained using regression analysis on the triaxial test results.

Considering the above assumptions, taking the cross-anisotropy into account made Luo et al.'s analysis comparatively more complex. Accordingly, Luo et al. adjusted a test protocol that allows estimation of all cross-anisotropic characteristics using the triaxial test measurements. A crushed granite material with a maximum dry density of 2.16×10^3 kg/m^3 and optimum water content of 6.7 % was used in their study. Three types of geogrids were used in the reinforced samples specifications of which are presented in Table 4.5. The samples were reinforced by placing the geogrid at the mid-height, at one-quarter below the mid-height or at the bottom of the triaxial specimen. Repeated loading triaxial tests were performed on both the unreinforced and geogrid-reinforced aggregate specimens. The specimens were cylindrical with 15-cm diameter and 15-cm height and were prepared at the optimum water content determined using the modified Proctor compaction test.

In each test, the sample was first pre-conditioned by applying a deviatoric stress of 103.4 kPa for 500 cycles under a constant confining stress of 103.4 kPa. Then the sample went through 10 stress states, in which certain static axial and confining stresses were applied while the associated dynamic stress was repeated for 25 times, with 1.5 seconds of loading and 1.5 seconds of unloading. The test protocol is summarized in Table 4.6. The axial and radial deformations, measured using Linear Variable Differential Transformer

(LVDTs), were analyzed based on the constitutive models in Equations (4.4) and (4.5) to determine the cross-anisotropic properties.

Table 4.5: Properties of Geogrids Used by Luo et al. (2017)

Geosynthetic Type	Aperture Shape	Aperture Dimension (mm)	Tensile stiffness @2% strain (KN/m)		Rib thickness (mm)
			MD	CMD	
TX-1	Triangle	40x40x40	225	225	1.2
TX-2	Triangle	40x40x40	300	300	1.5
BX-3	Rectangle	25x33	300	450	0.76

Note: MD: Machine direction CMD: Cross-machine direction
TX-1 should be TX140 (current product ID) of Tensar Corporation
TX-2 should be TX160 (current product ID) of Tensar Corporation
BX-3 should be BX1100 (current product ID) of Tensar Corporation
Rib thickness data were not provided in the original publication. The thicknesses listed here were from current product specifications of Tensar Corporation.

Table 4.6: Repeat Loading Triaxial Test Protocol Adopted by Luo et al. (2017)

Stress state	Static stress (kPa)		Dynamic stress (kPa)	
	σ_y	σ_x	$\Delta\sigma_y$	$\Delta\sigma_x$
1	40	25	5	0
2	50	25	10	0
3	70	40	10	0
4	130	60	20	0
5	150	70	20	0
6	170	100	20	0
7	220	120	30	0
8	250	140	30	0
9	250	120	30	0
10	250	105	30	0

Luo et al. (2017) reported the normalized resilient modulus ratios of the geogrid-reinforced samples to the unreinforced samples using Equations (4.6) and (4.7):

$$R_{M_{r,x}} = \frac{E_{x-geo}}{E_{x-control}} \tag{4.6}$$

$$R_{M_{r,y}} = \frac{E_{y-geo}}{E_{y-control}} \tag{4.7}$$

where $R_{M_{r,x}}$ = the improvement ratio of the resilient modulus in the horizontal direction; $R_{M_{r,y}}$ = the improvement ratio of the resilient modulus in the vertical direction; $E_{x-geo} =$ the horizontal resilient modulus of the geogrid-reinforced specimen; $E_{x-control} =$ the horizontal resilient modulus of the unreinforced specimen; $E_{y-geo} =$ the vertical resilient modulus of the geogrid-reinforced specimen; and $E_{y-control} =$ the vertical resilient modulus of the unreinforced specimen. The results reported by Luo et al. (2017) were compared with predictions from the model developed in this study.

Luo et al. found that the addition of geogrids increased the vertical and horizontal resilient moduli by approximately 10-20 percent for specimens with 15-cm diameter and 15-cm height. Previous repeated loading triaxial tests conducted on higher crushed aggregate specimens (e.g., 30-cm-high specimens in Nazzal (2007) study; 40-cm-high specimens in Moghaddas-Nejad & Small (2003) study), however, reported only a slight improvement in the resilient modulus. Therefore, Luo et al. inferred that the specimen dimensions might significantly influence the quantified benefit of geogrids. Nonetheless, no solid conclusion can be made based on their limited test results.

4.3.2 Considerations in this Model for Comparison with Luo et al. (2017) Study

The geogrid influence was characterized in the analytical model by the improvement ratio of elastic modulus, R_E, as defined in Equation (4.2). To obtain R_E from the model, inputs are required concerning the pavement geometry, material properties and traffic loading conditions. These aspects are discussed separately in the following subsections.

4.3.2.1 Model Inputs of Pavement Geometry

The analytical model proposed in this study considered an infinitely long pavement under strip loading, and the pavement was assumed to be composed of asphalt, base and subgrade layers. Consequently, the geometry in the model was more complex compared to the triaxial test specimen. As shown in Table 4.7, typical values were assumed for the thickness of pavement layers. However, the geosynthetic influence zone was assumed to be only part of the base course, and its thickness was set to be consistent with the specimens' height in the Luo et al.'s study.

Table 4.7: Geometric Parameters Assumed in the Analytical Model to Compare with Luo et al. Study

Input parameter	Value
HMA thickness (m)	0.1524
Base course thickness (m)	0.3556
Thickness of geosynthetic influence zone (m)	0.15

4.3.2.2 Model Inputs of Material Properties

The base aggregates and geogrids were two materials that needed to be characterized in the analytical model. As for the base aggregates, a critical property is the resilient modulus after compaction, which would serve as the model input of the original elastic modulus of the base material without geosynthetics, i.e., E_u. To be consistent with Luo et al.'s study, E_u was estimated based on the available information of the crushed aggregate material used in their triaxial tests. However, neither the resilient modulus after compaction nor California Bearing Ratio (CBR) was explicitly provided by Luo et al. (2017) for the crushed aggregate used in their specimens. Instead, the resistance R-value was reported in their study, and it was used herein to estimate the resilient modulus using the following correlation (AASHTO, 1993):

$$M_r = 1155 + 555R \quad (4.8)$$

where $M_r =$ resilient modulus (psi), and it was considered as an estimate for elastic modulus. The value was further expressed in kPa.

The median R-value reported by Luo et al. was 70. By substituting it into Equation (4.8), the resultant estimate of E_u was 275,825 kPa. Since Luo et al. took the cross-anisotropy into account, the analytical model presented in this study was also used to estimate the modulus improvement ratios separately for the horizontal and vertical directions to allow comparison with Luo et al.'s results. In addition, Luo et al. seemed to give more weight to the vertical resilient modulus E_y (by using the constitutive model in Equation (2.11) to formulate E_y while expressing the horizontal resilient modulus E_x as n times E_y). Therefore, the above estimated E_u, 275,825 kPa, was assigned for the original vertical elastic modulus in the model, while the original horizontal elastic modulus was estimated as $0.45 \times 275{,}825 = 124{,}121$ kPa. The factor 0.45 was the n value reported by Luo et al. in their study.

On the other hand, geogrid properties were also important inputs of the analytical model. The inputs of the geogrid geometric characteristics were specified according to Table 4.5. However, as discussed earlier in Section 4.2.2.2, the tensile stiffness reported in Table 4.5 could not be directly used to represent the confined tensile stiffness of geogrids subjected to small deformations in pavements. Biaxial geogrid BX-3 in Luo et al.'s study was the same as the geogrid BX-2 in Nazzal's (2007) study. As discussed in Section 4.2.2.2, Roodi (2016) has reported the average confined stiffness for this product as 650 kN/m. This value was adopted herein as the stiffness input for geogrid BX-3. However, for triaxial geogrids TX-1 and TX-2, representative confined stiffness values were not found in the literature. In Section 4.2.2.2, a constant correction factor 1.44 was adopted to convert

the tensile stiffness at 2% strain to the confined stiffness. However, due to the geometric difference between triaxial and biaxial geogrids, it might not be appropriate to directly apply this factor to these two triaxial geogrids. Instead, values listed in Table 4.8 were assumed for geogrids TX-1 and TX-2. It should be noted that the confined stiffness values assigned for TX-1 and TX-2 were approximate and might be of low accuracy.

Table 4.8: Confined Tensile Stiffness Assumed for Geogrids Used in Luo et al. Study

Geogrid Type	Confined tensile stiffness J_c (kN/m)
TX-1	650
TX-2	700
BX-3	650

4.3.2.3 Model Inputs of Traffic Loading Conditions

Together with the specified pavement geometry and the existing assumptions of stress forms, the traffic loading conditions were considered by the analytical model to determine the stress distribution in the geosynthetic influence zone of the base course. Since the traffic load was assumed to be a uniform strip load, the related model inputs included the width of strip load, i.e., the width of the wheel, and the strip load magnitude, i.e., the tire pressure. The wheel width was assumed to be 0.21 m. As for the tire pressure, it was not directly specified. Instead, since Luo et al. applied the associated dynamic stress to their triaxial test samples at each stress state, the magnitude of constant b in the vertical stress assumption of our model was set to be consistent with the dynamic stress at each stress state, and the tire pressure was back-calculated from the magnitude of constant *b* using Equation (a.2) in Appendix A. With the tire pressure obtained, the constant *d* in the horizontal stress assumption could be calculated using Equation (a.1) in Appendix A. Because the constants b and d were determined based on a specific stress state, the elastic

modulus improvement ratios were also separately predicted by our model for those 10 stress states in Luo et al. study and then compared with their test results.

4.3.3 Comparison between Model Predictions and Test Results of Luo et al. Study

In addition to the model inputs considered in Section 4.3.2, the aggregate-geogrid interface friction angle was assumed to be 40°, and the Poisson's ratio of the base aggregate material was assumed to be 0.3. The predicted improvement ratios R_E were compared with the results of R_{Mr} reported by Luo et al. in their study. To more clearly communicate the comparison results, the improvement in modulus was further expressed as the percent increase of modulus (i.e., $(R_E - 1) \times 100\%$ and $\left(R_{M_r} - 1\right) \times 100\%$). The comparison was conducted separately for three geogrid types and ten stress states, as shown in Figures (4.4) to (4.9). It is worth mentioning that only results from Luo et al. study concerning the samples with the geogrid placed at the mid-height were adopted herein since the model assumed the geogrid to be placed at the mid-depth of the base course. In addition, when comparing with the results of Luo et al., the correction factor α in the model was only determined using Approach 1 in Appendix C to avoid the complexity of the geometric calculation of triaxial geogrids.

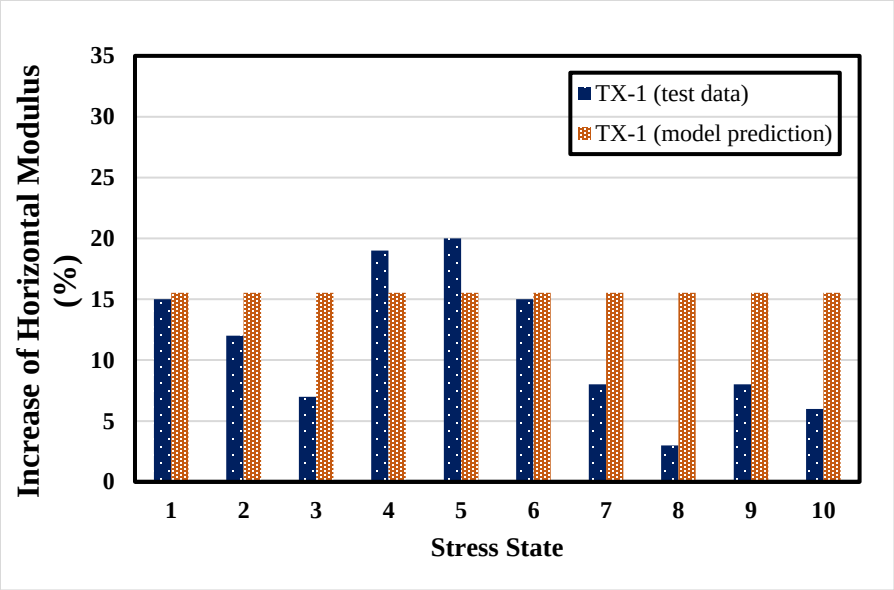

Figure 4.4: Comparison between $\left(R_{M_{r,x}} - 1\right) \times 100\%$ of the geogrid TX-1 in Luo et al. Study and $(R_E - 1) \times 100\%$ predicted using the analytical model

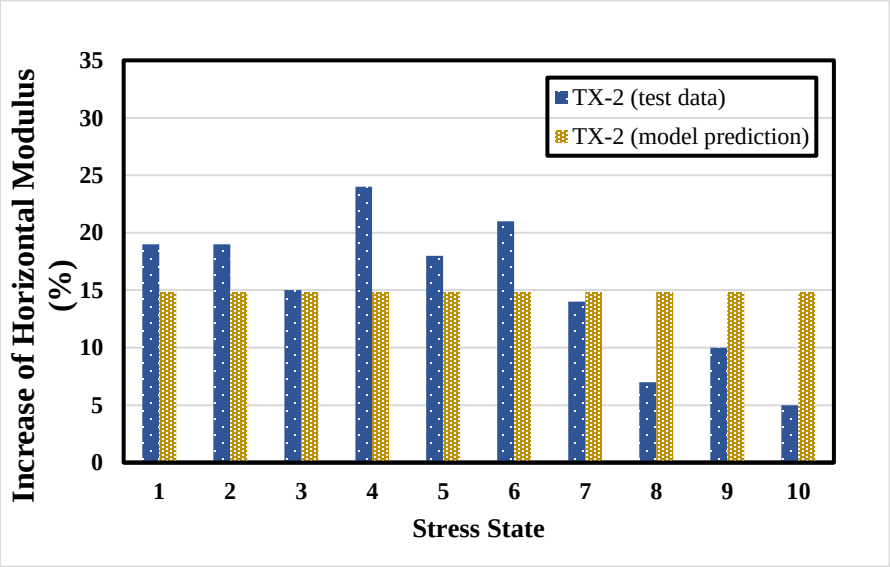

Figure 4.5: Comparison between $\left(R_{M_{r,x}} - 1\right) \times 100\%$ of the geogrid TX-2 in Luo et al. Study and $(R_E - 1) \times 100\%$ predicted using the analytical model

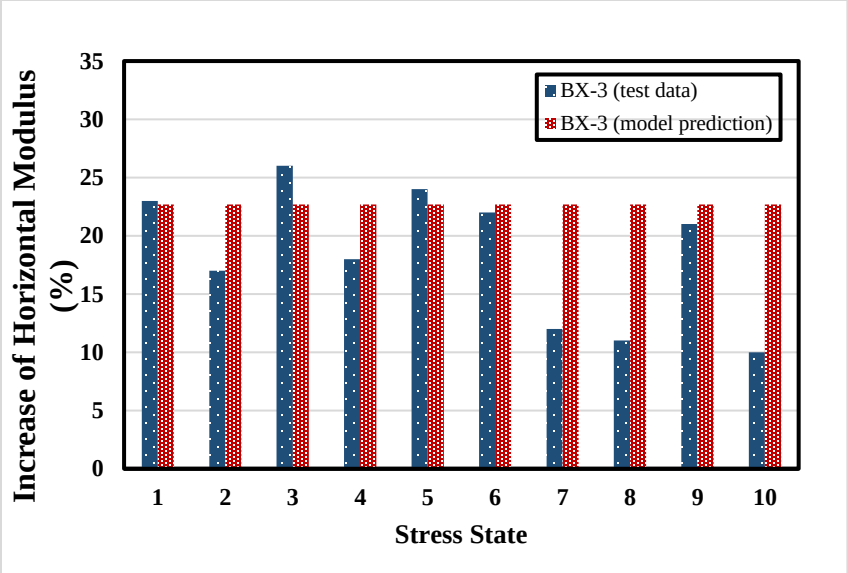

Figure 4.6: Comparison between $\left(R_{M_{r,x}} - 1\right) \times 100\%$ of the geogrid BX-3 in Luo et al. Study and $(R_E - 1) \times 100\%$ predicted using the analytical model

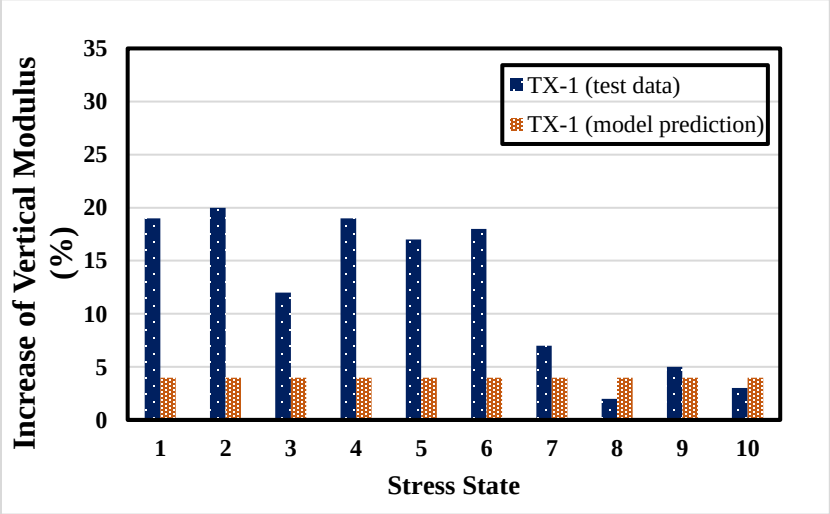

Figure 4.7: Comparison between $\left(R_{M_{r,y}} - 1\right) \times 100\%$ of the geogrid TX-1 in Luo et al. Study and $(R_E - 1) \times 100\%$ predicted using the analytical model

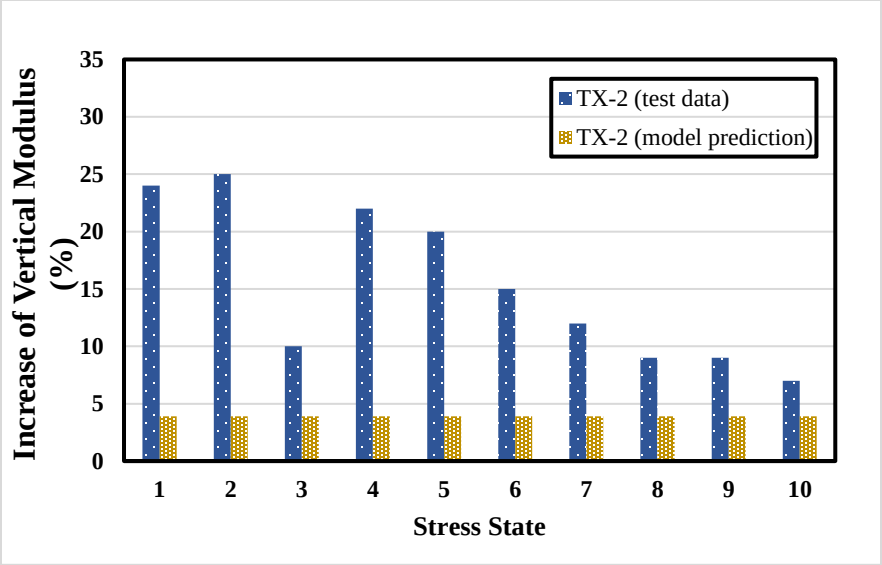

Figure 4.8: Comparison between $\left(R_{M_{r,y}} - 1\right) \times 100\%$ of the geogrid TX-2 in Luo et al. Study and $(R_E - 1) \times 100\%$ predicted using the analytical model

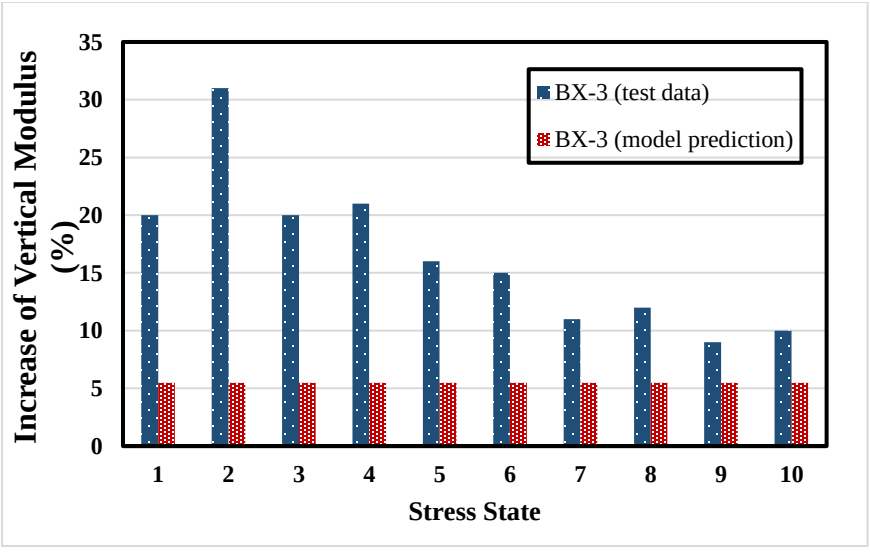

Figure 4.9: Comparison between $\left(R_{M_{r,y}} - 1\right) \times 100\%$ of the geogrid BX-3 in Luo et al. Study and $(R_E - 1) \times 100\%$ predicted using the analytical model

It was found that the R_E predicted by the analytical model for a certain geogrid product did not vary with the stress state. In other words, since each stress state corresponds to a specific tire pressure input in the model, this invariance indicates that the model prediction of R_E does not depend on the tire pressure. It can be noticed that the horizontal modulus improvement ratios predicted by the proposed model are generally consistent with the test results of Luo et al. Our model predictions of the vertical modulus improvement ratios, however, are generally lower than the values reported by Luo et al. Since the original vertical and horizontal elastic moduli of the natural base material were specified as 275,825 kPa and 124,121 kPa respectively in the model, this comparison result may indicate that the model tends to give conservative estimates of the modulus improvement if the natural base material already has a relatively high stiffness, for example, in the vertical direction in this case.

4.4 COMPARISON WITH YANG & HAN (2012) MODEL

Yang and Han (2012) developed an analytical model to evaluate the resilient modulus and permanent deformation of geosynthetic-reinforced unbound granular material. They also validated the geogrid-related part of their model using Nazzal's (2007) resilient modulus test results. A parametric analysis was performed by Yang and Han on their analytical model to evaluate the effects of material modulus, stress level, sample diameter and dilation angle on the benefit of geosynthetic reinforcement.

Results of Yang and Han's parametric analysis concerning the influence of material modulus on the quantified geogrid benefit were used to compare with the predictions from the model proposed in this study. It should be noted that the predictions were made by the proposed model based on the inputs in the parametric analysis of Yang and Han. Therefore, this comparison was not a rigorous validation using experimental results. However, since

these models, developed based on different methodologies, both exhibited consistency with test results of Nazzal's (2007) study, it was of special meaning to compare their results when parallel model inputs were specified.

4.4.1 Overview of the Parametric Analysis Conducted by Yang and Han (2012)

In the parametric analysis performed by Yang and Han (2012), the input parameters for the baseline case, as listed in Table 4.9, were specified based on the typical material properties of coarse-grained unbound granular materials and polypropylene geosynthetics. The confining and repeated deviatoric stresses in the baseline case of their analysis were set as 35 kPa and 103 kPa, respectively, to represent the typical stress experienced in the base or subbase, as suggested by NCHRP Project 1-28A (Witczak, 2003).

Table 4.9: Baseline Input Parameters for the Parametric Analysis (Yang and Han, 2012)

Input parameters	Value
Sample size	D = 15 cm
	H = 30 cm
Resilient modulus parameters	k1 = 1,500
	k2 = 0.5
	k3 = -0.2
Permanent deformation parameters	$(\varepsilon 0/\varepsilon r) = 80$
	$\rho = 1{,}000$
	$\beta = 0.4$
Geosynthetic tensile stiffness M	200 kN/m
Geogrid Poisson's ratio ν_g	0.3
Interaction spring stiffness k	200,000 kN/m^3
Dilation angle ψ	0°
N_{limit}	100,000

Instead of the normalized resilient modulus ratios of the geogrid-reinforced samples to the unreinforced samples, Yang and Han used the percentages of resilient modulus increase to represent the geogrid benefit, as defined in Equation (4.9):

$$\Delta M_{r,\%} = \frac{M_{r,reinf} - M_{r,unreinf}}{M_{r,unreinf}} \times 100\% \quad (4.9)$$

Where $\Delta M_{r,\%} =$ the increase in resilient modulus (percent), $M_{r,reinf} =$ the resilient modulus of the reinforced sample, and $M_{r,unreinf} =$ the resilient modulus of the unreinforced sample.

Our model predictions of $\Delta M_{r,\%}$ were compared with those of Yang and Han by varying two input parameters: geosynthetic tensile stiffness and $M_{r,unreinf}$. It is worth mentioning that $M_{r,unreinf}$ was controlled by Yang and Han (2012) by changing k1 in the constitutive model (Equation (2.11)) of resilient modulus. The parametric analysis results of Yang and Han concerning these two parameters are shown in Figure 4.10.

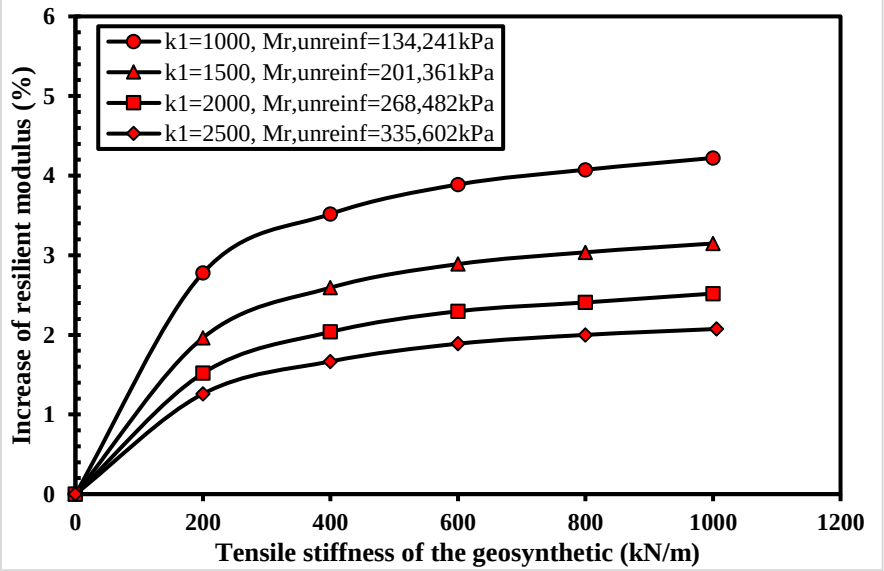

Figure 4.10: Effect of material modulus on the quantified geogrid benefit (adapted from Yang and Han (2012))

It can be noticed from Figure 4.10 that the increase in the geosynthetic tensile stiffness increases the quantified geosynthetic benefit while the increase in $M_{r,unreinf}$ decreases the quantified geosynthetic benefit. Both trends have been reported to be nonlinear.

4.4.2 Input Parameters Specified in the Analytical Model

Comparison between our model predictions and the results of Yang and Han was conducted separately for the four values of $M_{r,unreinf}$ and five values of geosynthetic tensile stiffness as shown in Figure 4.10. The values of $M_{r,unreinf}$ in the legend of Figure 4.10 were directly used as the inputs of the original base elastic modulus in our model. The values of geosynthetic tensile stiffness on the horizontal axis of Figure 4.10, on the other hand, were also directly considered as our model inputs of the confined geosynthetic tensile stiffness. Yang and Han used this geosynthetic tensile stiffness in their definition of the additional confining stress, so this stiffness should have been considered in their model as the confined stiffness, and no more correction is required herein.

Since the sample height was specified as 30 cm in the parametric analysis of Yang and Han, the geometric inputs of the pavement considered in our model were selected to be the same as those presented in Table 4.3. In addition, since the confining and repeated deviatoric stresses in the parametric analysis of Yang and Han were set as 35 kPa and 103 kPa, respectively, constant *b* in the vertical stress assumption of our model was set as -138 kPa while constant *d* in the horizontal stress assumption of our model was set as -35 kPa. The tire pressure was back calculated from the magnitude of constant *b*. Furthermore, the Poisson's ratios of the aggregates and geosynthetics were assumed to be 0.3. The aggregate-geosynthetic interface friction angle, on the other hand, was set to be 36°, 38°,

40° and 42°, respectively for the four values of $M_{r,unreinf}$, with higher angle for higher $M_{r,unreinf}$.

4.4.3 Comparison of Predictions from Two Models

As shown in Figures 4.11 to 4.14, the predictions of the percent increase in resilient modulus from our model and Yang & Han model were compared based on five values of confined geosynthetic stiffness and separately for four values of $M_{r,unreinf}$.

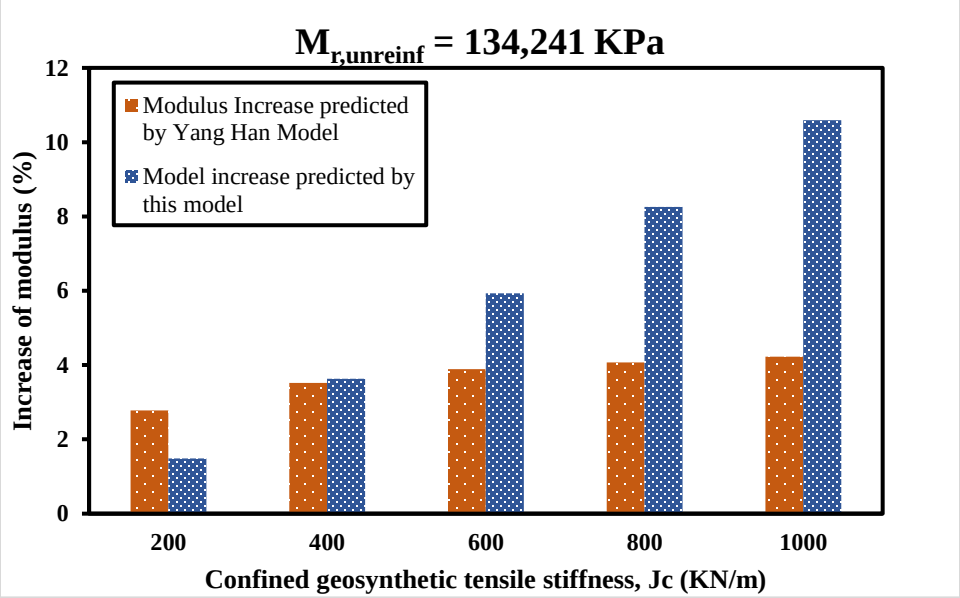

Figure 4.11: Comparison of the model predictions of $\Delta M_{r,\%}$ for $M_{r,unreinf} = 134{,}241\ kPa$

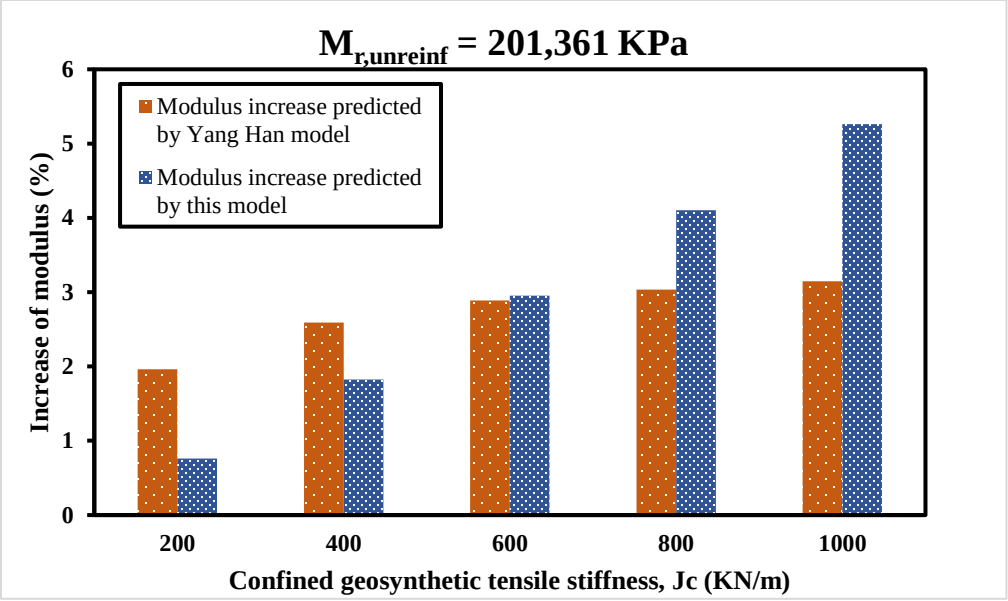

Figure 4.12: Comparison of the model predictions of $\Delta M_{r,\%}$ for $M_{r,unreinf} = 201{,}361\ kPa$

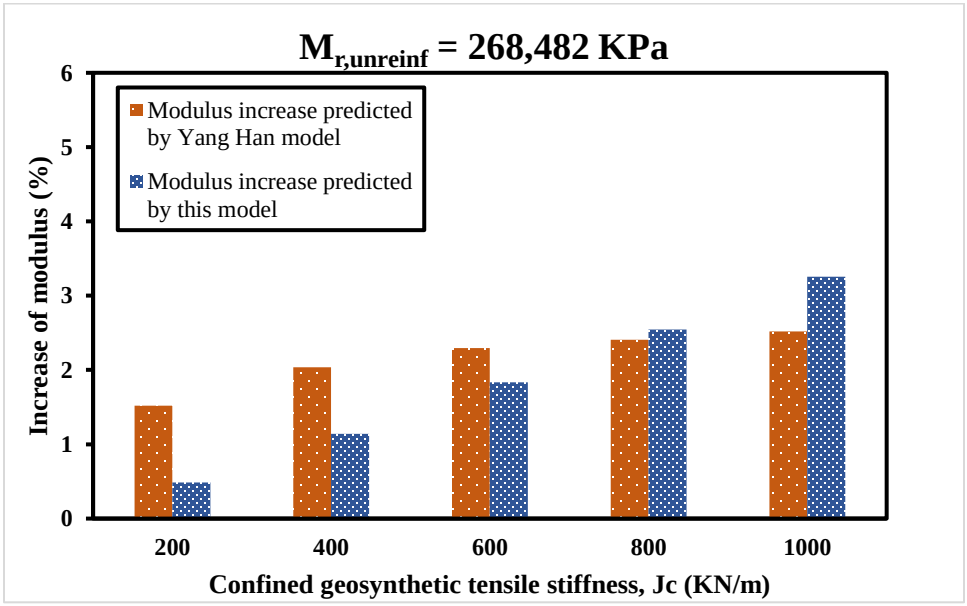

Figure 4.13: Comparison of the model predictions of $\Delta M_{r,\%}$ for $M_{r,unreinf} = 268{,}482\ kPa$

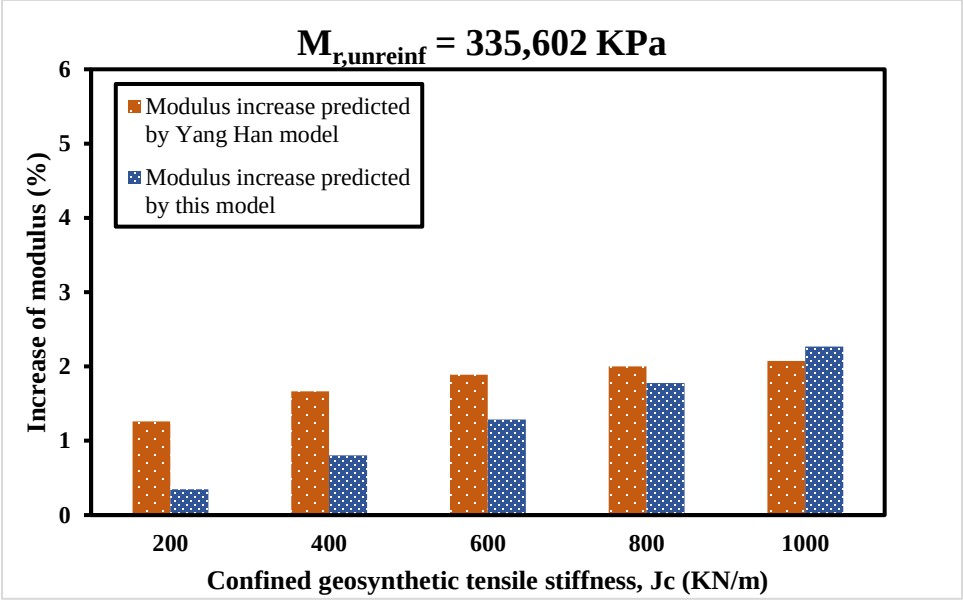

Figure 4.14: Comparison of the model predictions of $\Delta M_{r,\%}$ for $M_{r,unreinf} = 335{,}602\ kPa$

Overall, a reasonably good agreement was found between the predictions from the two models. It can be noticed that the modulus increase predicted by Yang and Han only show small change when the geosynthetic tensile stiffness is increased. Our model prediction of the modulus increase, however, is much more sensitive to the magnitude of the geosynthetic tensile stiffness. As a result, when the specified geosynthetic tensile stiffness is very low, e.g., 200 kN/m, the modulus increase estimated by our model is much lower compared to that predicted by Yang and Han (2012). On the other hand, our model predictions of the modulus increase are higher than those of Yang and Han model when high geosynthetic stiffness and low original base material modulus are assigned for the mode inputs. Nevertheless, these differences are mainly attributed to the different assumptions and methodologies adopted in these two models, since similar ranges of the modulus increase can be observed from results of both models.

Chapter 5: Sensitivity Analysis

5.1 OVERVIEW

This chapter presents the findings of a sensitivity analysis that was conducted on the proposed analytical model. The parameters considered in this analysis can be divided into three categories: material properties, pavement geometry and traffic loading conditions. Specifically, the parameters that were studied under each category are as follows:

1) Material properties parameters
- the original elastic modulus of the base course without geosynthetics (E_u),
- the confined geosynthetic tensile stiffness J_c,
- the stiffness of soil-geosynthetic composite K_{SGC},
- the aggregate-geosynthetic interface friction angle ϕ, and
- the Poisson's ratio of the aggregates and geosynthetics μ;

2) Pavement geometry parameters
- the thickness of the asphalt layer h_1,
- the half thickness of the base course h_2,
- the half thickness of the geosynthetic influence zone t, and
- the half thickness of the geosynthetic t_s; and

3) Traffic loading parameters
- the tire pressure p and
- the wheel width W_w.

The following discussions on the effect of these parameters on the model results are also organized according to the three categories mentioned above.

As listed in Table 5.1, the parameter values specified for the baseline case reflect a typical flexible pavement design. By varying one of these parameters while keeping the rest the same as in the baseline case, the effect of that parameter on the resultant geosynthetic benefit was evaluated. The geosynthetic benefit was quantified using the elastic modulus improvement ratio R_E, as defined in Equation (4.2). For simplicity, only Approach 1 in Appendix C was used to calculate the correction factor α, which was further utilized to calculate all the values of R_E reported in this chapter.

Table 5.1: Baseline Input Parameters for Sensitivity Analysis

Category	Input parameter	Value
Material Properties	E_u (kPa)	220,000
	J_c (kN/m)	650
	K_{SGC} ((kN/m)^2/mm)	36.4
	ϕ (°)	38
	μ	0.3
Geometry	h_1 (m)	0.1524
	h_2 (m)	0.1778
	t (m)	0.0762
	t_s (mm)	0.76
Traffic Loading	p (kPa)	241.32
	W_w (m)	0.21

5.2 EFFECT OF MATERIAL PROPERTIES

5.2.1 Original Elastic Modulus

The parameter analyzed in this section is the original elastic modulus of the base course without geosynthetic, which has been denoted by E_u. As shown in Figure 5.1, an

increase in E_u reduces the elastic modulus improvement ratio R_E. This trend is nonlinear. It is understandable that the geosynthetic stiffening effect will be less apparent if the base aggregate material itself has already been very stiff. Therefore, the trend shown in Figure 5.1 is consistent with the expectation. It can be observed that 33% increase in elastic modulus was obtained when E_u was 100,000 kPa while the improvement was only 5% when E_u was 300,000 kPa. This drastic change indicates that the original modulus of the base aggregate has a significant impact on the modulus improvement caused by the geosynthetic.

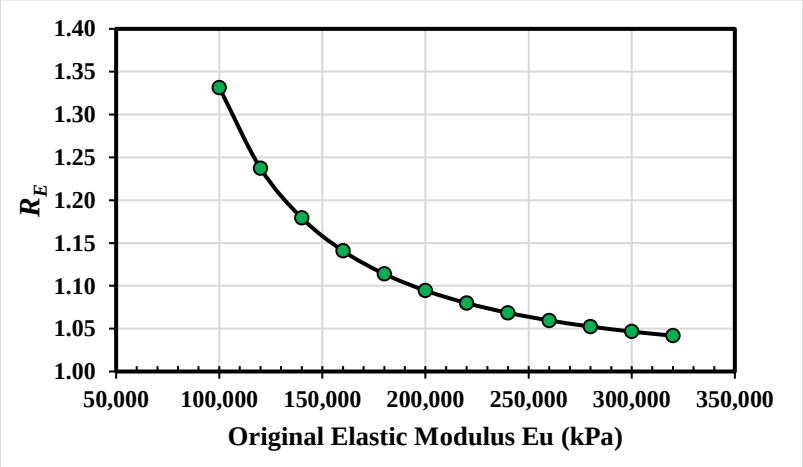

Figure 5.1: Effect of the original elastic modulus E_u on the predicted elastic modulus improvement ratio R_E

5.2.2 Confined Geosynthetic Tensile Stiffness

The confined geosynthetic tensile stiffness, denoted by J_c, is expected to be an important parameter representing the geosynthetic ability to stiffen the base aggregate material. As shown in Figure 5.2, the predicted elastic modulus improvement ratio R_E increases with the increasing J_c. This trend is almost linear.

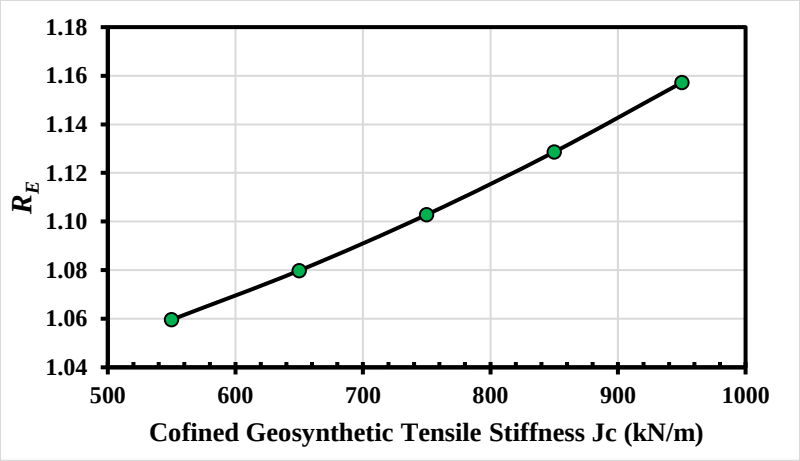

Figure 5.2: Effect of the confined geosynthetic tensile stiffness J_c on the predicted elastic modulus improvement ratio R_E

Figure 5.3 presents the combined effect of E_u and J_c. In short, the predicted R_E increases with the decreasing E_u and the increasing J_c. It can be noticed that the influence of the confined geosynthetic stiffness J_c is less significant when the original elastic modulus of the base material E_u is large enough.

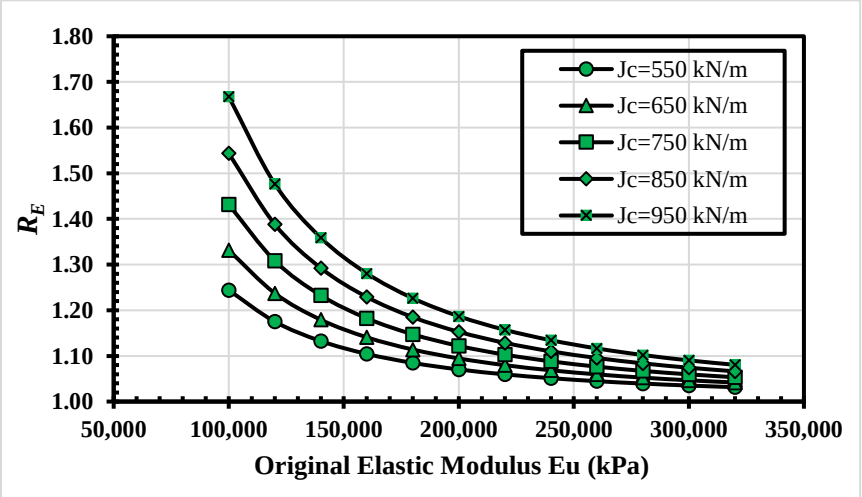

Figure 5.3: Combined effect of the original elastic modulus E_u and the confined geosynthetic stiffness J_c on the predicted elastic modulus improvement ratio R_E

5.2.3 Stiffness of the Soil-Geosynthetic Composite K_{SGC}

If the correction factor α is determined using Approach 3 in Appendix C, α will be a function of the stiffness of the soil-geosynthetic composite (K_{SGC}), which is a parameter proposed by the SGC model to characterize the soil-geosynthetic interaction under small displacements. With α determined in this way, since the predicted increased elastic modulus (E_r) is a function of α as indicated by Equation (3.57), E_r is also a function of K_{SGC}.

As shown in Figure 5.4, the correction factor α increases with the increasing K_{SGC}. Specially, when K_{SGC} was increased from 29.7 to 47.6 (kN/m)^2/mm, α increased from 3.8 to 5.5. The trend is perfectly linear.

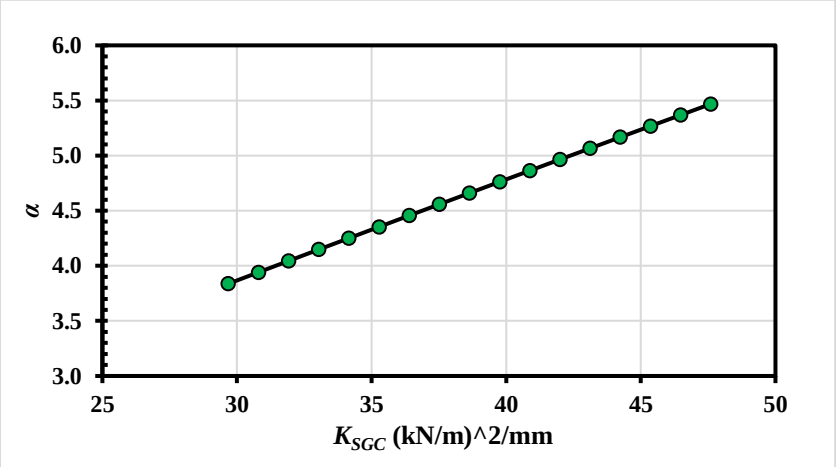

Figure 5.4: Effect of K_{SGC} on the correction factor α

As shown in Figure 5.5, the predicted elastic modulus improvement ratio (R_E) increases with increasing K_{SGC}. Specifically, when K_{SGC} was increased from 29.7 to 47.6 (kN/m)^2/mm, R_E increased from 1.055 to 1.126. The trend is almost linear. Such a change in R_E with K_{SGC} indicates that K_{SGC} has a comparatively large impact on the elastic modulus improvement predicted in this model. Furthermore, the combined effect of the original

elastic modulus (E_u) and K_{SGC} on the predicted R_E is shown in Figure 5.6. It was found that the influence of K_{SGC} reduced when the original elastic modulus (E_u) of the base material was increased. If the non-stabilized base material has a very large elastic modulus (E_u), the effect of K_{SGC} on the predicted R_E will be minimized. However, when a base material with low E_u was stabilized with a geosynthetic with high K_{SGC}, the percentage of elastic modulus improvement could be comparatively high, for example, 52% when E_u = 100,000 kPa and K_{SGC} = 47.6 (kN/m)^2/mm. It can also be noticed that the percentage of elastic modulus increase was 24% when E_u = 100,000 kPa and K_{SGC} = 30.8 (kN/m)^2/mm. The change from 24% to 52% by increasing K_{SGC} from 30.8 to 47.6 (kN/m)^2/mm indicates that K_{SGC} can have a significant impact on the predicted elastic modulus improvement when considering a base material with low original elastic modulus.

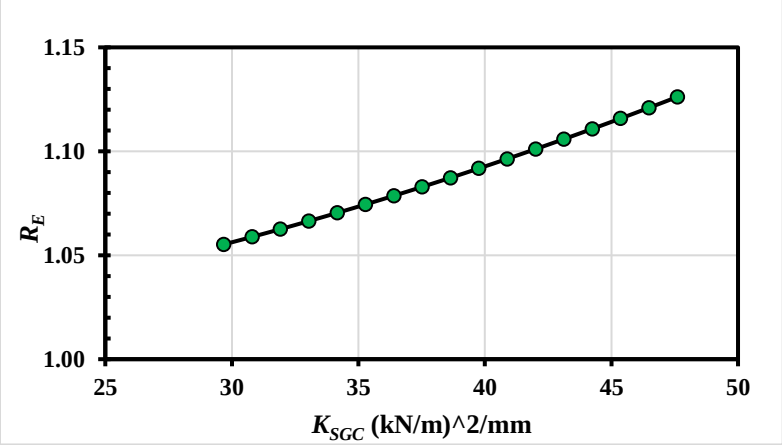

Figure 5.5: Effect of K_{SGC} on the predicted elastic modulus improvement ratio R_E

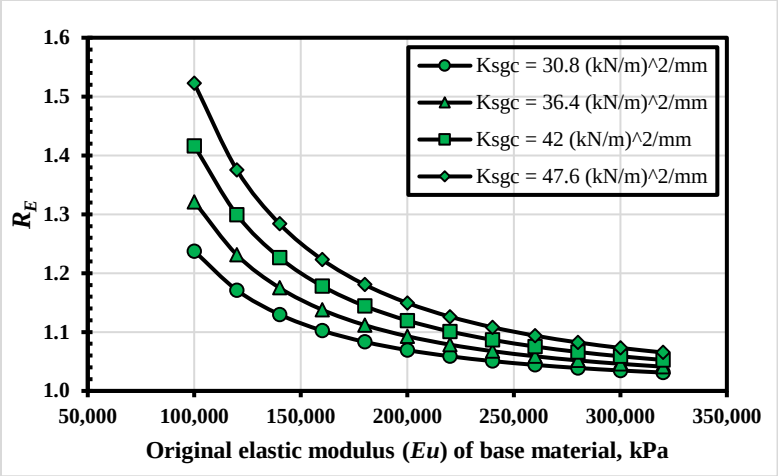

Figure 5.6: Combined effect of the original elastic modulus E_u and K_{SGC} on the predicted elastic modulus improvement ratio R_E

5.2.4 Aggregate-Geosynthetic Interface Friction Angle

The aggregate-geosynthetic interface friction angle ϕ is used in Equation (c.4) in Appendix C to determine the correction factor α. Considering how the correction factor α is defined in Approach 1 of Appendix C, the increasing ϕ will result in a higher α, which will ultimately yield a higher R_E. These relationships are confirmed in Figures 5.7 and 5.8, in which both α and R_E increase with the increasing ϕ. However, the increases in α and R_E are both very small, indicating that the model prediction is insensitive to the change in the aggregate-geosynthetic interface friction angle.

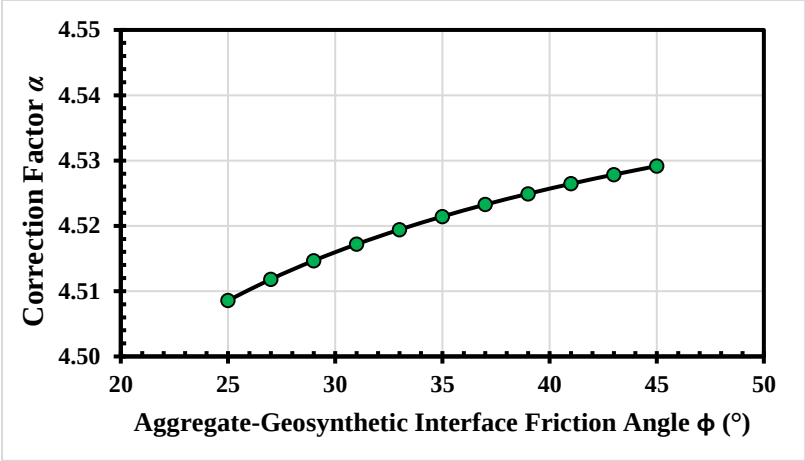

Figure 5.7: Effect of the aggregate-geosynthetic interface friction angle ϕ on the correction factor α

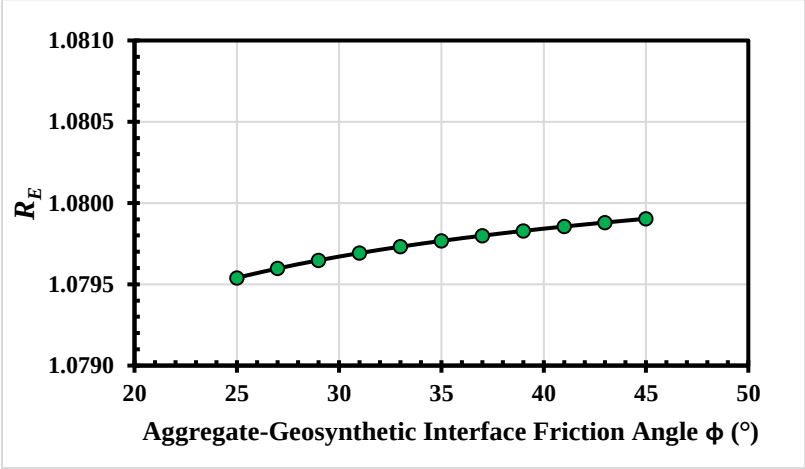

Figure 5.8: Effect of the aggregate-geosynthetic interface friction angle ϕ on the predicted elastic modulus improvement ratio R_E

5.2.5 Poisson's Ratio of the Base Aggregate

As shown in Figure 5.9, the predicted elastic modulus improvement ratio R_E increases linearly with the increasing Poisson's ratio of the base aggregate. Since Poisson's ratio is the negative of the ratio of (signed) transverse strain to (signed) axial strain, larger Poisson's ratio corresponds to larger aggregate lateral movement when certain amount of

vertical deformation occurs. In addition, comparatively larger displacements in the geosynthetic is expected for the larger aggregate lateral movement. The larger displacement in the geosynthetics results higher tension developed in the geosynthetic, which eventually provide more confinement to the surrounding aggregates. Accordingly, larger Poisson's ratio is expected to result in higher modulus improvement. The trend observed in Figure 5.9 is consistent with this expectation.

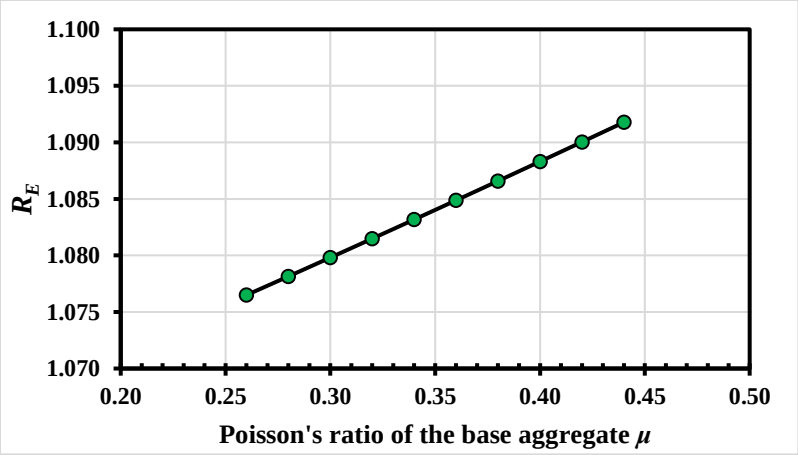

Figure 5.9: Effect of the Poisson's ratio of the base aggregate μ on the predicted elastic modulus improvement ratio R_E

5.3 EFFECT OF GEOMETRIC CHARACTERISTICS

A schematic diagram of the pavement profile with the relevant geometric characteristics marked is shown in Figure 3.4 of Chapter 3.

5.3.1 Pavement Layer Thicknesses (h_1 and h_2)

This sensitivity analysis was conducted based on a simple pavement profile composed of an asphalt layer, a base course and the subgrade. In this study, the thickness of the asphalt layer (h_1) and the half thickness of the base course (h_2) are the two

parameters adopted to represent the geometry of pavement layers. In the developed model, h_1 and h_2 were only used to determine constants b and d in the stress distribution assumptions, as discussed in Appendix A. Figures 5.10 and 5.11 show changes in the predicted R_E when increasing h_1 and h_2, respectively.

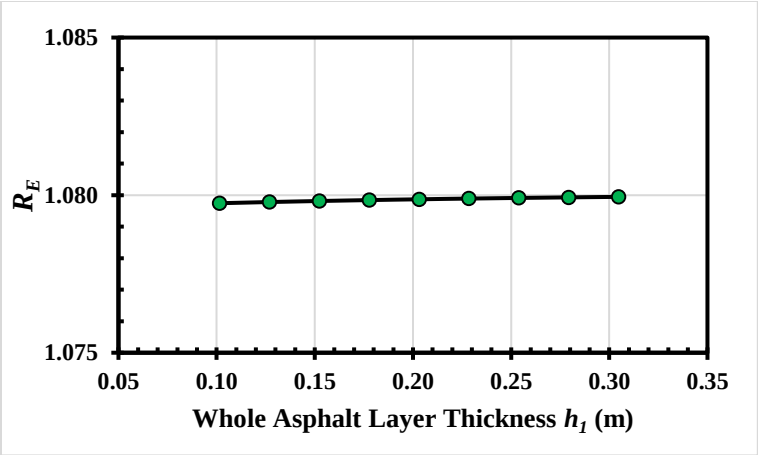

Figure 5.10: Effect of the whole asphalt layer thickness h_1 on the predicted elastic modulus improvement ratio R_E

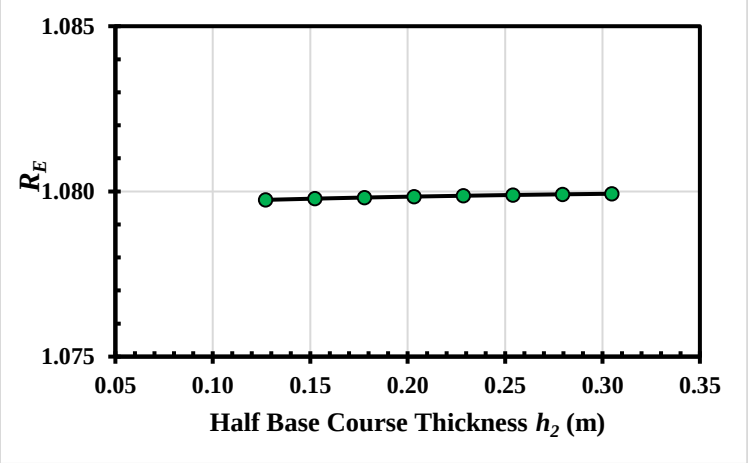

Figure 5.11: Effect of the half base course thickness h_2 on the predicted elastic modulus improvement ratio R_E

It can be noticed from Figure 5.10 and 5.11 that the predicted elastic modulus improvement ratio R_E is insensitive to the changes in h_1 and h_2. This insensitivity may be attributed to the simultaneous decreases in the vertical and horizontal stresses, represented by b and d in the model, with increasing h_1 or h_2. In this way, such a proportional change in stress condition may not significantly influence the benefit brought by the geosynthetic.

5.3.2 Thickness of the Geosynthetic Influence Zone (*2t*)

The thickness of geosynthetic influence zone specifies the region of the base course that can be stabilized by the geosynthetic. For convenience in calculation, the half thickness of the geosynthetic influence zone, denoted by t, is the parameter adopted as the model input. The importance of t is directly reflected in the initial definition of the additional confining stress $\Delta\sigma_3$, as shown in Equation (3.43). Specifically, with a certain geosynthetic tension, a higher value of t indicates a wider range of the base material over which the geosynthetic tension will be distributed, and thus a higher t will reduce the magnitude of $\Delta\sigma_3$ and lower the modulus improvement. This expectation is confirmed by the trend presented in Figure 5.12, where the predicted modulus improvement R_E decreases with increasing t. The trend is nonlinear, and the influence of t on R_E is significant.

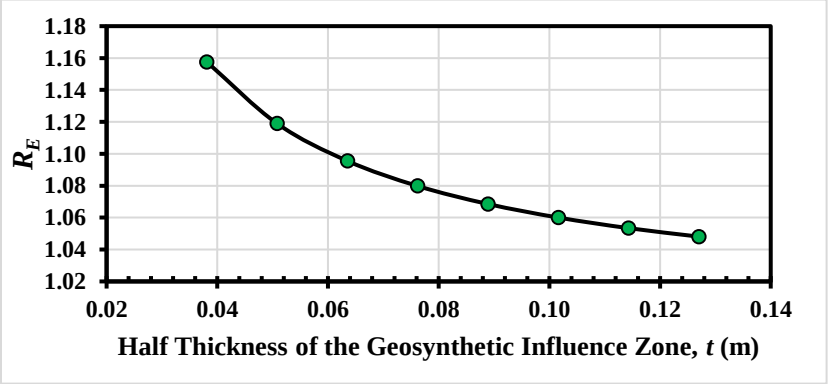

Figure 5.12: Effect of the half thickness of the geosynthetic influence zone *t* on the predicted elastic modulus improvement ratio R_E

5.3.3 Thickness of the Geosynthetic ($2t_{gs}$)

Geosynthetic thickness also has an influence on the predicted modulus improvement when determining the correction factor α using Approach 1 in Appendix C. In Step 2 of that approach, the additional confining stress contributed by the interface skin friction ($\Delta\sigma_{3,fric}$) is calculated using the interface shear stress (τ_y) as expressed by Equation (c.2) of Appendix C. The half thickness of the geosynthetic is denoted by t_{gs}. As shown in Equation (c.2), larger t_{gs} yields larger τ_y, which will further result in a larger $\Delta\sigma_{3,fric}$ when plugged into Equation (c.3). Consequently, as defined in Equation (c.6), the correction factor α will be smaller due to the larger $\Delta\sigma_{3,fric}$, and this smaller α will ultimately result in a smaller modulus improvement R_E predicted by the model. Figures 5.13 and 5.14 show change of α and R_E when varying the geosynthetic thickness. It was confirmed by these figures that both α and R_E decrease with increasing t_{gs}. The predicted modulus improvement was found to be sensitive to the change in geosynthetic thickness.

In this case, the geosynthetic thickness was increased while keeping the confined geosynthetic stiffness constant to ensure a single variable. In reality, however, the confined geosynthetic stiffness may increase with the increasing geosynthetic thickness. This fact should be taken into account when evaluating the sensitivity results.

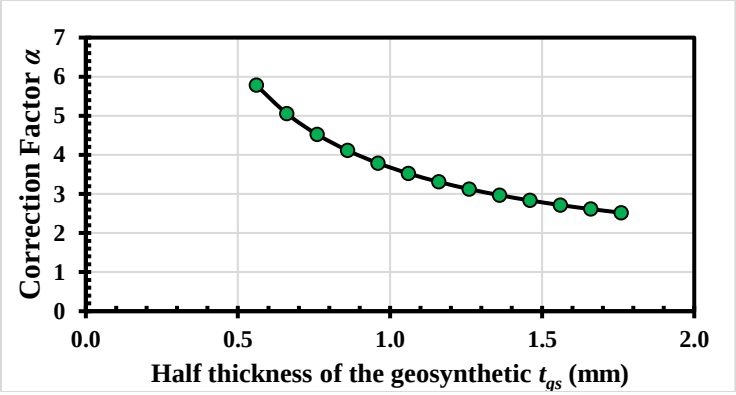

Figure 5.13: Effect of the half geosynthetic thickness t_{gs} on the correction factor α

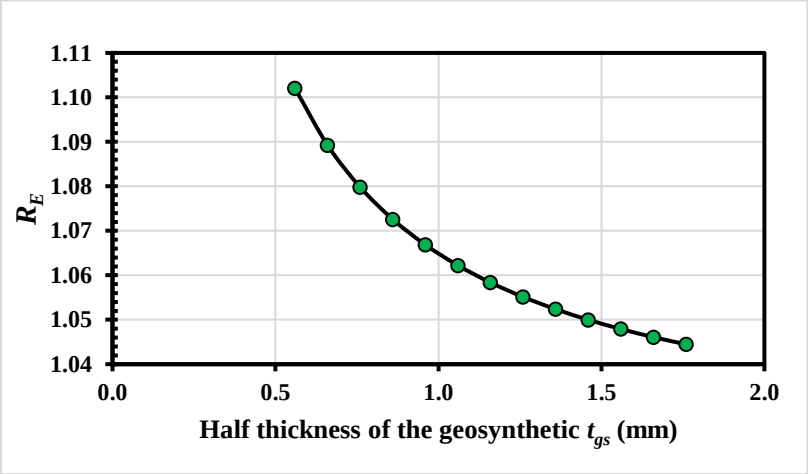

Figure 5.14: Effect of the half geosynthetic thickness t_{gs} on the predicted elastic modulus improvement ratio R_E

5.4 EFFECT OF TRAFFIC LOADING CONDITIONS

5.4.1 Tire Pressure (p)

It was found that the predicted modulus improvement by the developed model did not depend on the tire pressure input, as shown in Figure 5.15. In the final form of the increased elastic modulus (E_r) (Equation (3.57)), the correction factor α is the only place where the tire pressure can play a role. However, the parametric analysis revealed that α

did not change when different tire pressures were assigned. This indicates that the ratio between the bearing resistance contribution and the interface skin friction contribution to the soil-geosynthetic interaction is not affected by the magnitude of the load in our case. The invariance of α with different tire pressures causes the predicted R_E not to be affected by the tire pressure either.

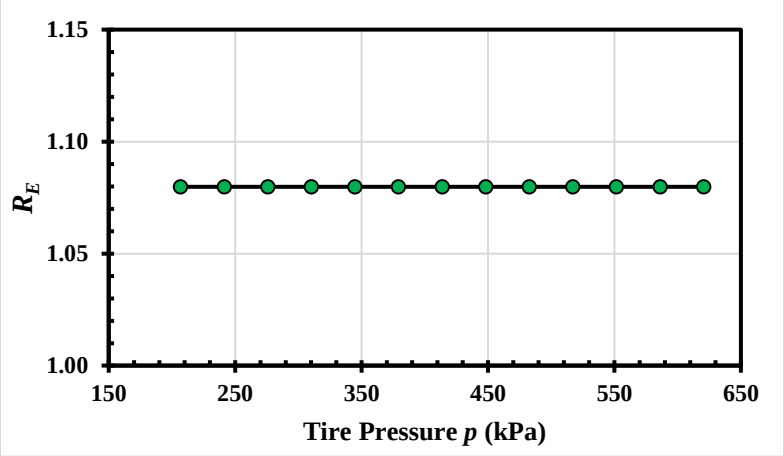

Figure 5.15: Effect of the tire pressure p on the predicted elastic modulus improvement ratio R_E

5.4.2 Wheel Width (*Ww*)

The wheel width is used to determine the stress distribution within the geosynthetic influence zone of the base course. As shown in Figure 5.16, the predicted modulus improvement by the developed model is insensitive to the different inputs of the wheel width. The horizontal and vertical stresses acting on the geosynthetic influence zone will be proportionally changed with the wheel width specified. This proportional change in stress condition, however, may not significantly affect the modulus improvement. This consideration may probably explain the insensitivity of the predicted modulus improvement ratio R_E to the wheel width W_w.

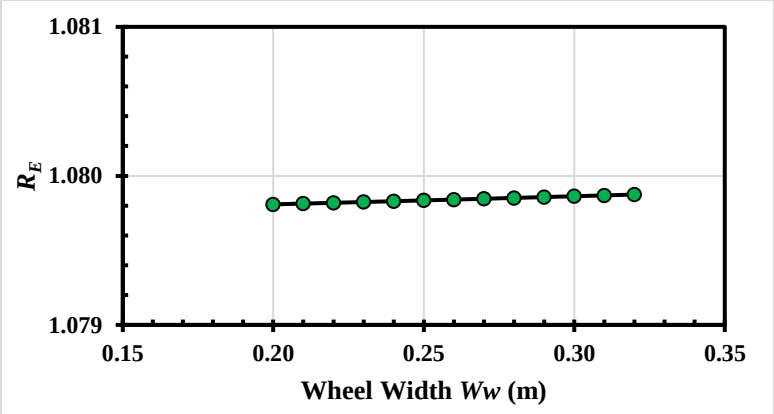

Figure 5.16: Effect of the wheel width W_w on the predicted elastic modulus improvement ratio R_E

5.5 SUMMARY

Based on the preceding sensitivity analysis, the parameters that can significantly affect the predicted modulus improvement include the original elastic modulus of the natural base material E_u, the confined geosynthetic tensile stiffness J_c, the Poisson's ratio μ, the half thickness of the geosynthetic influence zone t, and the half thickness of the geosynthetic t_s. In detail, the predicted elastic modulus improvement ratio R_E increases with decreasing E_u, increasing J_c, increasing μ, decreasing t and decreasing t_s. These trends were found to be consistent with the expectations. Other parameters, however, have no or a small impact on the predicted R_E. The insensitivity of the modulus improvement to some of these parameters may be attributed to certain assumptions made in this model. In general, the insensitivity of R_E to these parameters is acceptable, considering that they do not play a critical role in the quantification of the geosynthetic benefit.

Chapter 6: Summary and Conclusions

6.1 SUMMARY

This research developed an analytical model to quantify the geosynthetic effect on the stabilization of road bases. The basic framework of this model was built based on the theory of elasticity, by determining the force equilibrium, stress-strain relationship and strain displacement relationship under a plane strain condition. Under this framework, the geosynthetic benefit was quantified as the additional confining stress applied to the surrounding base aggregates. Specifically, the additional confining stress was expressed in the form of the geosynthetic unit tension divided by the thickness of the geosynthetic influence zone, assuming a constant distribution of the additional confinement. Together with the selected soil-geosynthetic interaction model, the above relationships in the established framework were utilized to solve the additional confining stress. Furthermore, with a specified equivalence criterion, the increased resilient modulus of the geosynthetic-stabilized base material was estimated based on the additional confining stress. This increased modulus, as the final result of this model, can serve as the input in the design software to calculate the critical pavement response. With the geosynthetic effect incorporated in this way, the rest of current mechanistic-empirical design procedures remain valid for the design of pavements with geosynthetic base stabilization.

The proposed analytical model was validated using the repeated loading triaxial test results from two published studies. Overall, the model predictions matched the experimental data well. In addition, with similar model inputs assigned, the predictions of this model and another analytical model proposed by Yang and Han (2012) were compared, and a generally good consistency was found. Following the model validation, a parametric analysis was conducted to evaluate the sensitivity of the model predictions to each input

parameter. It turned out that the predicted modulus improvement was sensitive to the original elastic modulus of the natural base material, the confined geosynthetic stiffness, the Poisson's ratio, the thickness of the geosynthetic influence zone, and the thickness of the geosynthetic. Reasonable trends were found in variations of the model predictions with changes in the above parameters.

In summary, the proposed analytical model provides, with a reasonably good accuracy, an enhanced modulus value for the geosynthetic-stabilized base layer. The model inputs can be determined with comparatively less time and labor needed for similar model. Unlike those models developed by considering the soil-geosynthetic composite to be a cylinder under triaxial loading, the model proposed in this study characterizes the geosynthetic-stabilized base course as an infinitely long solid under plane strain condition. In addition, the traffic loading is simplified as a continuous strip load. In this way, the geometry and loading mechanism adopted in this model more realistically simulate the in-situ pavement conditions. However, the assumption of the perfect elasticity of the base material, along with the simplified linear stress distributions, reduces the prediction accuracy to some degree. Consequently, predictions of this model may mainly serve as an initial evaluation of the improvement in the base resilient modulus when specific geosynthetics are included, thereby providing preliminary suggestions for the appropriate geosynthetic product and base course thickness that should be selected.

6.2 CONCLUSIONS

The proposed analytical model provides an equivalent property for the geosynthetic-stabilized base material to serve as the surrogate input in the mechanistic-empirical design software. Specifically, this model can estimate the increased elastic modulus of the geosynthetic-stabilized base material with the following inputs:

- Material properties (original base elastic modulus, confined geosynthetic stiffness, the stiffness of the soil-geosynthetic composite, the soil-geosynthetic interface friction angle and the Poisson's ratio);
- Pavement geometry (thicknesses of asphalt layer, base course, geosynthetic influence zone and geosynthetic product);
- Traffic loading condition (tire pressure and wheel width).

Based on the validation and sensitivity analysis of the model predictions, the following conclusions can be made:

- The original elastic modulus of the base aggregate has a significant impact on the quantified geosynthetic benefit. Specifically, the predicted modulus improvement ratio decreases nonlinearly with the increasing original base elastic modulus. This indicates that the geosynthetic is less effective when the base aggregate has already possessed a high modulus.
- The geosynthetic property that governs its stiffening effect is the confined tensile stiffness. The predicted modulus improvement ratio increases almost linearly with the increasing confined tensile stiffness. Considerable geosynthetic benefit can be observed when the low-modulus base aggregate is stabilized by a high-stiffness geosynthetic.

- The magnitude of modulus improvement predicted by this model is sensitive to the specified thickness of the geosynthetic influence zone. However, there is not a well-established method for the determination of this parameter. The assumed 6-inch geosynthetic influence zone thickness, together with other baseline input parameters, results in an estimated 8% modulus increase. This is the average geosynthetic benefit predicted for typical pavement configurations.
- This model considers an infinitely long pavement under an assumed continuous strip load, corresponding to a plane strain problem in the theory of elasticity. Based on the comparison with the repeated loading triaxial test results, the stress-strain and strain-displacement relationships in plane strain problems are proved to be valid in the characterization of the geosynthetic-stabilized base course.
- This model considers the additional confining stress to be the direct indicator of the geosynthetic influence on the road base stabilization. A criterion of equivalence is used to estimate the increased resilient modulus based on the additional confining stress. The increased resilient modulus obtained in this way closely match the results of repeated loading triaxial tests, indicating that the quantification of the geosynthetic influence following such procedures is effective and worth further exploring.
- The model predictions indicate that the geosynthetic influence on increasing the elastic modulus of the geosynthetic-stabilized base material ranged from 4% to 67% for configurations evaluated in this study. The typical range of the percent increase in elastic modulus, however, was 5% to 15%. This increase in resilient modulus was also observed in the repeated loading triaxial test results. Some field test data, however, indicated higher modulus improvement. Further

modification of the stress assumptions in this model by making them closer to the field conditions, may improve the accuracy of the predictions and enable the model results to be better compared with both the laboratory and field data.

6.3 SUGGESTIONS FOR FUTURE WORK

This model builds its basic framework using the theory of elasticity, and the geosynthetic influence is characterized using a specific soil-geosynthetic interaction model. Major assumptions which were made during the development of this model included the assumptions regarding the pavement geometry, loading conditions, form of the additional confining stress, and the criterion of equivalence used to obtain the increased resilient modulus. Accordingly, future research may benefit from additional knowledge or modification of the existing consideration in the following areas:

- The assumed stress distribution within the base course may be modified to better simulate the realistic conditions in the field, including the stresses caused by the construction and traffic loads. For example, it may be helpful to consider the horizontal residual stress induced by the compaction when specifying the initial confinement in the base material.
- The model currently gives more weight to the horizontal displacement in order to incorporate the geosynthetic displacement into the model framework with ease. However, adjustments to the stress assumptions and the displacement function forms may refine the expression of vertical aggregate displacement, so that the rutting calculation will be more accurate.
- The soil-geosynthetic interaction may not be accurately quantified using the theory of elasticity, which is not able to characterize the discontinuous interface. A correction factor α was proposed as a tentative method to make up for this

defect. However, the specific way of defining α may need further justification, or a better approach may be devised to more realistically represent the soil-geosynthetic interaction while ensuring its compatibility with the current model framework.

- A more robust criterion of equivalence may be specified to relate the increased resilient modulus to the additional confining stress.
- Considering that the objective analyzed in this model is the realistic road base, which is infinitely long and under strip wheel load, full-scale tests such as Accelerated Pavement Testing (APT) are desirable to further validate the model predictions. Performance data of the in-service pavements are also a beneficial source of model validation.

Appendix A: Determination of Constants *b* and *d*

The physical meaning of the constant b in the expression of σ_y is the maximum vertical stress (at $x = 0$) within the geosynthetic influence zone. In the realistic pavement loading condition, the subsurface vertical stress decreases with depth under the wheel path. Our solution, however, assumes the vertical stress not to change with the y coordinate within the limited geosynthetic influence zone. Despite this assumption, the vertical stress at the top of the geosynthetic influence zone, calculated based on a stress distribution solution, is selected to be the representative value. This value might be slightly higher than the real average vertical stress within that zone, but it is conservative, especially considering that the accuracy of stress prediction has been lowered due to the linear assumption.

The constant d, on other hand, is the horizontal stress at $x = 0$ within the geosynthetic influence zone. The horizontal stress is also assumed to be a function of only the x coordinate. The same stress distribution solution for a plane strain problem under strip loading as that used for determining b is applicable to the estimate of d. The difference is that the center of the base course (point(0,0)) is selected to be the calculation point in the mentioned solution to estimate d. It results in lower confining stresses compared to using the top of the geosynthetic influence zone for prediction. This selection is also conservative since less confining stress corresponds to more potential rutting.

The term *strip loading* is used to indicate a loading which has a finite width along the transverse direction but an infinite length along the longitudinal direction. Solutions have been gained by Carothers (1920) for various forms of stress distribution across the width of the strip. The solution for a uniformly loaded strip applies to our problem, since the wheel load is idealized to be a continuous strip load to match the plane strain condition.

The geometry of the problem is shown in Figure A.1. The horizontal and vertical stresses can be calculated with Equations (a.1) and (a.2), as follows:

$$\sigma_x = \frac{p}{\pi}(\theta - sin\theta \cdot cos2\beta) \qquad \text{(a.1)}$$

$$\sigma_y = \frac{p}{\pi}(\theta + sin\theta \cdot cos2\beta) \qquad \text{(a.2)}$$

As mentioned earlier, the vertical stress at point A in Figure A.2 can be calculated using Equation (a.2) to represent the constant *b*, while the horizontal stress at point B in Figure A.2 can be calculated using Equation (a.1) to represent the constant *d*. However, the results of Equations (a.1) and (a.2) should be multiplied by -1 before assigned to *b* and *d*, since *b* and *d* both correspond to compressive stresses which are negative as prescribed in the elastic theory.

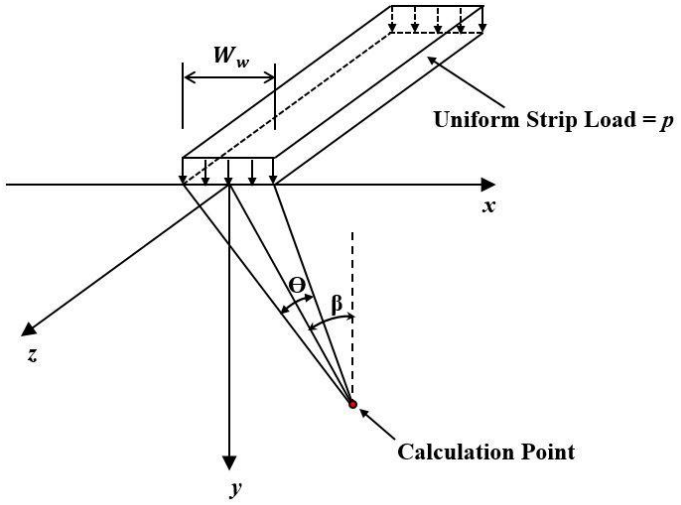

Figure A.1: Geometry of the problem involving a uniform strip load

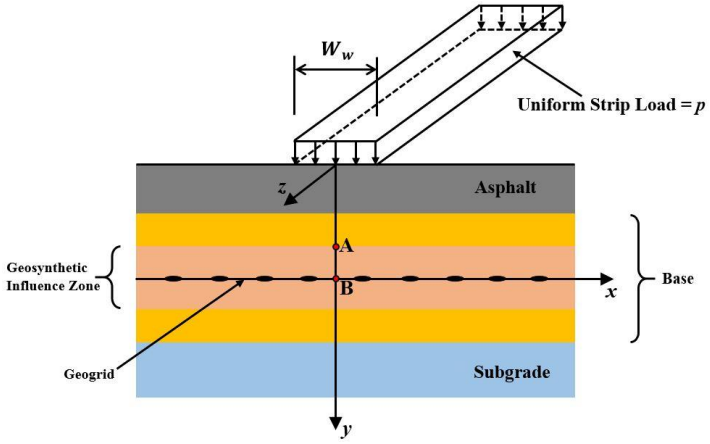

Figure A.2: Calculation points for estimating *b* and *d*

Appendix B: Determination of Constant *c*

The constant c in the assumed expression of σ_x is the rate of change of the horizontal stress along the *x* axis. The constant c cannot be assumed or estimated arbitrarily. By exploring the governing differential equations pertaining to the equilibrium in the elastic system, c is found to be a certain function of a to meet the equilibrium requirement, where a is the rate of change of the vertical stress along the *x* axis. The detailed derivation is discussed as follows.

As introduced in Section 3.2.3, the force equilibrium in an elastic object is described by Equation (3.1) and (3.2). Since σ_y is a function of only the x coordinate and τ_{xy} is a function of only the y coordinate, Equation (3.2) is valid all the time for our case. On the other hand, substitution of Equations (3.10) and (3.25) into Equation (3.1) yields the following equation:

$$\frac{\partial(cx+d)}{\partial x} + \frac{\partial\left(\frac{1-\mu}{2}\left(a-\frac{\mu}{1-\mu}c\right)y\right)}{\partial y} = 0 \tag{b.1}$$

After processing Equation (b.1), c turns to be a linear function of a, as follows:

$$c = \frac{1-\mu}{\mu-2}a \tag{b.2}$$

As prescribed in the theory of elasticity, the compressive stress is negative. Both the horizontal and vertical stresses in our case are compressive stresses. As indicated by Equation (3.15), a is a positive value, corresponding to the decreasing $|\sigma_y|$ but the increasing σ_y in value with the increasing x. Furthermore, μ, as the Poisson's ratio, is within the range of [0, 0.5]. Consequently, c is a negative value, which corresponds to the increasing $|\sigma_x|$ but the decreasing σ_x in value with the increasing x. It means that more lateral confinement exists where closer to the boundary of the vertical stress distribution.

It makes sense considering that the aggregates move much less at the periphery of the vertical stress distribution, thus providing more restraint for the inner aggregates.

In summary, by assigning such a *c* value for the expression of σ_x, the equilibrium in the elastic object, namely the geosynthetic influence zone in our case, is satisfied. The determined *c* value using Equation (b.2) is considered as suitable simplification of the realistic lateral confinement condition.

Appendix C: Correction Factor α

In Section 3.3.3.3, a correction factor α is adopted in the definition of the additional confining stress $\Delta\sigma_3$ to consider the contribution of the bearing resistance to the soil-geosynthetic interaction. This correction factor α is only applicable to geogrids since the bearing resistance is provided by the transverse ribs perpendicular to the geosynthetic displacement direction. For geotextiles, $\alpha = 1$. As follows, this section explains why a correction factor is required by this analytical model for geogrids and then discusses how it can be determined.

As explained in Section 3.3.3.3, the additional confining stress applied by the geosynthetic to the base material can be defined as follows:

$$\Delta\sigma_3 = \alpha \cdot \frac{T_{avg}}{2t} = \alpha \cdot \frac{T_{(x=0)}}{4t} = \alpha \cdot \frac{\tau_y L'}{2t} \tag{c.1}$$

where $\Delta\sigma_3$ =the additional confining stress; $t =$ the half thickness of the geosynthetic influence zone; $T_{avg} =$ the average geosynthetic unit tension; $T_{(x=0)} =$ the geosynthetic unit tension at $x = 0$; $\tau_y =$ the yield shear stress at the soil-geosynthetic interface, and $L' =$ the geosynthetic active length.

The above definition is easy to understand if α is not involved. The factor α is adopted for the geogrids considering the difficulty in the determination of the yield interface shear stress τ_y. Without a correction factor, it is hard to specify a τ_y that remains compatible with the elastic analytical framework and meanwhile quantifies the geosynthetic influence accurately. This is discussed in detail as follows:

Firstly, if calculating τ_y using the shear stress function derived from the elastic theory, it can be expressed as follows by substituting $y = t_{gs}$ into Equation (3.25):

$$\tau_y = \frac{1-\mu}{2}\left(a - \frac{\mu}{1-\mu}c\right)t_{gs} \tag{c.2}$$

where $t_{gs} =$ the half thickness of the geosynthetic. This yield shear stress τ_y is calculated by considering the base course as a homogeneous and continuous object, so it cannot take into account the soil-geosynthetic interaction. It is assumed that such a shear stress can, at best, represent the contribution from the interface friction. In the case of the realistic traffic loading, however, the geogrid transverse ribs perpendicular to the geosynthetic horizontal displacement direction may develop more local deformation compared to that of the longitudinal ribs parallel to that direction, as shown in Figure C.1. This occurs because the transverse ribs deform due to their interlock with the moving particles while the longitudinal ribs' deformation is attributed to the interface friction. If substituting Equation (c.2) into Equation (3.51) to calculate L', which is further plugged into Equation (3.42) to calculate u_g, the resultant geogrid displacement is considered as only the representation of the longitudinal rib deformation, since the τ_y used is from the elastic prediction. Accordingly, the geosynthetic influence might be underestimated without properly quantifying the local transverse rib deformation or the corresponding bearing resistance it contributes.

On the other hand, if τ_y is selected based on the results of the large-deformation tests such as pullout or interface direct shear tests, it will have much larger magnitude than that estimated by the elastic theory. When evaluating the soil-geosynthetic relative displacement, the geosynthetic displacement estimated using the experimental τ_y turned out to be larger than the base aggregate displacement estimated with the elastic theory. This is unreasonable considering that the geosynthetic displacement is powered by the aggregate movement. As indicated by Equation (3.46), zero soil-geosynthetic relative displacement is considered at $x = L'$ to calculate L' and $\Delta\sigma_3$. Despite this unique boundary condition, two situations can satisfy the requirement as shown in Figure C.2. The dot curve corresponds to the calculation where the experimental τ_y is adopted. Even though

Equation (3.46) is satisfied by this dot curve, it indicates smaller aggregate displacement than that of the geosynthetic, making it an unreasonable solution. According, in this analytical model, the adopted yield shear stress is required to be derived from the elastic theory, to make it compatible with the elastic analytical framework and to ensure reasonable soil-geosynthetic relative displacement.

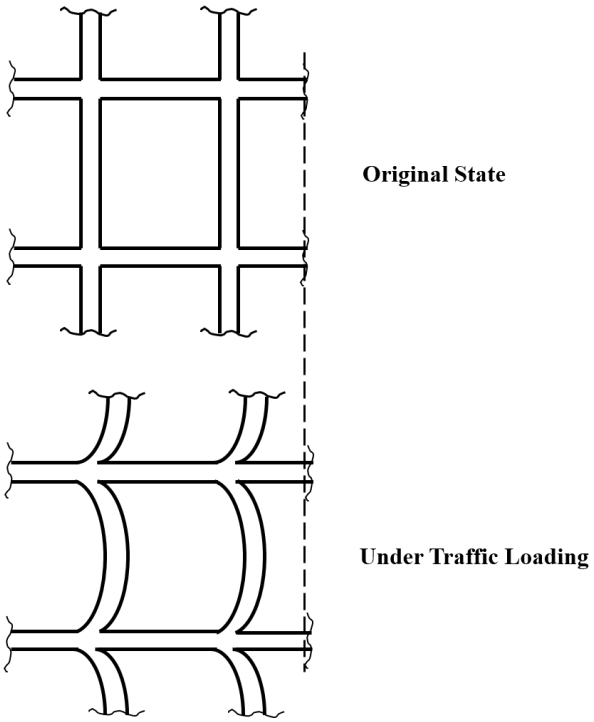

Figure C.1: Deformation of transverse and longitudinal ribs under traffic loading

So far, the problem is that the τ_y derived from the elastic theory cannot involve the contribution from the bearing resistance of transverse ribs, while the experimental τ_y cannot result in reasonable soil-geosynthetic relative displacement. To overcome this obstacle, Equation (c.2) is still used to calculate τ_y, but a correction factor α is adopted in the definition of $\Delta\sigma_3$. In this way, if $\frac{\tau_y L'}{2t}$ represents the additional confinement caused by the interface friction, $\alpha \cdot \frac{\tau_y L'}{2t}$ incorporates the bearing resistance into the estimate of $\Delta\sigma_3$

by converting its contribution to a factor larger than one. It satisfies requirements of the bearing resistance consideration and the reasonable relative displacement at the same time. The approach to determine this correction factor α is discussed as follows.

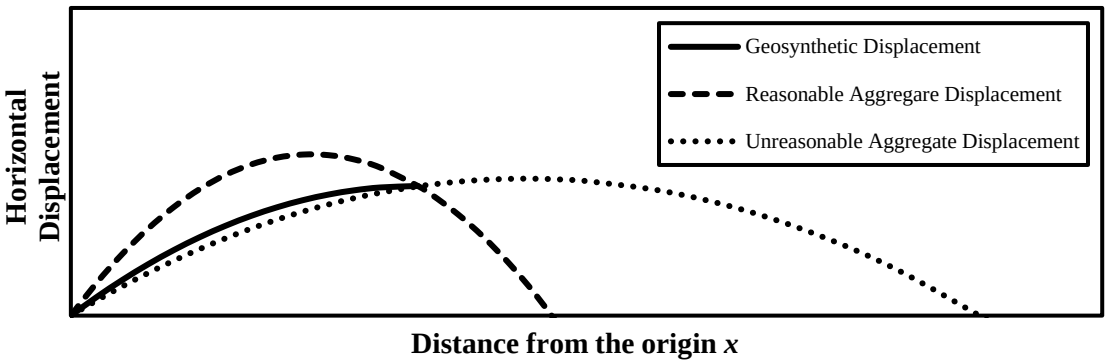

Figure C.2: Unreasonable result of aggregate displacement using experimental τ_y

As explained in Section 3.3.3.3, Equation (3.52) can be used to calculate the additional confining stress $\Delta\sigma_3$. If the correction factor α is not considered, i.e. $\alpha = 1$, Equation (3.52) can be rewritten as follows:

$$\Delta\sigma_3 = \frac{\frac{1-\mu^2}{E_u}\left(d-\frac{\mu}{1-\mu}b\right)\frac{J_c}{2t}}{1-\frac{1-\mu^2}{E_u}\frac{J_c}{2}\left[\left(c-\frac{\mu}{1-\mu}a\right)\frac{1}{\tau_y}-\frac{1}{t}\right]} \tag{c.3}$$

where $E_u =$ original elastic modulus of the base material, $\mu =$ Poisson's ratio of the base material, $J_c =$ confined geosynthetic stiffness, $\tau_y =$ yield shear stress at the soil-geosynthetic interface, *a*, *b*, *c* and *d* are the constants in the assumptions of vertical and horizontal stresses, and *t* is the half thickness of the geosynthetic influence zone.

Correction factor α is assumed to be the ratio of the full additional confinement (considering both interface friction and bearing resistance) to the additional confinement caused by only the interface friction. It is suggested that one of the following three

approaches be used to determine α. Specifically, Approach 3 is similar to Approach 1 except that the yield shear stress (τ_y) at the soil-geosynthetic interface is determined from the stiffness of the soil-geosynthetic composite (K_{SGC}) instead of an interface friction angle (ϕ). These approaches can be used to compare with and validate each other.

Approach 1:

This approach utilizes the existing Equation (c.3) in this model to estimate the contribution to the additional confining stress from different mechanisms of interface interaction. In detail, the three steps below need to be followed:

Step 1: Select the yield shear stress τ_y to be the interface shear strength, as calculated using the following equations:

$$\tau_y = \sigma_{y,avg} \cdot tan\,\phi \tag{c.4}$$

$$\sigma_{y,avg} = \frac{aL'}{2} + b \tag{c.5}$$

where $\sigma_{y,avg} =$ the average vertical stress within the geosynthetic active length, as calculated using Equation (c.5), and $\phi =$ the interface friction angle, which can be obtained from interface direct shear tests or using typical values. Substitution of Equation (c.4) into Equation (c.3) yields an estimate of $\Delta\sigma_3$, which is considered as the full additional confinement ($\Delta\sigma_{3,full}$), including the contribution from both the interface friction and the bearing resistance of transverse geogrid ribs.

Step 2: Select the yield shear stress τ_y to be the function derived from the elastic theory, i.e. Equation (c.2). Substitution of Equation (c.2) into Equation (c.3) results in another estimate of $\Delta\sigma_3$, which is considered as the additional confinement caused by the interface friction. This $\Delta\sigma_3$ can be denoted by $\Delta\sigma_{3,fric}$.

Step 3: The correction factor α can be calculated as the ratio between the above two estimates of $\Delta\sigma_3$, as follows:

$$\alpha = \frac{\Delta\sigma_{3,full}}{\Delta\sigma_{3,fric}} \quad \text{(c.6)}$$

Approach 2:

This approach is associated with the geometric analysis of geogrids. The theory used here was borrowed from the evaluation of pullout resistance. Although the soil-geosynthetic interaction in roadway bases under traffic loading is different from the pullout mechanism, the relative contribution to $\Delta\sigma_3$ from the skin friction and the bearing resistance can be similarly compared based on the counterparts in the formulation of pullout resistance. After all, the emphasis is the ratio of the interaction components instead of the specific values.

As per Jewell (1990) and Moraci & Gioffrè (2006), the following equations can be used to evaluate the pullout resistance, for a geogrid of length L_R and unit width W_R:

$$P_R = P_{RS} + P_{RB} \quad \text{(c.7)}$$

$$P_{RS} = 2\alpha_s L_R \tau = 2\alpha_s L_R \sigma_n' tan\delta \quad \text{(c.8)}$$

$$P_{RB} = \left(\frac{L_R}{S}\right) \alpha_B \sigma_b' B \quad \text{(c.9)}$$

where $P_R =$ pullout resistance; $P_{RS} =$ skin friction component of pullout resistance; $P_{RB} =$ the bearing component of pullout resistance; $\alpha_s =$ the fraction of geogrid surface area that is solid; $\tau =$ shear stress acting at soil-geosynthetic interface; $\sigma_n' =$ the normal effective stress, $\delta =$ the skin friction angle between soil and geogrid, $S =$ the spacing between geogrid bearing members, $\frac{L_R}{S} =$ the number of geogrid bearing members, $\alpha_B =$ the fraction of total frontal area of geogrid available for bearing, $\sigma_b' =$ the effective bearing stress on the geogrid bearing members, and $B =$ the bearing member thickness.

For general shear failure mechanism, the ratio σ_b'/σ_n' may be defined as follows (Moraci & Gioffrè (2006)):

$$\frac{\sigma_b'}{\sigma_n'} = e^{\pi tan\phi'} \tan(\frac{\pi}{4} + \frac{\phi'}{2}) \quad \text{(c.10)}$$

where ϕ' is the soil shear strength angle.

In this approach, to estimate the weight of skin friction in the total soil-geogrid interaction in roadway bases, it is assumed that α equals the ratio of the total pullout resistance to its skin friction component under a corresponding pullout loading condition, as follows:

$$\alpha = \frac{P_R}{P_{RS}} = \frac{P_{RS}+P_{RB}}{P_{RS}} \quad \text{(c.11)}$$

As mentioned earlier, pullout is not the mechanism of soil-geogrid interaction in roadway bases. Despite this discrepancy, the ratio $\frac{P_R}{P_{RS}}$ is considered as an approximate representation of the correction factor α in our case.

It was found in this study that Approaches 1 and 2 resulted in similar estimates of α. Consequently, similar predictions of the increased base elastic modulus were obtained when specifying α using Approach 1 and Approach 2 respectively, as shown by Figures 4.1 to 4.3 in Chapter 4.

Approach 3:

This approach has similar three steps and definition of α as proposed in Approach 1. Specifically, Steps 2 and 3 of Approach 3 are exactly the same as in Approach 1, and thus α is still calculated using Equation (c.6). In Step 1 of Approach 3, however, the yield shear stress (τ_y) used to calculate the full additional confinement ($\Delta\sigma_{3,full}$) is determined from the stiffness of the soil-geosynthetic composite (K_{SGC}), which is the parameter generated in the soil-geosynthetic composite (SGC) model and can be obtained using pullout tests.

In the SGC model, the parameter K_{SGC} is used to relate the geosynthetic unit tension to geosynthetic displacement. According to Equations (3.32) and (3.39) in Chapter 3, the following equation can be obtained:

$$T(x)^2 = (4\tau_y J_c) \cdot u_g(x) \tag{c.12}$$

where $\tau_y =$ yield shear stress at the soil-geosynthetic interface, $J_c =$ confined geosynthetic tensile stiffness, $T(x) =$ the geosynthetic unit tension at *x*, and $u_g(x) =$ the geosynthetic displacement at *x*. Consequently, the stiffness of the soil-geosynthetic composite (K_{SGC}) was defined in the SGC model as follows:

$$K_{SGC} = 4\tau_y J_c \tag{c.13}$$

That is

$$T(x)^2 = K_{SGC} \cdot u_g(x) \tag{c.14}$$

This single parameter K_{SGC} may be particularly suitable for the characterization of the soil-geosynthetic interaction under small displacements (Zornberg et al., 2017). Consequently, the yield shear stress (τ_y), as obtained from the SGC model using the following equation, is considered a good estimate of the soil-geosynthetic interface shear strength that can be used to calculate the full additional confinement ($\Delta\sigma_{3,full}$):

$$\tau_y = \frac{K_{SGC}}{4J_c} \tag{c.15}$$

Specifically, substitution of Equation (c.15) into Equation (c.3) yields the estimate of $\Delta\sigma_{3,full}$. With $\Delta\sigma_{3,fric}$ obtained in the same way as Step 2 of Approach 1, the correction factor α can be calculated using Equation (c.6), and after simplification, α can be ultimately expressed as follows:

$$\alpha = \frac{1-\frac{1-\mu^2}{E_u}\frac{J_c}{2}\left\{\frac{2[(1-\mu)c-\mu a]}{(1-\mu)[(1-\mu)a-\mu c]t_{gs}}-\frac{1}{t}\right\}}{1-\frac{1-\mu^2}{E_u}\frac{J_c}{2}\left[\left(c-\frac{\mu}{1-\mu}a\right)\frac{4J_c}{K_{SGC}}-\frac{1}{t}\right]} \quad \text{(c.16)}$$

where $E_u =$ original elastic modulus of the base material, $\mu =$ Poisson's ratio of the base material, $J_c =$ confined geosynthetic stiffness, $\tau_y =$ yield shear stress at the soil-geosynthetic interface, *a*, *b*, *c* and *d* are the constants in the assumptions of vertical and horizontal stresses, *t* = the half thickness of the geosynthetic influence zone, and K_{SGC} = stiffness of the soil-geosynthetic composite.

Summary:

This correction factor α obtained from one of the three approaches above is ultimately plugged into Equation (3.52) to calculate the additional confining stress $\Delta\sigma_3$, which will be the final model prediction of the additional confinement caused by the geosynthetic inclusion.

References

Abdi, M. R., & Zandieh, A. R. (2014). Experimental and numerical analysis of large scale pull out tests conducted on clays reinforced with geogrids encapsulated with coarse material. Geotextiles and Geomembranes, 42(5), 494-504.

Abu-Farsakh, M. Y., & Chen, Q. (2011). Evaluation of geogrid base reinforcement in flexible pavement using cyclic plate load testing. International Journal of Pavement Engineering, 12(03), 275-288.

Al-Qadi, I. L., Dessouky, S. H., Kwon, J., & Tutumluer, E. (2008). Geogrid in flexible pavements: validated mechanism. Transportation Research Record, 2045(1), 102-109.

Al-Qadi, I. L., Dessouky, S. H., Kwon, J., & Tutumluer, E. (2012). Geogrid-reinforced low-volume flexible pavements: pavement response and geogrid optimal location. Journal of Transportation Engineering, 138(9), 1083-1090.

American Association of State Highway and Transportation Officials, (1993), AASHTO Guide for Design of Pavement Structures, Washington, DC, USA.

American Association of State Highway and Transportation Officials (AASHTO), (2015). Mechanistic-Empirical Pavement Design Guide, 2nd Edition: A Manual of Practice. American Association of State Highway and Transportation Officials, Washington, DC, USA.

American Association of State Highway and Transportation Officials (AASHTO), (2015). Pavement Design, Construction, and Management, 1st Edition: A Digital Handbook. American Association of State Highway and Transportation Officials, Washington, DC.

ARA, Inc. (2004). Guide for mechanistic-empirical design of new and rehabilitated pavement structures. Final Rep. NCHRP Project 1-37A, Transportation Research Board, Washington, DC.

Archer, S. (2008). Subgrade Improvement for Paved and Unpaved Surfaces Using Geogrids. CE News Professional Development Hours.

Archer, S., & Wayne, M. H. (2012). Relevancy of Material Properties in Predicting the Performance of Geogrid-Stabilized Roadways. In GeoCongress 2012: State of the Art and Practice in Geotechnical Engineering, 1320-1329.

Askeland, D. R., Fulay, P. P., & Wright, W. J. (2003). The science and engineering of materials. 6th edition, Cengage Learning, Inc.

Berg, R. R., Christopher, B. R., & Perkins, S. (2000). Geosynthetic reinforcement of the aggregate base/subbase courses of pavement structures (No. GMA White Paper II).

Cox, B. R., Goldman, T. M., & McCartney, J. S. (2011). The Marked Tree Site: Evaluation of Geosynthetic Reinforcements in Flexible Pavements (No. TRC 0903).

Giroud, J. P., & Noiray, L. (1981). Geotextile-reinforced unpaved road design. Journal of Geotechnical and Geoenvironmental Engineering, 107(ASCE 16489).

Giroud, J. P., Ah-Line, C., & Bonaparte, R. (1984). Design of unpaved roads and trafficked areas with geogrids. In Polymer grid reinforcement (pp. 116-127). Thomas Telford Publishing.

Giroud, J. P., & Han, J. (2004). Design method for geogrid-reinforced unpaved roads. II. Calibration and applications. Journal of Geotechnical and Geoenvironmental Engineering, 130(8), 787-797.

Giroud, J. P., & Han, J. (2006). Closure to "Design Method for Geogrid-Reinforced Unpaved Roads. I: Development of Design Method" by JP Giroud and Jie Han. Journal of Geotechnical and Geoenvironmental Engineering, 132(4), 549-551.

Han, J. (2015). Principles and practice of ground improvement, Wiley, Hoboken, NJ.

Highway Research Board, (1961). The AASHO Road Test: History and Description of Project. National Academy of Sciences.

Holtz, R. D., Christopher, B. R., & Berg, R. R. (1998), "Geosynthetic Design and Construction Guidelines", U.S. Department of Transportation, Federal Highway Administration, Washington, DC, FHWA-HI-98-038, 460 p

Huang, Y. H. (1993). Pavement analysis and design. Prentice-Hall, Englewood Cliffs, N.J.

Hufenus, R., Rueegger, R., Banjac, R., Mayor, P., Springman, S. M., & Brönnimann, R. (2006). Full-scale field tests on geosynthetic reinforced unpaved roads on soft subgrade. Geotextiles and Geomembranes, 24(1), 21-37.

Hugo, F., & Martin, A. E. (2004). Significant findings from full-scale accelerated pavement testing (Vol. 325). Transportation Research Board.

Jewell, R. A. (1990). Reinforcement bond capacity. Geotechnique, 40(3), 513-518.

Koerner, R. M. (2012). Designing with geosynthetics (Vol. 1). Xlibris Corporation.

Lee, K. M., & Manjunath, V. R. (2000). Soil-geotextile interface friction by direct shear tests. Canadian geotechnical journal, 37(1), 238-252.

Ling, H. I., & Tatsuoka, F. (1994). Performance of anisotropic geosynthetic-reinforced cohesive soil mass. Journal of geotechnical engineering, 120(7), 1166-1184.

Liu, C. N., Ho, Y. H., & Huang, J. W. (2009). Large scale direct shear tests of soil/PET-yarn geogrid interfaces. Geotextiles and Geomembranes, 27(1), 19-30.

Maubeuge, K. V., & Klompmaker, J. (2011). New developments for geogrid reinforced base courses. In Geo-Frontiers 2011: Advances in Geotechnical Engineering (pp. 4624-4634).

Moghaddas-Nejad, F., & Small, J. C. (2003). Resilient and permanent characteristics of reinforced granular materials by repeated load triaxial tests. Geotechnical testing journal, 26(2), 152-166.

Moraci, N., & Gioffrè, D. (2006). A simple method to evaluate the pullout resistance of extruded geogrids embedded in a compacted granular soil. Geotextiles and Geomembranes, 24(2), 116-128.

Moraci, N., Cardile, G., Gioffrè, D., Mandaglio, M. C., Calvarano, L. S., & Carbone, L. (2014). Soil geosynthetic interaction: design parameters from experimental and theoretical analysis. Transportation Infrastructure Geotechnology, 1(2), 165-227.

Olague, P. B., Nazarian, S., Kreinovich, V., Gholamy, A., & Mazari, M. (2018). How to estimate resilient modulus for unbound aggregate materials: a theoretical explanation of an empirical formula. In Recent Developments and the New Direction in Soft-Computing Foundations and Applications, 571-580. Springer, Cham.

Palmeira, E. M. (2009). Soil–geosynthetic interaction: modelling and analysis. Geotextiles and Geomembranes, 27(5), 368-390.

Pedersen, N. J. (2007), 'Pavement lessons learned from the AASHO road test and the performance of the interstate highway system', Transportation Research Board, Pavement Management Section.

Perkins, S. W., & Ismeik, M. (1997). A Synthesis and Evaluation of Geosynthetic-Reinforced Base Layers in Flexible Pavements-Part I. Geosynthetics International, 4(6), 549-604.

Perkins, S. W., & Ismeik, M. (1997). A Synthesis and Evaluation of Geosynthetic-Reinforced Base Layers in Flexible Pavements-Part II. Geosynthetics International, 4(6), 605-621.

Perkins, S. W., & Cuelho, E. V. (1999). Soil-geosynthetic interface strength and stiffness relationships from pullout tests. Geosynthetics International, 6(5), 321-346.

Roodi, G. H., & Zornberg, J. G. (2012). Effect of geosynthetic reinforcements on mitigation of environmentally induced cracks in pavements. In Proceedings of the 5th European Geosynthetics Conference, EuroGeo5 (pp. 16-19).

Roodi, G. H., & Zornberg, J. G. (2017). Stiffness of soil-geosynthetic composite under small displacements. II: Experimental evaluation. Journal of Geotechnical and Geoenvironmental Engineering, 143(10), 04017076.

Sukmak, K., Sukmak, P., Horpibulsuk, S., Han, J., Shen, S. L., & Arulrajah, A. (2015). Effect of fine content on the pullout resistance mechanism of bearing reinforcement embedded in cohesive–frictional soils. Geotextiles and Geomembranes, 43(2), 107-117.

Vieira, C. S., Lopes, M. D. L., & Caldeira, L. M. (2013). Sand-geotextile interface characterisation through monotonic and cyclic direct shear tests. Geosynthetics International, 20(1), 26-38.

Witczak, M. W. (2003). Harmonized test methods for laboratory determination of resilient modulus for flexible pavement design. Project No. NCHRP 1-28A.

Yang, X., Han, J., Pokharel, S. K., Manandhar, C., Parsons, R. L., Leshchinsky, D., & Halahmi, I. (2012). Accelerated pavement testing of unpaved roads with geocell-reinforced sand bases. Geotextiles and Geomembranes, 32, 95-103.

Zhao, A., & Foxworthy, P. T. (1999). Geogrid reinforcement of flexible pavements: a practical perspective. Geotechnical Fabrics Report, 17(4).

Zornberg, J. G., & Gupta, R. (2010). Geosynthetics in pavements: North American contributions. In Theme Speaker Lecture, Proceedings of the 9th International Conference on Geosynthetics, Guarujá, Brazil, May (Vol. 1, pp. 379-400).

Zornberg, J. G., Ferreira, J. A. Z., Gupta R., Joshi R. V., & Roodi, G. H. (2012). Geosynthetic-reinforced unbound base courses: quantification of the reinforcement benefits (No. FHWA/TX-10/5-4829-01-1).

Zornberg, J. G., Roodi, G. H., Ferreira, J., & Gupta, R. (2012). Monitoring performance of geosynthetic-reinforced and lime-treated low-volume roads under traffic loading and environmental conditions. In GeoCongress 2012: State of the Art and Practice in Geotechnical Engineering (pp. 1310-1319).

Zornberg, J. G. (2017). Functions and applications of geosynthetics in roadways. Procedia engineering, 189, 298-306.

Zornberg, J. G., Roodi, G. H., & Gupta, R. (2017). Stiffness of Soil–Geosynthetic Composite under Small Displacements: I. Model Development. Journal of Geotechnical and Geoenvironmental Engineering, 143(10), 04017075.

Vita

Ziye Liu was born in Xuzhou, Jiangsu, China. He received his Bachelor of Engineering degree in Geological Engineering from Lanzhou University. He was a master's student in the Geotechnical Engineering Program at the University of Texas at Austin from 2016 to 2018.

Email address: ziyeliu@utexas.edu

This thesis was typed by Ziye Liu.